Institut für Physikalische und Theoretische Chemie
der Technischen Universität München

Dynamics of Photoinduced Charge Transfer Processes in Modified DNA and an Engineered Protein

Stephan Hess

Vollständiger Abdruck der von der Fakultät für Chemie der Technischen Universität München zur Erlangung des akademischen Grades eines

Doktors der Naturwissenschaften

genehmigten Dissertation.

Vorsitzender: Univ.-Prof. Dr. Dr. A. Bacher
Prüfer der Dissertation:

1. Univ.-Prof. Dr. M.-E. Michel-Beyerle, i. R.
2. Univ.-Prof. Dr. H. Scheer, Ludwig-Maximilians-Universität München
3. Univ.-Prof. Dr. N. Rösch

Die Dissertation wurde am 16.04.2002 bei der Technischen Universität München eingereicht und durch die Fakultät für Chemie am 28.05.2002 angenommen.

meinen Eltern
und Katrin

Table of Contents

1 Introduction

1.1 Motivation and Background

Electron transfer (ET) processes are ubiquitous in chemistry, biology, and physics.[1] In the context of reaction mechanisms in chemistry the breaking of bonds as well as changes of molecular conformation are often initiated by changes in the charge distribution due to the polarization or ET between separated entities. Also in biochemical molecules, electron transfer may initiate bond breakage. Such a sequence of events is realized, for instance, in DNA photolyases, where a reduced flavin coenzyme in its excited state transfers an electron to a thymine dimer which initiates bond splitting and leads to DNA repair.[2]

Proteins with highly resolved X-ray structures have provided the most detailed insight into ET mechanisms and dynamics, since they allow experimental access to electron transfer rates. The majority of the experimental results were modeled within the framework of nonadiabatic electron transfer theory. The most prominent example is the reaction center of photosynthetic bacteria where transmembrane electron transfer proceeds sequentially between strictly localized donor and acceptor sites on time scales between 1 ps and 100 ms.[3-5] The rates of the activationless transmembrane ET processes are essentially determined by the distance dependence of the electronic couplings. Time-resolved spectroscopy revealed that the electronic coupling of the first and second electron transfer steps is determined by direct exchange interactions between donor and acceptor, whereas the third forward step and all recombination reactions are mediated by superexchange interactions. For the recombination processes that occur over center-to-center-distances of about 17 Å and 30 Å, time scales in the nanosecond and hundred millisecond ranges, respectively, were reported.[3, 5]

At this stage of understanding of electron transfer mechanisms in the reaction center protein experiments on DNA duplexes were reported that postulated a distance-independent electron transfer process between a photoexcited injector and an acceptor species separated by more than 40 Å.[6, 7] This provoking concept of DNA functioning as a molecular wire or "π-way" was based either exclusively on biochemical control of thymine dimer splitting at a distance from a tethered rhodium metallointercalator[6] or was merely

inferred from the absence of fluorescence of the photoexcited charge injector.[6] However, other research groups reported measurements of the distance dependence of electron transfer rates in DNA with a strong exponential fall-off behavior.[8, 9] These discrepancies have been explained to be partly due to the complexity of and insufficient information on the structure of some of these DNA donor–acceptor systems.[10] In addition, in some cases the evidence available was not sufficient for the conclusions drawn.

In a theoretical approach two distinct electron transfer mechanisms in DNA donor–acceptor systems were advanced, which bear a close analogy to the mechanisms of ET in bacterial photosynthesis.[11] This concept is based on the hierarchy of the in vitro oxidation potentials of the nucleobases in solution. The redox potential of adenine (A) is about 0.4 eV higher than that of guanine (G) and the potentials of the pyrimidine nucleobases thymine (T) and cytosine (C) are approximately 0.6 eV higher than in guanine.[12, 13] Therefore, hole transfer between guanines or between an exogenous hole donor and a guanine occurs as a unistep process with a strong distance dependence mediated by superexchange interaction with adenine and thymine. In this picture, the possibility of weakly distance-dependent hole transport phenomena in DNA has been explained by diffusive hopping processes between adjacent guanines. In the single hopping steps the electronic coupling is mediated by superexchange interactions as in the unistep process. The realization of one of these two mechanisms is determined by the base sequence within the DNA bridge.[11]

One of the central questions in DNA charge transfer research is whether conventional ET theory is capable of modeling electron transfer processes accurately in the DNA environment with its unique and characteristic features. Such a theoretical understanding is relevant to oxidative damage and certain pathophysiological processes such as cancer and ageing.[14, 15] Other potential applications were expected in molecular electronics.[16-18] The double helix of the standard B-form of DNA consists of two antiparallel polynucleotide chains.[19] Highly charged sugar–phosphate backbones spiral around a well-defined stack of paired nucleobases (Fig. 1.1). The double helix is also stabilized by interactions between the stacked bases on the same strand that have a separation of 3.4 Å. The average number of base pairs per helical turn is 10.4 and the helix twist is 36°. Numerous aromatic molecules have a high propensity to intercalate between two base pairs. Such molecules, either randomly intercalated or covalently bound to the framework, have been used as charge donors and acceptors.[8, 9] The exact location of the donor and acceptor molecules in DNA is difficult to control. However, a structural characterization is possible applying NMR techniques.[19-20]

The aim of the present work was to study the dynamics of charge injection and transport in structurally defined DNA donor–acceptor systems and to answer several open questions related to the previously proposed ET mechanisms. This has been done by means of

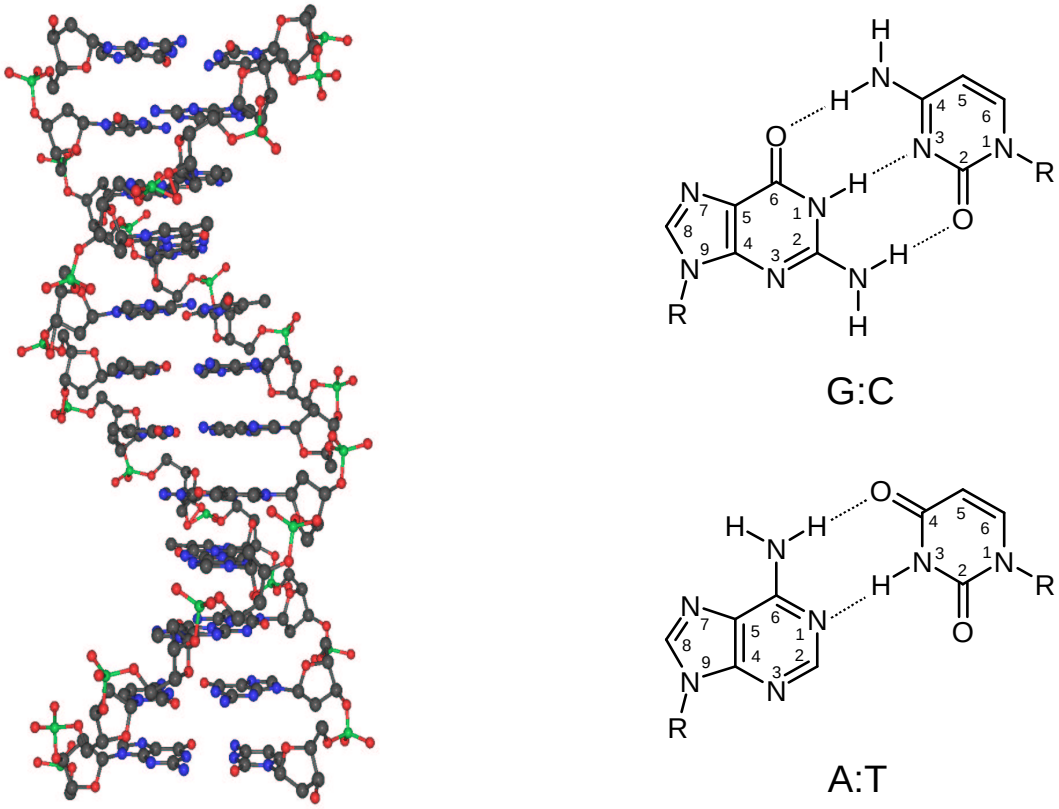

Fig. 1.1: Molecular structure of B-form DNA. The double helix consists of two antiparallel polynucleotide chains (left). Guanine:cytosine and adenine:thymine Watson–Crick base pairs (right). R indicates the deoxyribose $C_{1'}$ atom of the sugar–phosphate backbone.

femtosecond time-resolved absorption spectroscopy. In addition, this technique has been applied to identify the mechanism of the strong fluorescence quenching in a structurally well-defined protein.

1.2 Topic of this Work

1.2.1 Charge Transfer in Modified DNA

For a detailed study of the charge transfer mechanisms in DNA the optimal donor–acceptor system should meet a number of requirements:

- A precise definition of the donor–acceptor distance.
- A minimal perturbation of the DNA structure by the attached molecules.
- A thorough investigation of the charge injection process.

Additionally, an injection process that provides optimal conditions for a long-range hopping study should take into account the following points:

- Hole injection should occur via a charge shift reaction because of the minimized Coulomb well in contrast to charge separation.
- A weak electronic coupling between the hole donor and the bridge is required because in this case hole hopping along the strand is expected to favorably compete with the backward charge transfer. For such injection systems the electronic coupling should decrease steeply with the number of A:T base pairs between the donor and the acceptor.

Structurally defined DNA donor–acceptor systems suitable for the investigation of the dynamics of photoinduced charge transfer processes have become available only recently. Whereas Lewis et al. used stilbene-linked DNA hairpins,[9] Fukui and coworkers employed a 9-amino-6-chloro-2-methoxyacridine (ACMA) derivative inserted into a specific abasic site of a DNA duplex as hole injector.[21-23] In both experiments a guanine nucleobase was used as the acceptor. By varying the number of A:T base pairs between the photoexcited chromophore and the guanine the distance dependence of the charge injection was studied. Whereas Lewis et al. reported a decay parameter of $\beta = 0.7$ Å^{-1} for photoinduced charge separation in the stilbene-linked DNA hairpins[9] a significantly larger attenuation parameter of $\beta = 1.5$ Å^{-1} was reported for the charge shift in acridine-modified DNA.[21, 22]

Obviously, the acridine system fulfills the injection conditions, and therefore seems to be suitable for charge transport studies. However, the results that were available at the beginning of the present work for the acridine–DNA system were based exclusively on emission measurements, which did not allow any intermediate state to be monitored, and therefore could not verify the electron transfer process.

Based on these prerequisites the injection kinetics in 9-amino-6-chloro-2-methoxyacridine-modified DNA duplexes has been revisited in the present work. Transient absorption spectroscopy has been employed to elucidate the origin of the steep distance-dependence of the rate constants for hole injection by monitoring the charge transfer intermediate states. These experiments illustrate the potentially complex nature of experimental β values and identify the contribution of a prominent but rarely recognized feature of ET theory, namely the medium reorganization energy.[24]

1.2.2 Complex between Fluorescein and an Engineered Lipocalin Protein

Whereas in DNA research main emphasis is placed on the elucidation of details of electron transfer processes it was the goal of this second project to investigate the underlying mechanism responsible for the observed fluorescence quenching effect in the complex between the pigment molecule fluorescein and an engineered protein.[25]

The high fluorescence quantum yield of the fluorescein dianion ($\Phi = 0.93$),[26] its easy synthesis, and its high chemical stability are responsible for its widespread application as a reporter pigment in chemistry and, in particular, in the biological sciences. Fluorescein and its chemically activated derivatives are generally used for the covalent labeling of biomacromolecules, including nucleic acids, proteins, and, especially, antibodies.[27] Antibodies raised against the fluorescein group often show a pronounced fluorescence quenching efficiency upon binding of this ligand. Such antibodies with high affinity and quenching effects on fluorescein have also been utilized in special experimental applications, e.g. in order to determine the orientation of transmembrane proteins that were site-specifically labeled with fluorescein[28] or to discriminate between free and bound states of a fluorescein-conjugated peptide ligand in biological cell surface receptor-binding studies.[29]

Recently, fluorescein was employed as a model target for the generation of a cognate anticalin, i.e., an engineered protein with tailored specificities derived from the lipocalin scaffold.[25] Lipocalins are small monomeric ligand-binding proteins that in nature play a role in transport or storage of lipophilic or chemically sensitive physiological compounds, for example, biliverdin IX_γ in the case of the bilin-binding protein.[27] Proteins of the lipocalin family share a characteristic polypeptide fold comprising a circularly closed eight-stranded anti-parallel β-sheet. This β-barrel is usually open to the solvent on one side and a set of four loops, each connecting a pair of neighboring β-strands, forms the entry to the ligand pocket. In contrast to the structurally conserved β-barrel, the loops vary considerably in length and conformation among different lipocalins, and thus determine their ligand specificities.[30] The lipocalin architecture resembles that of immunoglobulins, where a set of at least six hypervariable loops, which are supported on a rigid β-sheet framework, makes up the antigen-binding site.

In an attempt to reshape the ligand pocket of the bilin-binding protein via combinatorial protein design the fluorescein group served as a target for molecular recognition.[25] Using the methods of site-directed random mutagenesis and phage display,[31] an engineered lipocalin with high affinity for fluorescein, the anticalin FluA, was selected. In contrast to other cognate anticalins that were chosen along with FluA this protein exerted an almost complete quenching effect on the steady-state ligand fluorescence upon complexation ($Q_{max} = 99.7 \pm 0.3\%$).[25]

Such a quenching effect points to extremely strong and specific interactions between the ligand and a moiety of the protein matrix at the binding pocket leading to a fast depopulation of the excited fluorescein. The potential deactivation mechanisms considered here, such as excited-state electron, proton, and energy transfer processes,[32] differ in their intermediate states. In order to distinguish between them transient methods are required that not only monitor the depopulation of the primary excited state but also the identity and kinetic behavior of potential product states. In this work, the almost complete quenching phenomenon in the complex between fluorescein and the anticalin FluA, which surpasses known quenching effects described so far for anti-fluorescein antibodies, and the underlying physico-chemical mechanism are studied with femtosecond transient absorption measurements.

1.3 Overview of the Content

The following chapters are organized as follows: In Chapter 2 the experimental setup of the femtosecond laser system is described together with the preparation of the samples used. Chapter 3 surveys the basic concepts of nonadiabatic electron transfer theory as far as it is needed for data evaluation. Chapters 4–8 deal with photoinduced hole transfer in 9-amino-6-chloro-2-methoxyacridine-modified DNA duplexes. The distance dependence of hole injection rate constants from the photoexcited acridine to guanine and its analog 7-deazaguanine is discussed in Chapter 4. The photophysics of 9-amino-6-chloro-2-methoxyacridine in DNA in the absence of hole transfer is considered in Chapter 5. The temperature-dependent measurements presented in Chapter 6 allow a quantification of the influence of the activation energy on the distance dependence of the injection rates. The activated hole transfer in these DNA duplexes is employed to investigate in situ the hierarchy of oxidation potentials of modified purine nucleobases (Chapter 7). The topic of Chapter 8 is the investigation of the photoinduced dynamics in the complex between fluorescein and an engineered lipocalin protein. Finally, the results of this work are summarized.

2 Experimental Methods

The temporal evolution of the photoexcited charge transfer processes investigated in this work is followed by femtosecond transient absorption spectroscopy. An introduction to the principle of the time-resolved measurements and the laser systems used will be given in Section 2.1. The instrumentation utilized for the steady-state measurements and the preparation of the modified DNA and protein samples are described in Sections 2.2 and 2.3, respectively.

2.1 Time-Resolved Absorption Measurements

2.1.1 The Pump–Probe Technique

Time-domain pump–probe techniques have been applied to study ultrafast molecular phenomena in chemistry and biology with temporal resolution on the picosecond and femtosecond time scale.[33] The ultrafast resolution is achieved by beam-splitting a laser source with a very short pulse width and recombining the beams at the sample under investigation. The initiating pulse (pump pulse) triggers a photophysical or photochemical process. The response of the system can be sampled by comparing the modifications of a second pulse (probe pulse), delayed in time from the pump pulse, after crossing the sample before and after the action of the pump pulse.[34] By fine control of the optical paths of the two beams using high precision translation stages, the arrival of one beam can be delayed relative to the other by a well-defined amount. With this technique, molecular dynamics can be mapped at different times following the arrival of the initial excitation beam. In general, the temporal resolution of the pump–probe technique is limited only by the pulse width of the pulsed laser source.[34]

2.1.2 Differential Absorption Spectroscopy

In a typical transient absorption study, a strong pump pulse is used to excite molecules from their electronic ground state to an excited electronic state at time $t = 0$. Any dynamic process occurring after photoexcitation that affect the optical properties can then be monitored by the change in absorption of the weak probe pulse through the sample at time $t + \Delta t$. The quantity of interest is the differential absorption ΔA:

$$\Delta A = A_{\text{with}} - A_{\text{without}} \tag{2.1}$$

In this equation, A_{with} and A_{without} denote the absorption of the sample in the presence and in the absence of the pump pulse, respectively. The absorptions A can be calculated from the probe pulse intensity before (I_0) and after (I) the sample:

$$A = -\log \frac{I}{I_0} \tag{2.2}$$

Combination of Eqs. (2.1) and (2.2) yields

$$\Delta A = -\log \frac{I_{\text{with}}}{I_0} + \log \frac{I_{\text{without}}}{I_0} = -\log \frac{I_{\text{with}}}{I_{\text{without}}} \tag{2.3}$$

In principle, a measurement of the transient absorption can therefore be reduced to the detection of the transmitted intensity of the probe beam. Since this detection scheme cannot account for temporal changes of the intensity due to fluctuations of the laser system, the present experiments also involve the detection of I_0 (see Section 2.1.4).

In general, a differential absorption signal can comprise up to three different contributions from (1) the recovery of the ground state, (2) stimulated emission, and (3) excited-state absorption of the molecule and/or absorption of photoproducts.

This can be illustrated by a simple example (Fig. 2.1). A pump pulse is used to excite molecules from their electronic ground state to the first excited singlet state S_1. Because of the depletion of the ground-state population, the transmitted intensity of a probe pulse tuned to the wavelength range of the ground-state absorption increases, yielding a negative transient absorption signal. Additionally to the processes of internal conversion and spontaneous emission, molecules in the S_1 state may return to the ground state by stimulated emission. The intensity of the transmitted light is increased by stimulated emission ($I_{\text{with}} > I_{\text{without}}$), yielding a negative contribution to ΔA. Positive contributions to

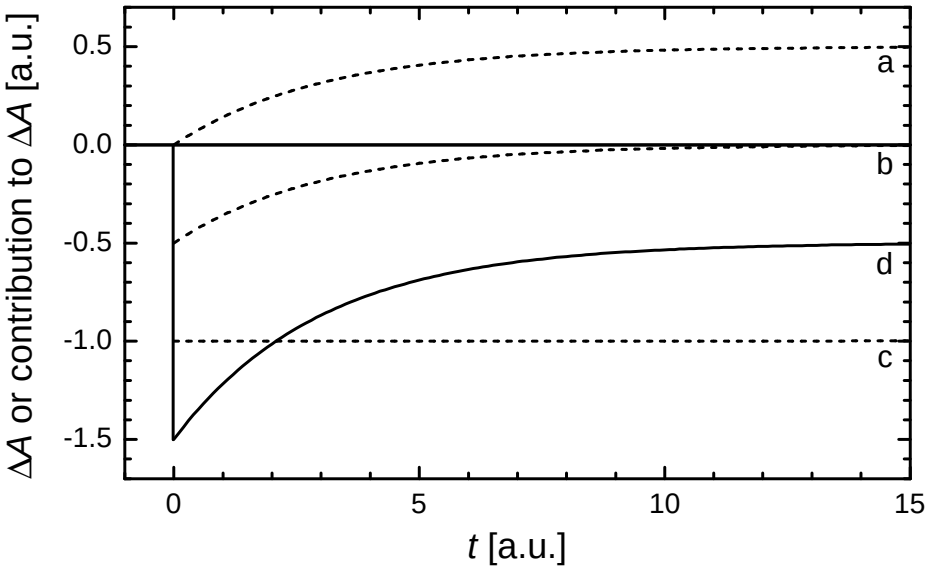

Fig. 2.1: Schematic reconstruction of a differential absorption signal consisting of (a) the absorption of a photoproduct, (b) stimulated emission, and (c) the recovery of the ground state. The observed signal (d) is the sum of the contributions (a)–(c).

the signal arise if the probe pulse induces absorptions of new electronic states created by the pump pulse. In addition to excited-state absorption from the first excited singlet state ($S_n \leftarrow S_1$), these may be due to transitions from triplet states or photoproducts, e.g. intermediate free radical or ion states.

Using the Beer–Lambert law

$$A = \varepsilon c d \tag{2.4}$$

which correlates the absorption to the sample thickness d, and the concentration of the absorbent substance c (ε denotes the wavelength-dependent extinction coefficient), the differential absorption signal can be related to the concentrations of the contributing species:

$$\Delta A(t) = -\varepsilon_g \sum_i c_i(t) d + \sum_i \varepsilon_i c_i(t) d = \sum_i (\varepsilon_i - \varepsilon_g) c_i(t) d \tag{2.5}$$

The subscript g refers to the ground state, whereas i refers to states populated after excitation. The temporal change of the concentrations c_i is reflected by a change of the differential absorption signal with time. Together with the wavelength dependence of the extinction coefficients, the temporal evolution of ΔA allows to identify the molecular states and species involved and to interrogate their kinetic behavior.

2.1.3 The Titanium:Sapphire Femtosecond Laser System

For the transient absorption measurements in this work two different amplified laser systems were employed, both based on titanium-doped aluminum oxide (Ti:sapphire, Ti:Al_2O_3) as the gain medium. The optical setup of these systems is similar and both have been described in detail elsewhere.[35, 36] A description of the laser system, which was used for most of the measurements, will be given in this section. The other setup is briefly described in Section 2.1.6.

Ultrashort pulses are generated with a commercial Ti:sapphire oscillator (Coherent MIRA 900 Basic) employing the concept of Kerr lens mode-locking, a technique simultaneously using the very large bandwidth of the laser medium[1] and its intensity-dependent index of refraction.[37] The optical cavity is designed to utilize changes in the spatial profile of the beam produced by self-focusing from the optical Kerr effect in the Ti:sapphire crystal. This self-focusing results in a higher round-trip gain in the modelocked versus continuous-wave (CW) operation due to an increased overlap between the pumped gain profile and the circulating cavity mode. In this setup, a pair of Brewster prisms is used to compensate for the group velocity dispersion introduced by the dispersive elements within the laser cavity. The oscillator is pumped by a CW argon ion laser in multiline operation (Coherent Innova 310) and produces pulses with a duration of ~100 fs (full width at half maximum, FWHM) at a central wavelength of 780 nm. The repetition rate f of 76 MHz is given by the length of the cavity L ($f = c/2L$). The average output power under mode-locking conditions is ~500 mW. Since the energy of a single pulse is only 0.01 μJ, the pulses must be amplified before they can be used for transient absorption experiments.

The amplification of nJ-level femtosecond pulses to the mJ range is complicated by the extremely high peak powers involved, which exceed the damage threshold of most optical materials. This problem is overcome by using the concept of chirped pulse amplification. The ultrashort pulse is not amplified directly, but first stretched and then amplified, before finally being recompressed. This technique also has the benefit of eliminating unwanted nonlinear effects in the amplifier materials.[37]

In the current setup, the pulses from the oscillator are temporarily broadened to ~180 ps using a stretcher with a grating as the dispersive element introducing positive group velocity dispersion.[2] Using a fast-switching Pockels cell (Medox), one out of 76 000 pulses is selected to seed a regenerative amplifier system (BMI Alpha 1000S) based on a Ti:sapphire crystal. Due to its large effective gain bandwidth (vide supra) this material is well suited for the amplification of femtosecond pulses.

---

[1] The emission spectrum of Ti:Al_2O_3 ranges from 650 to 1100 nm.[37]

[2] i.e. the red wavelengths go faster than the blue ones

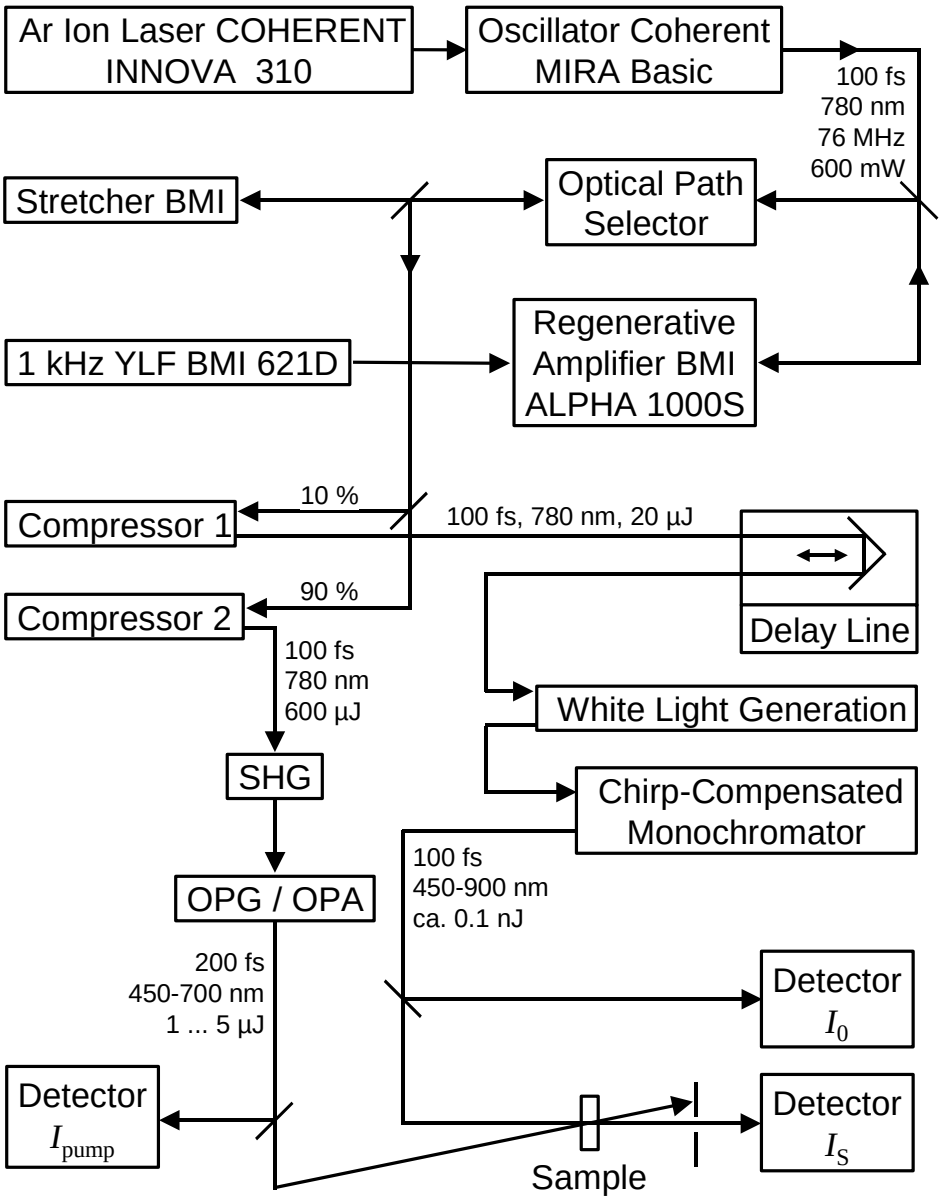

Fig. 2.2: Scheme of the setup of the amplified Ti:sapphire laser system used for the time-resolved transient absorption measurements.

Trapping and dumping the pulse is done using the Pockels cell and a broadband polarizer. The Pockels cell is initially set to be equivalent to a quarter-wave plate. When a pulse is in the resonator, the voltage of the Pockels cell crystal is switched so that it becomes equivalent to a half-wave plate. The Pockels cell is synchronized with the Q-switch of a Nd:YLF laser (BMI 621D), pumping the Ti:sapphire crystal of the amplifier with ~9 W at 528 nm. The pulse passes through the regenerative cavity several times before the gain is saturated, and a second voltage step is applied to extract the pulse.

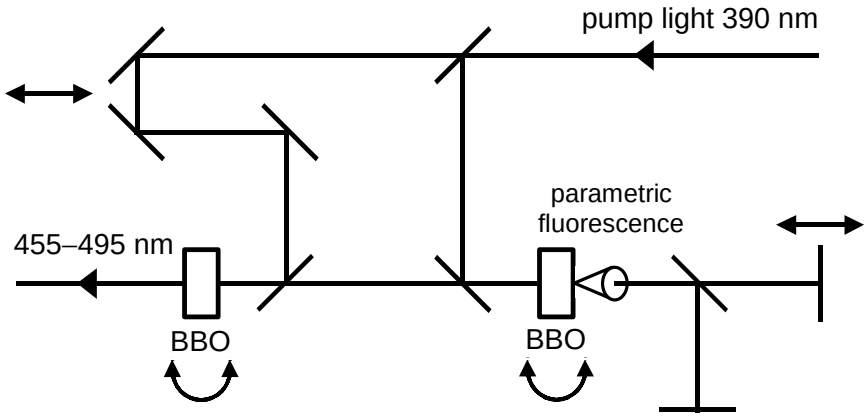

Fig. 2.3: Experimental setup of optical parametric generation and amplification. The first BBO crystal is used for both the parametric generation, as illustrated by the cone of parametric superfluorescence, and for the first stage of amplification. The parametrically generated light is further amplified using a second crystal. Also indicated are the wavelengths of the signal wave used for most of the experiments in this work.

A setup consisting of a Faraday rotator, a half-wave plate and a broadband polarizer is used to isolate the output pulse from the input. The amplified pulse train, now with a repetition rate of 1 kHz, is split into a pump and a probe pulse (9:1). After separate recompression with grating compressors with negative group velocity dispersion to match the dispersive characteristics of the stretcher optical pulses at 780 nm with a pulse duration of ~100 fs are obtained.

The pump pulses are frequency-doubled to 390 nm with a BBO crystal (β-Barium borate, β-$Ba_2B_2O_4$) and directed through an optical parametric generator (OPG) and two-stage amplifier setup (Fig. 2.3). A part of the input beam at 390 nm is incident on another BBO crystal cut at the correct angle to ensure phase matching. As a result of the optical parametric effect, signal and idler waves are generated. The wavelengths of these are determined by energy conservation and momentum conservation (through phase matching) in the nonlinear crystal. The pump beam and the parametrically generated light coming out of the crystal are redirected toward the crystal for a second pass, after being retimed together. For power amplification, the parametric amplified light and the rest of the input beam at 390 nm are directed toward a second BBO crystal.

For excitation the signal wave is selected by a band pass filter and passes through a chopper set to 500 Hz. This provides subsequent "pump-on" and "pump-off" conditions in the sample needed for the calculation of the differential absorption. A small fraction of the pump light is directed onto a detector which is used to correct fluctuations of the pump intensity (I_{pump}) in the signal.

The weaker probe pulses pass a variable delay line (up to 5 ns) and are focused into a 2 mm sapphire crystal. By self-focusing and self-phase-modulation a single filament white light continuum is produced that ranges from 450 nm to the near infrared. A chirp-compensated stepper motor-controlled spectrometer is used to select spectral regions with a bandwidth of 15 nm. The probe pulse intensities before (I_0) and after (I_S) the sample are detected by photodiodes. Pump and probe beams are focused at a cuvette containing the sample under a mutual angle of 10° with long focal length converging lenses. Using half-wave plates and polarizers, the relative polarizations between pump and probe beam are set to the magic angle (54.7°) to avoid rotational depolarization effects. The size of the pump and probe foci at the sample position can be adjusted by changing the position of the converging lenses. As measured by a CCD chip, the transverse profiles of the pump and probe pulses typically had diameters of 300 μm and 100 μm, respectively. The CCD chip is also used to adjust the overlap of pump and probe pulses.

The detector signals are digitalized in a 10 bit A/D converter which is connected to a PC. The data are processed by a C-language program which also controls the stepper motors and the translation stage.

For the measurements discussed in Chapter 4, the temperature of the samples was held fixed to 10 ± 2 °C using a home-built temperature controller that was moved perpendicularly to the probe beam to avoid sample bleaching. Temperature-dependent (Chapter 7) or low-temperature experiments (Chapter 8) were performed by placing the cuvette in a continuous-flow cryostat (Cryovac KONTI-Cryostat-Spektro 4) cooled with liquid nitrogen.

2.1.4 Calculation of the Transient Absorption Signal

The probe pulse intensities before (I_0) and after (I_S) the sample, and the pump intensity (I_{pump}) are used to calculate the transient absorption signal $\Delta A(t)$. Before each measurement the light intensity at negative delay times[3] is detected to correct the effects of scattering light caused by the pump pulse. The intensity of the scattering light $I_{scatter}$ is given by the difference in intensities I_0 and I_S measured in the presence and absence of the pump light.

$$I_{\text{scatter,S}} = I_{\text{S}}^{\text{with}}(-t) - I_{\text{S}}^{\text{without}}(-t) \tag{2.6}$$

$$I_{\text{scatter,0}} = I_{0}^{\text{with}}(-t) - I_{0}^{\text{without}}(-t) \tag{2.7}$$

[3] i.e. the pump pulses are delayed with respect to the probe pulses

The difference absorption ΔA_{corr} is calculated from the scattering light-corrected probe pulse intensities $I_{0,corr}$ and $I_{S,corr}$ according to:

$$\Delta A_{corr} = -\log \frac{I_{S,corr}^{with} / I_{0,corr}^{with}}{I_{S,corr}^{without} / I_{0,corr}^{without}} \tag{2.8}$$

The fluctuations of the incident and transmitted probe light, as measured by the detectors, are typically <1%. Pump pulses produced by optical parametric generation display fluctuations of about 10%. To increase the signal-to-noise ratio, typically 4000 single-shot measurements were averaged for a given delay between pump and probe pulses. Additionally, to correct for long-term fluctuations of the pump light, ΔA_{corr} is normalized with respect to the pump pulse intensity I_{pump}.

2.1.5 Numerical Analysis of the Measurements

Apart from the intrinsic kinetics of the sample under investigation, the experimental differential absorption signal also contains instrumental contributions. As stated before, the temporal resolution of the pump–probe technique is limited by the pulse width of the pump and probe pulses. Since the laser pulses used for the experiments have a finite temporal width, this is also true for the so-called instrument response function (IRF). This function depends likewise on the pulse duration of both the pump and the probe. The measured kinetics must be numerically corrected for the contribution from the IRF. In this work, this is done by fitting the experimental data $\Delta A(t)$ to a multiexponential decay function convoluted with the instrument response function $B(t-t_0)$ centered at t_0 using the Levenberg–Marquardt algorithm:

$$\Delta A(t) = \int_0^{+\infty} \left(\Delta A_0 + \sum_{i=1}^{n} \Delta A_i \exp\left(-\frac{t'}{\tau_i} \right) \right) \times B(t - t' - t_0) dt' \tag{2.9}$$

ΔA_i is the amplitude of a decay component with lifetime τ_i. ΔA_0 is the offset due to long-lived species. The instrument response function is modeled by a Gaussian with variable FWHM. The IRF of the setup described above has a FWHM of 200–250 fs. For every measurement, the residuals were calculated to assess the quality of the fit.

2.1.6 Femtosecond Pump–Probe Measurements with Excitation at 390 nm

All experiments with a pump wavelength at 390 nm were performed using a different amplified laser system. Briefly, ~150 fs, 390 nm pump pulses with a pulse energy of ~100 μJ are obtained by frequency doubling the 1 kHz, 780 nm output of a home-built amplified Ti:sapphire laser in a 2 mm BBO crystal.[36] Probe pulses are produced by focusing a small fraction of the amplifier output at 780 nm into a 2 mm sapphire crystal and using 10 nm band pass filters for wavelength selection. As in the other setup, the relative polarization between pump and probe beam was set to the magic angle (54.7°).

2.1.7 Nanosecond Pump–Probe Measurements

(performed together with I. Naydenova and R. Haselsberger)

Nanosecond decay times were determined using an absorption laser system that has been described in detail previously.[38] Pump pulses at 450 nm were generated by pumping a Coumarin 120 dye laser with the third harmonic of a Nd:YAG laser. Probe pulses were generated by a N_2-laser pumped dye laser. The delay time between excitation and probing pulse was adjusted electronically. The time resolution of this setup was ~2 ns.

2.1.8 Broadband Femtosecond Absorption Spectroscopy

(in cooperation with N. P. Ernsting, S. A. Kovalenko, J. L. Pérez Lustres, Institut für Chemie, Humboldt-Universität zu Berlin)

The broadband femtosecond transient absorption spectra discussed in Chapter 5 were measured after excitation at 396 nm with 40 fs pulses from a laser system based on a commercial Ti:sapphire laser (Femtolasers). The optical setup has been described in detail previously.[39] The output of the laser was split into two parts. One part was frequency doubled and provided pump pulses with a pulse energy of 0.2 μJ and a diameter on the sample of 150 μm. The other part formed the probe beam which was used to generate the supercontinuum in multiple filaments. The sample was continuously flowed through a cell with an optical path length of 650 μm. The excited volume was probed with a chirped supercontinuum with polarization parallel or perpendicular to that of the pump pulse. 200 single-shot spectra were averaged at 35 Hz for a given pump–probe delay. Additionally, a measurement with pure solvent was performed in order to obtain the coherent solvent signal which defines the pump–probe intensity crosscorrelation at every probe wavelength.

These data were then used to time-correct the resonant transient spectra and obtain the induced optical density $\Delta A(\lambda,t)$.[40] The time resolution of the experiment was 220 fs, limited by the optical path length. For measurements up to 70 ps time steps were typically 100 fs. All measurements were performed at room temperature.

2.2 Steady-State Measurements

Steady-state absorption spectra were obtained using a UV/Vis spectrometer (Perkin-Elmer Lambda 2S) with 2.0 nm resolution. Steady-state fluorescence spectra were recorded on a spectrofluorometer (Spex Fluorolog-2 Model F212I) with 1.7 nm resolution or better. In both spectrometers 1 mm path-length quartz cuvettes were used and fluorescence was detected using a front-face geometry. To perform low-temperature experiments the cuvette was placed in a continuous-flow cryostat (Leybold VSK 3-300) cooled with liquid nitrogen. Circular dichroism (CD) spectra were recorded on a Janus Scientific Jasco-715 CD spectrometer. Melting points were measured on a UV/Vis spectrometer (Cary 100) at 260 nm. The melting temperatures (T_m) of the oligodeoxynucleotides were calculated by determining the midpoints of the melting curves from the first-order derivatives.

2.3 Sample Preparation

2.3.1 The DNA Oligonucleotides

All DNA strands used in this study were ordered from Eurogentec (Köln, Germany) or Biospring (Frankfurt a. M., Germany), delivered lysophilized after polyacrylamide gel electrophoresis (PAGE) purification, and stored at −10 °C under the exclusion of light until shortly before use. Solutions of complementary single strands were made by dissolving each strand in a 10 mM Na_2HPO_4/NaH_2PO_4, 100 mM NaCl, pH 7.2 buffer solution. Modified single strands, internally labeled with 9-amino-6-chloro-2-methoxyacridine (X^+, see Fig. 4.1), were mixed with a 10% excess of unmodified counter strands present to help ensure that all X^+ chromophores would be located in a DNA duplex. Hybridization was performed by heating the mixed single strands to 80 °C, followed by slow cooling to room temperature over two hours. All samples had an adenine base opposite to X^+ on the counter strand. Based on the thermal stability and the fluorescence quantum yield it was reported that this base is most suited for fixing the chromophore into the DNA helix.[21] The hybridized spectroscopic samples were stored at 4 °C.

Samples had optical densities of about 0.3 at 450 nm in a 1 mm path-length quartz

cuvette (concentration approximately 0.3 mM). The observed kinetics were independent of the duplex concentration in the accessible range (0.05–1.5 mM). As evidenced by steady-state absorption spectra taken before and after time-resolved measurements, the oligonucleotide solutions were found to be very photostable. Deoxygenation of the samples by purging with argon had no effect on the observed kinetic behavior.

In view of the complexity of the system the preparation of the samples according to the above procedure was found to be remarkably reproducible. Time-resolved measurements on duplexes with identical sequences but with single strands from different batches yielded deviations in the observed lifetimes of <20%.

To increase the temperature range for the temperature-dependent measurements discussed in Chapter 6 buffer solutions containing sucrose were used. A sucrose stock solution was prepared by dissolving 24 g sucrose in 10 ml buffer (10 mM Na_2HPO_4/NaH_2PO_4, 100 mM NaCl, pH 7.2). Sample solutions containing sucrose were prepared by mixing equal volumes of a buffer solution (10 mM Na_2HPO_4/NaH_2PO_4, 1 M NaCl, pH 7.2) containing the hybridized duplexes and the sucrose stock solution. Sucrose acts as freezing point depression agent and maintains the samples in the liquid phase over the temperature range studied (245–305 K).

For CD spectroscopy, the X^+–DNA samples were diluted with additional buffer. For spectra in the 190–300 nm wavelength region samples had an optical density of 1.0 at 260 nm in a 10 mm path-length quartz cuvette (~3 μM). CD measurements from 300–600 nm were performed on samples with a concentration of 50–100 μM in 1 mm path-length cuvettes. CD spectra were corrected for the appropriate solvent blank. For melting point studies DNA samples were mixed in a 1:1 ratio of modified and complementary unmodified strands. Concentrations were ~3 μM in 10 mm path-length cuvettes. Samples were heated to 90 °C for 30 min and then cooled to 5 °C over 120 min.

2.3.2 The FluA Fluorescein Complex

(provided by A. Skerra, Lehrstuhl für Biologische Chemie, Technische Universität München)

The anticalin FluA was prepared as a recombinant protein by secretion into the periplasm of *E. coli* and purified by means of the *Strep*-tag as described previously.[25] Fluorescein (Fl) was purchased as sodium salt from Sigma (Deisenhofen, Germany) and a stock solution was prepared by dissolving 36.4 mg fluorescein in 100 ml buffer solution (phosphate-buffered saline (PBS), 1 mM EDTA, pH 8.0). The samples of fluorescein bound to FluA (FluA·Fl) used for all measurements contained 18 μl of fluorescein stock solution (967 μM) added to 150 μl of the FluA protein at 190 μM, dissolved in the same

buffer. The concentration of the chromophore was about 100 µM. For all measurements 1 mm path-length quartz cuvettes were used.

3 Theoretical Basics

In this chapter, the theoretical basics and principles of photoinduced electron transfer will be introduced. Since nonadiabatic electron transfer theory is the topic of numerous comprehensive accounts,[41, 42] emphasis will be placed on the concepts required for an understanding of the experiments presented in the following chapters.

3.1 Photoinduced Charge Transfer

In its most simple description, electron transfer is the result of the transition of a single electron from an initial molecular orbital (MO), the donor (D) state, to a MO of the final acceptor (A) state.[32] In a photoinduced electron transfer reaction the photoexcited molecule can act either as oxidizing or reducing species. Concentrating only on the HOMO and the LUMO[1] of the donor–acceptor complex Fig. 3.1 illustrates the possible pathways of ET. By optical excitation an electron of the donor is placed into the LUMO. The ET proceeds between the donor and acceptor LUMOs. Alternatively, an electron may move in the opposite direction from the acceptor HOMO to the donor HOMO. This process is usually called a hole transfer since the reaction can be alternatively understood as the motion of a missing electron (hole) from the donor to the acceptor. The ET processes discussed in the next chapters are of this type, i.e., the chromophores employed act as electron acceptors in their excited state.

Figure 3.1 suggests the possibility of a back reaction, where the transferred electron moves from the acceptor LUMO into the empty donor HOMO (Fig. 3.1a) or from the donor LUMO into the acceptor HOMO (Fig. 3.1b). In most cases the back transfer is slower than the forward reaction, although its driving force is larger. An explanation is given by nonadiabatic electron transfer theory which will be summarized in the next section.

[1] highest occupied and lowest unoccupied molecular orbital, respectively

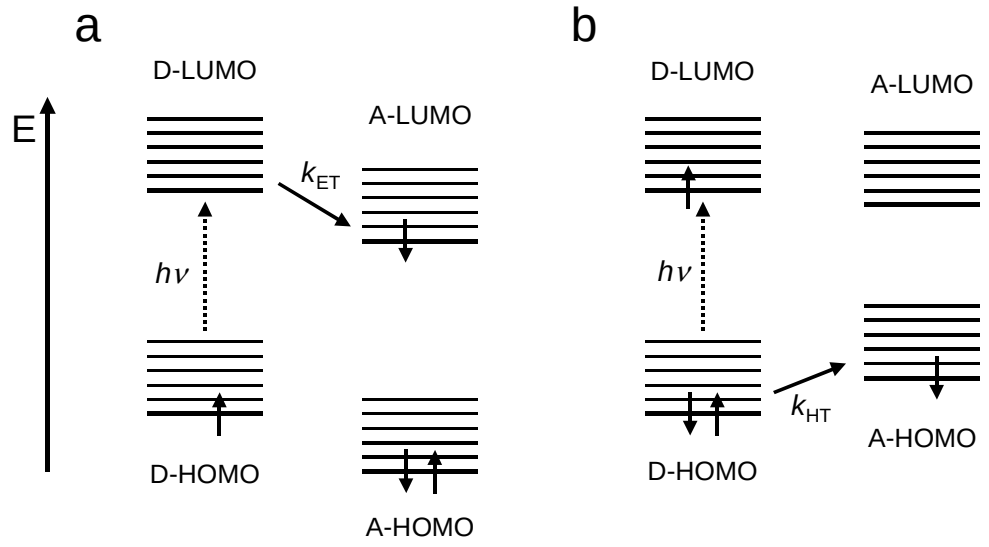

Fig. 3.1: Photoinduced charge transfer in a donor–acceptor complex. (a) Photoinduced electron transfer (ET), (b) photoinduced hole transfer (HT). Shown are the electron configurations of the product states. Thick lines and thin lines represent electronic and vibrational levels, respectively.

3.2 Fundamentals of Nonadiabatic Electron Transfer Theory

From the golden rule of perturbation theory, the rate constant for nonadiabatic electron transfer, with the Condon approximation, is given by:[42]

$$k_{\mathrm{ET}} = \frac{2\pi}{\hbar}\left|\langle R|H|P\rangle\right|^2 \left|\langle r_{\mathrm{vib}}\,|\,p_{\mathrm{vib}}\rangle\right|^2 \delta\left(E_{\mathrm{R}} - E_{\mathrm{P}}\right) = \frac{2\pi}{\hbar} V^2 FC \tag{3.1}$$

Here, the ET rate constant is given first in terms of the isolated levels of the reactant and product. $|r_{\mathrm{vib}}\rangle$ and $|p_{\mathrm{vib}}\rangle$ are vibrational states, $|R\rangle$ and $|P\rangle$ electronic states of reactant and product, respectively. $|\langle R|H|P\rangle| = V$ is the matrix element for electronic coupling between the donor and the acceptor, with *H* being the Hamiltonian of the entire system. *FC* denotes the density of states weighted Franck–Condon factor.

The distinction between nonadiabatic and adiabatic electron transfer is related to the magnitude of the electronic interaction between the reactant and product potential energy surface (Fig. 3.2). In the nonadiabatic limit the splitting at the barrier top, given by the crossing point of the curves, is very small. The formulation given in Eq. (3.1) is only correct in the limit of sufficiently weak coupling, i.e., for donors and acceptors at moderate

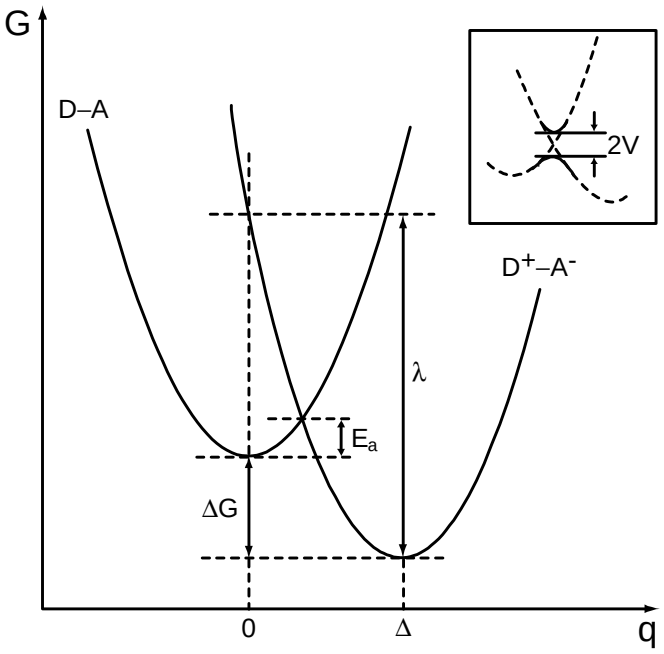

Fig. 3.2: Free energy curves for a D–A complex in harmonic approximation. q is the reaction coordinate. The definition of the driving force ΔG, the reorganization energy λ, and the free energy of activation E_a is indicated. Inset: The diabatic (dashed curve) as well as the adiabatic curves (full line) are shown. The splitting has a magnitude of $2V$ at the crossing point of the adiabatic curves.

to long distances. For this discussion, the presence of a nonadiabatic ET reaction will be assumed. Depending on the treatment of the nuclear degrees of freedom that contribute to the Franck–Condon factor, electron transfer theories can be divided into classical and quantum mechanical approaches.[2]

3.2.1 Classical Theory

Marcus derived a general expression for the ET rate constant from a thermally equilibrated vibronic manifold of the donor–acceptor potential surface, involving only the low-frequency medium modes in the high-temperature limit:[43]

$$k_{\mathrm{ET}} = \frac{2\pi}{\hbar}\frac{V^2}{\sqrt{4\pi\lambda k_{\mathrm{B}}T}}\exp\left[-\frac{(\Delta G+\lambda)^2}{4\lambda k_{\mathrm{B}}T}\right] \tag{3.2}$$

[2] In general, vibrational modes must be treated as quantum mechanical if $\hbar\omega >> k_BT$. When $\hbar\omega \approx k_BT$, the classical results are often reasonably accurate.[42]

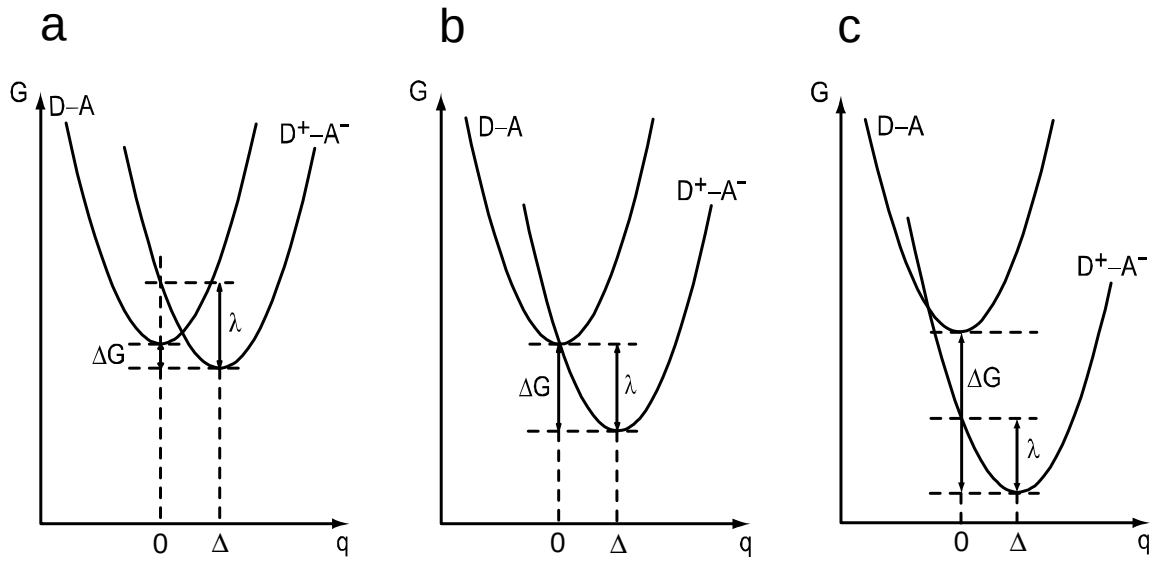

Fig. 3.3: (a) The normal region, (b) the activationless region, (c) and the inverted region of electron transfer in a D–A complex.

In Eq. (3.2) k_{ET} is expressed in terms of the reorganization energy λ and the free energy change of the reaction ΔG. k_B is the Boltzmann constant, and T the temperature.

In the derivation of Eq. (3.2) it is assumed that a quadratic function can adequately describe the free-energy surfaces of the reactant and product and that these two surfaces have identical curvature (Fig. 3.2). Importantly, Eq. (3.2) predicts that the electron transfer rate decreases with increasing $-\Delta G$ for strongly exoergic reactions and advances a universal classification of ET reactions to normal ($-\Delta G < \lambda$), activationless ($-\Delta G = \lambda$), and inverted ($-\Delta G > \lambda$) regions (Fig. 3.3). On the basis of Eq. (3.2) the free energy of activation E_a can be described by:

$$E_a = \frac{(\Delta G + \lambda)^2}{4\lambda} \tag{3.3}$$

From Fig. 3.2 a physical meaning of the reorganization energy can be deduced: λ is the change in free energy required to move the reactant atoms to the product configuration and to move the solvent molecules as if they were solvating the products without actually transferring the electron. λ contains contributions from the vibrations of the molecules (inner-sphere or intramolecular reorganization energy λ_v) and from the polarization changes in the dielectric solvent environment (outer-sphere or medium reorganization energy λ_s). The standard estimate for the latter was obtained by Marcus by using a model

in which reactants and products were modeled as conducting spheres and the medium as a dielectric continuum:[42]

$$\lambda_s = \frac{e^2}{4\pi\varepsilon_0}\left(\frac{1}{2r_D}+\frac{1}{2r_A}-\frac{1}{R}\right)\left(\frac{1}{\varepsilon_{op}}-\frac{1}{\varepsilon_s}\right) \tag{3.4}$$

In this equation r_D and r_A are the radii of the donor and the acceptor, respectively, and R the distance between their centers. ε_{op} and ε_s are the optical frequency and the static dielectric constants of the medium, e is the charge transferred, and ε_0 is the permittivity of free space. The difference in the inverse dielectric constants (Pekar factor) relates to the fact that nuclear degrees of freedom cannot readjust instantaneously to the motion of the electrons, a manifestation of the Born-Oppenheimer approximation.[42]

For photoinduced electron transfer reactions the free energy change ΔG can be calculated using the Rehm-Weller expression:[44]

$$\Delta G = E_{ox} - E_{red} - \Delta E_{00} + C \tag{3.5}$$

Here, E_{ox} is the oxidation potential of the ground-state donor, E_{red} is the reduction potential of the ground-state acceptor and ΔE_{00} is the zero–zero transition energy for optical excitation. To a first approximation, C is the Coulomb energy change resulting from ET between the donor and the acceptor. Under the assumption that the ions are spherical and using the Born equation to estimate the electrostatic solvation energy, the reaction free energy is given by[45]

$$\Delta G = E_{ox} - E_{red} - \Delta E_{00} + \frac{e^2}{8\pi\varepsilon_0}\left(\frac{1}{2r_D}+\frac{1}{2r_A}-\frac{1}{R}\right)\left(\frac{1}{\varepsilon}-\frac{1}{\varepsilon_{Ref}}\right)-\frac{e^2}{4\pi\varepsilon_0\varepsilon_{Ref}R} \tag{3.6}$$

where ε is the dielectric constant of the solvent in which the electron transfer reaction occurs, ε_{Ref} is the static dielectric constant of the solvent used to measure E_{ox} and E_{red}. The last term in Eq. (3.6) is the Coulomb stabilization of the product ions and the second to last term arises from the separation-distance-dependent solvation energy of the ion pair.

It follows from Eq. (3.6) that for a charge shift reaction, with donor–acceptor charges $\pm1, 0 \rightarrow 0, \pm1$ and donor and acceptor molecules of similar size and in similar environments, the distance dependence of ΔG can be neglected.[46]

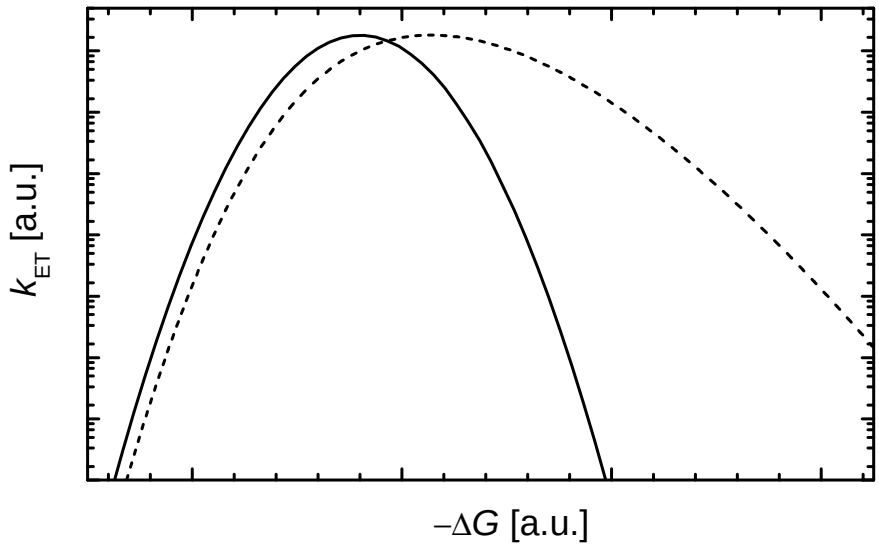

Fig. 3.4: Driving force dependence of the ET rate constant, involving only low-frequency medium modes (solid line), and in the presence of one high-frequency quantum mode (broken line). Calculated according to Eq. (3.2) and Eq. (3.7), respectively.

3.2.2 Quantum Mechanical Theory

For many systems Eq. (3.2) has been shown to be insufficient since it treats the nuclear system as a single effective classical degree of freedom. Therefore, theoretical models with one or more additional high-frequency quantum mechanical degrees of freedom must be employed. A generalization of Eq. (3.2) for nonadiabatic ET is given by the Marcus-Levich-Jortner equation, where the contribution of the quantum modes is subsumed into a single high-frequency mode ($\hbar\omega_c > k_B T$) with the frequency ω_c:[47-50]

$$k_{ET} = \frac{2\pi}{\hbar}\frac{V^2}{\sqrt{4\pi\lambda_s k_B T}}\exp(-S_c)\sum_{n=0}^{\infty}\frac{S_c{}^n}{n!}\exp\left(-\frac{(\Delta G + \lambda_s + n\hbar\omega_c)^2}{4\lambda_s k_B T}\right) \tag{3.7}$$

$$\text{where } S_c = \frac{\lambda_v}{\hbar\omega_c} \tag{3.8}$$

S_c is the dimensionless vibrational coupling constant (Huang–Rhys factor). Although expressions have been proposed that include many coupled vibrations explicitly, it appears to be generally applicable to account for the effects of the quantum behavior by treating only a few modes quantum mechanically by mode averaging.[42] For aromatic donors and acceptors, ω_c is often approximated by 1500 cm^{-1}, corresponding to the typical skeletal vibration in an aromatic compound. Observations indicate that this type of vibrations is

mostly involved in ion formation whereas high-frequency hydrogen modes seem to be of lesser importance.[51] Nuclear quantum effects result in a significant modification of the free energy relations in the inverted regime (Fig. 3.4). More specifically, Eq. (3.7) leads to a substantial slowing down of the decrease in the ET rate with increasing $-\Delta G$, due to the vibrational excitation of the quantum mode.

The vibronic theory also gives a far better representation of the temperature dependence of k_{ET} than Eq. (3.2) since it accounts for nuclear tunneling. This quantum effect is important for the transfer at low temperatures and in the inverted regime. Figure 3.3 shows that the tunneling barrier is expected to be substantially smaller in the inverted region than in the normal region. The vibrational overlap is higher and tunneling more efficient. Only a weak temperature dependence is seen in the ET rate constant because there is little increase in the vibrational overlap between the product vibrational states and levels above.

3.2.3 Superexchange-Mediated Electron Transfer

In a variety of environments, e.g. in proteins, the rate of long-range (>5 Å) electron transfer has been shown to fall off exponentially with distance.[42] If the separation exceeds the spatial extension of the wavefunctions of D and A, their direct interaction is negligible. Such long-range ET involves the mediation of the nonradiative process by the intervening molecular bridges (B), which control the process via electronic and/or vibronic coupling. For proteins and other insulating environments, there exists a large energy difference between the electronic origin of the DBA manifold and the energy of the oxidized and reduced states of the bridging medium (D^+B^-A or D^-B^+A). Consequently, coupling of the donor to the acceptor involves quantum mechanical tunneling of charge between a localized orbital on the donor and a localized orbital on the acceptor. The states D^+B^-A or D^-B^+A are virtual states that are not physically populated, i.e., the ET takes place in a single step.[52]

As described by Eqs. (3.2) and (3.7), with weak donor-acceptor coupling k_{ET} is predicted to vary with the square of the electronic coupling matrix element V. The distance dependence of the solvent motion barrier, Eq. (3.4), is included in the Franck–Condon factor. Due to the exponential decay of the electronic wave functions of the donor and acceptor V is predicted to fall off exponentially with distance:

$$V = V_0 \exp\left[-\beta \frac{(R - R_0)}{2}\right] \tag{3.9}$$

V_0 is the electronic coupling matrix element at the van der Waals separation R_0 and R the D–A center-to-center distance. β is a constant that reflects the decay of V with distance.

In general, it is assumed that the distance dependence of the electronic coupling is the dominant source of the distance dependence of the electron transfer rate constant:

$$k_{\mathrm{ET}} = k_0 \exp\left[-\beta\left(R - R_0\right)\right] \tag{3.10}$$

Only for systems in which the reorganization energy and the driving force vary negligibly with R the rate constant is predicted to reflect the distance dependence of V. For different classes of donor–acceptor systems β can vary substantially. The distance dependence of ET rates is especially well characterized in proteins. Reported β values typically fall in the range of 0.9–1.6 Å^{-1}.[53, 54]

Any detailed characterization of the distance dependence of an electron transfer reaction must separate the decay of the electronic couplings from the distance dependence of the reorganization energy λ and the free energy change ΔG. In terms of Eq. (3.2), the rate constant of the nonadiabatic electron transfer from a donor to an acceptor at a distance R is then given by:

$$k_{\mathrm{ET}}(R) = \frac{2\pi}{\hbar} \frac{V_0^{\,2} \exp\left[\left(-\beta\left(R - R_0\right)\right)\right]}{\sqrt{4\pi\lambda(R)k_{\mathrm{B}}T}} \exp\left(- \frac{\left(\Delta G(R) + \lambda(R)\right)^2}{4\lambda(R)k_{\mathrm{B}}T} \right) \tag{3.11}$$

4 The Apparently Anomalous Distance Dependence of Charge Transfer Rates in DNA Duplexes Modified by 9-Amino-6-chloro-2-methoxyacridine

In this chapter, the dynamics of photoinduced charge transfer in DNA duplexes containing a covalently appended, protonated 9-amino-6-chloro-2-methoxyacridine (ACMA) chromophore are investigated by means of femtosecond and nanosecond transient absorption spectroscopy. From fluorescence quenching experiments on a similar system, Fukui et al. have reported a steep distance dependence of the hole transfer rates.[21, 22] In the context of utilizing the ACMA–DNA system for a study of hole hopping dynamics in duplex DNA, the major focus of this study is on the origin of this steep distance dependence. The results discussed in this chapter are the basis for the more detailed investigation of this DNA donor–acceptor system in the following chapters. The chapter starts with an overview of recent results on the dynamics of superexchange ET in DNA.[1]

4.1 Introduction

The value of the tunneling parameter β for single-step superexchange electron transfer, Eq. (3.10), is one of the most contentious points in the literature on DNA electron transfer.[10, 60] The earliest estimates of the Barton group of β came from experiments utilizing DNA duplexes with hole injectors and acceptors tethered to the 5′ termini with long linkers.[6] The existence of ultrafast long-range ET was merely inferred from the absence of fluorescence intensity and a value $\beta \leq 0.2$ Å^{-1} was reported. Brun and Harriman extracted β from non-covalently attached intercalated donors and acceptors and obtained a value of about 0.9 Å^{-1}.[8] Whereas the β values reported from these and other experiments are in sharp disagreement, a reconciliation between them is not possible due to poor

[1] In addition to the single-step superexchange mechanism, which operates only over relatively short distances, charge transport can occur over long distances in DNA by multi-step hopping. This mechanism has recently been studied both experimentally and theoretically.[55-59]

structural definition of these ET systems. Other potential reasons leading to the observed large discrepancies in the reported β values have already been discussed in detail.[10]

A more precise definition of the donor–acceptor distance has become possible in oligonucleotides where the hole injector is either a specific ribose cation,[61] a covalently attached hole injecting chromophore,[9, 22] or a purine nucleobase[62, 63] which is capable of acting as a hole donating species. These newer assays have allowed studies on the dependence of both thermal and photoinduced hole transfer processes on the number of A:T pairs separating the donor and acceptor species. In the thermal hole transfer studies of Giese and coworkers hole transfer from a guanine cation, selectively oxidized by a deoxyribose radical cation, to a triple guanine (GGG) led to distance-dependent yields of strand cleavage products.[61] The dynamics of photoinduced charge transfer in duplex DNA have recently been investigated in several structurally well-defined systems. In the work of Tanaka and coworkers, the ACMA chromophore was covalently attached to a sugar–phosphate backbone using a proprioamide linker and resided inside the duplex by filling an abasic pocket.[21-23, 64, 65] Lewis et al. have investigated the distance dependence of photoinduced hole transfer for a family of synthetic DNA hairpins in which a stilbene dicarboxamide (SA) forms a bridge connecting two oligonucleotide strands.[9]

In spite of the different nature of the experiments reported by Giese et al. and by Lewis et al., both the yield of strand cleavage products as well as the directly measured hole injection rate constant have been reported to decrease exponentially with the number of A:T base pairs between the hole donor and guanine with a decay parameter in the range $\beta = 0.6–1.0$ Å^{-1}.[9, 66] This β range is larger than that observed for donor-acceptor systems connected by phenylene or alkene bridges, in which $\beta \leq 0.4$ Å^{-1}.[67, 68] However, it is significantly smaller than that for non-specific electron transfer pathways in proteins[53, 54] and rigid aliphatic bridges[69, 70] where β ranges between 0.9–1.6 Å^{-1}. A prominent exception to this range of β values in DNA arises in the experiments involving ACMA-labeled DNA duplexes, where the decrease in the hole injection rate constant with increasing distance is much steeper and $\beta = 1.5$ Å^{-1}.[22] On the theory front, β values in the range 0.6–0.8 Å^{-1} were substantiated by recent quantum chemical calculations.[71-74]

In the context of utilizing ACMA-labeled duplexes for charge hopping studies a detailed investigation of the origin of the large decay parameter is essential. The large β value reported for the ACMA–DNA system may be system inherent and the difference in the attenuation factors could originate from weak electronic coupling between the ACMA hole donor and the bridging A:T base pairs. In this case, charge hopping could be expected to favorably compete with the backward charge transfer. Moreover, the electronic couplings may be affected by large amplitude motions of this modified duplex, and therefore may be time-dependent. Contributions to the larger distance dependence in

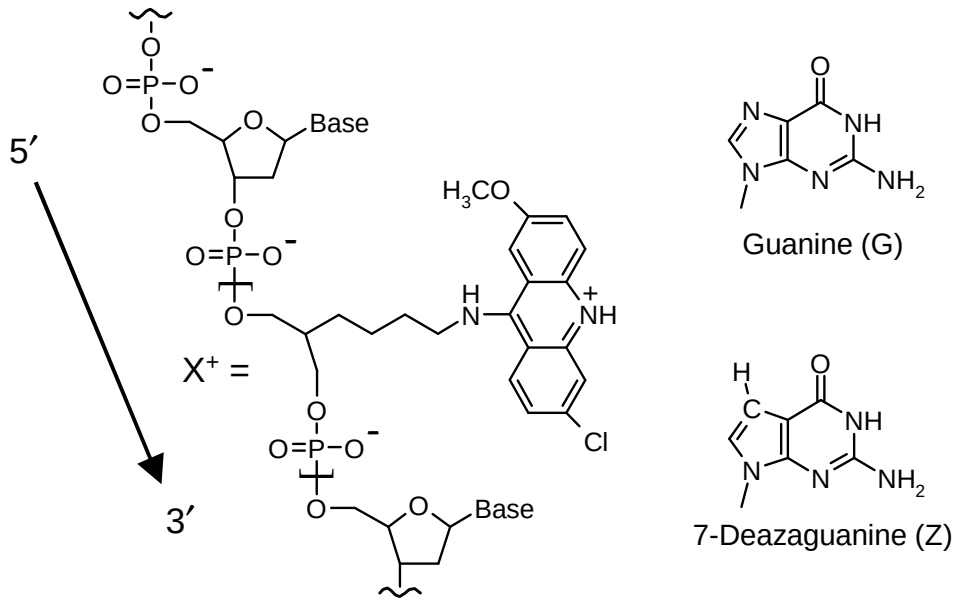

Fig. 4.1: Chemical structure of the 9-amino-6-chloro-2-methoxyacridine (X^+) modification utilized in this work and the structures of guanine (G) and 7-deazaguanine (Z).

ACMA–DNA duplexes could also result from a larger energy difference between the initial and bridge states.[75] In addition, some of the energy parameters which govern the hole transfer rate, such as ΔG and λ_s, may have a distance dependence of their own.[24, 76] This last hypothesis addresses an inherent problem of electron transfer theory which, in relation to DNA, has recently been approached in an explicit way.[46]

Moreover, it must be kept in mind that ACMA and its derivatives were reported to display complicated photophysics in aqueous solution.[77-79] Using steady-state and nanosecond time-resolved fluorescence measurements, Hélène and coworkers have reported a pronounced wavelength dependence of the fluorescence decay, i.e., a dynamic Stokes shift which has been assigned to an environmentally sensitive excited-state relaxation.[78] The relaxation time was reported to be solvent and temperature dependent with the fastest relaxation mode ranging from 100 ps in a mixed solvent of high viscosity (90% glycerol, 10% aqueous buffer) at 10 °C up to 2.5 ns in aqueous solution at room temperature. The relaxation mechanism was ascribed to the response of the polar solvent cage to an inferred 13 D increase in the molecules's dipole moment upon excitation.[78] Since in this work excited-state relaxation has been claimed to depend on the microenvironment of the chromophore in a specific way, intercalation of ACMA in the DNA duplex may influence the time scale of this relaxation process. Such an excited-state relaxation in the excited singlet state of ACMA could compete with ET and lead to a time-dependent driving force ΔG of the electron transfer process.

In the following, time-resolved transient absorption studies on a family of ACMA-

Duplex	1	2	3
X^+(AT)	A	A	A
5′-X^+G	G	A	A
5′-X^+AG	A	G	A
5′-X^+AAG	A	A	G
5′-X^+Z	Z	A	A
5′-X^+AZ	A	Z	A
5′-X^+AAZ	A	A	Z
3′-X^+G	A	A	G
3′-X^+AG	A	G	A
3′-X^+AAG	G	A	A
3′-X^+Z	A	A	Z
3′-X^+AZ	A	Z	A
3′-X^+AAZ	Z	A	A

Duplexes X^+(AT) and 5′-X^+

5′-GCG TTA TAT A(**X^+**)**1 23**T TAT GCG-3′

Duplexes 3′-X^+

5′-GCG TTA T**12 3**(**X^+**)A TAA TAT GCG-3′

Duplex $X^+(AT)_{13}$

5′-GCG TAA (**X^+**) AAT GCG-3′

Duplex 3′-X^+G_{13}

5′-GCG TAG (**X^+**) AAT GCG-3′

Fig. 4.2: Nucleobase sequences of the X^+-modified single strands. The counter strands utilized to produce the duplexes are not shown. However, all nucleobases were placed in a standard Watson–Crick pair and an adenine was placed opposite to X^+, similar to the previous work by Tanaka and coworkers.[21]

labeled DNA duplexes are presented. In these systems the photoexcited acridine derivative acts as a hole injector and guanine as the hole acceptor (Fig. 4.1). Three observables are monitored in these experiments: (1) the decay of the excited singlet state, (2) the formation of the hole transfer intermediate, and (3) the recovery of the ground state of the chromophore. From this data, the hole transfer rates as well as the underlying charge transfer mechanism will be investigated as a function of the ACMA–G distance. In addition, the energetics of the ET reaction will be varied through replacement of the electron donor guanine with its easier-to-oxidize analog 7-deazaguanine (Z).[80, 81] The chemical structure of the 9-amino-6-chloro-2-methoxyacridine modification (from now on denoted as X^+) utilized in this work is shown in Fig. 4.1, together with the structures of G and Z. Similar to the previous work by Tanaka et al.,[21] the chromophore is covalently attached to the backbone at an artificial abasic site by a tetramethylene linker. This modification is placed at the center of a 21 base pair oligonucleotide and hybridized to its Watson–Crick complementary strand according to the procedure given in Chapter 2. The sequences of the X^+-modified strands employed are given in Fig. 4.2.

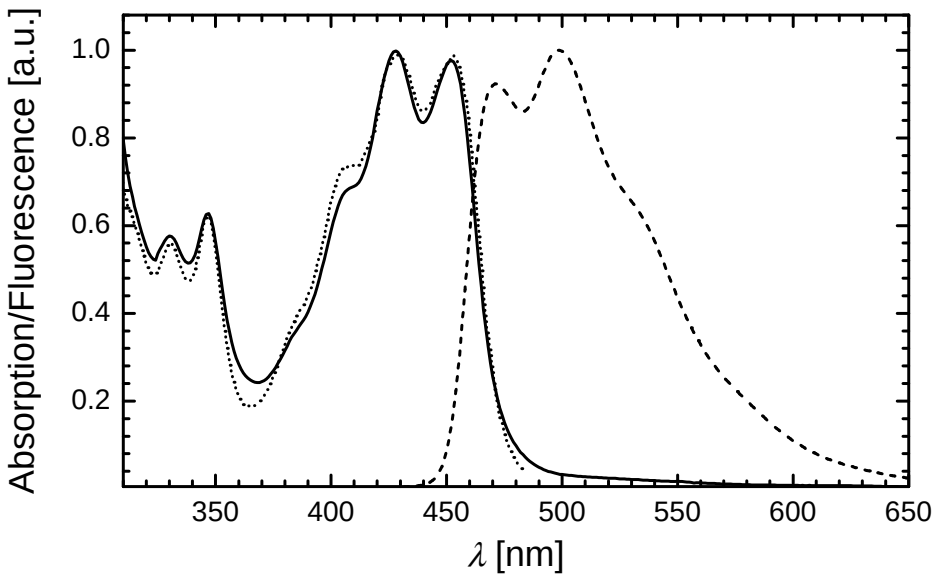

Fig. 4.3: Normalized absorption (—), fluorescence emission (---), and fluorescence excitation (·····) spectra of X^+ in duplex X^+(AT) at 283 K. The fluorescence was excited at 390 nm and fluorescence excitation was probed at 500 nm.

4.2 Experimental Results

4.2.1 Steady-State Spectroscopy

The absorption and fluorescence spectra of duplex X^+(AT) shown in Fig. 4.3 are representative examples for all duplexes studied here. The absorption spectrum is characteristic of an intercalated 9-amino-6-chloro-2-methoxyacridine chromophore, with $S_1 \leftarrow S_0$ absorption vibronic bands at 452, 428, and 405 nm and $S_2 \leftarrow S_0$ vibronic bands at 344 and 328 nm.[82] The absorption peaks are red-shifted by ≥4 nm compared to the chromophore in solution (see Fig. 5.4). This hypochromic effect is due to stacking interactions between the dye and the neighboring nucleobases.[22]

The fluorescence spectrum of X^+(AT) was obtained using excitation at 390 nm. It shows a main peak at 499 nm and two side bands at 471 nm and 530 nm. The strong increase in fine structure, as compared to quinacrine in solution (Chapter 5), in both the absorption and emission spectrum is indicative of a well-defined rigid X^+ environment. The bands are separated by approximately 1250 cm^{-1} in agreement with previous assignments, probably reflecting a vibration of the polycyclic aromatic ring structure.[83] The fluorescence excitation spectra, both at 470 and 500 nm emission wavelengths, closely follow the X^+ absorption spectrum, as shown for X^+(AT).

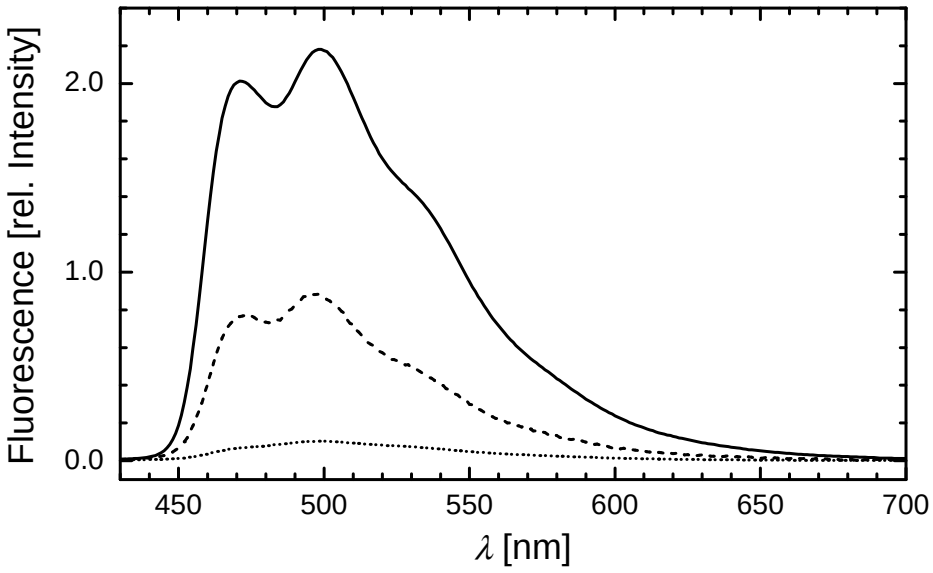

Fig. 4.4: Comparison of the relative fluorescence intensity in duplexes X^+(AT) (—), 3′-X^+AG (---), and 3′-X^+G (·····).

The steady-state fluorescence yield from X^+ was found to be highly dependent upon the nucleobase sequence flanking this chromophore (Fig. 4.4). In samples containing Z a lower fluorescence intensity (vide infra) was detected compared to analog duplexes with guanine. Independent of the direction along the helix (3′ or 5′) almost complete quenching of X^+ fluorescence was found for the duplexes X^+Z, X^+G, and X^+AZ, whereas X^+AAZ, X^+AG, and X^+AAG showed significant fluorescence yields.

The CD spectra of all X^+-labeled duplexes investigated display a positive band at ~277 nm, a negative band at 250 nm, and a crossover around 260 nm, indicative of an overall B-form DNA structure (Fig. 4.5).[84] Moreover, although 9-amino-6-chloro-2-methoxyacridine itself is achiral, an induced CD spectrum can be observed for the intercalated chromophore. All duplexes have a negative CD band which is a mirror image to the X^+ $S_1 \leftarrow S_0$ absorption band and a positive CD band around 350 nm, corresponding to the $S_2 \leftarrow S_0$ transition (Fig. 4.6). Induced CD spectra arise from strong interactions of the electronic transition moments of X^+ with the chirally arranged transition moments of the neighboring nucleobases. The induced CD bands shown in Fig. 4.6 have been reported to be indicative for ACMA intercalation.[85]

All these findings point to a well-defined rigid X^+ environment in the modified DNA duplexes, irrespective of the specific nucleobase sequence.

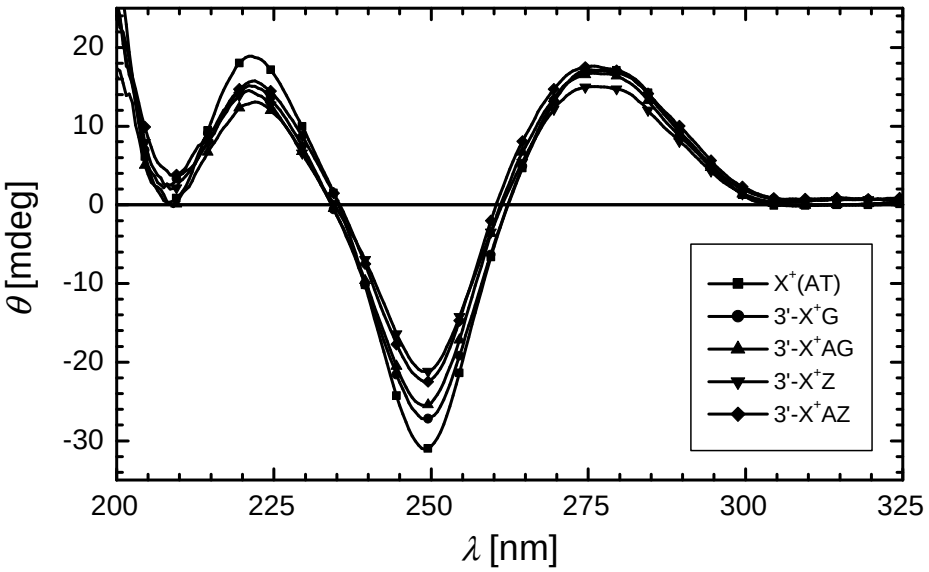

Fig. 4.5: Circular dichroism spectra of representative duplexes at pH 7.2 in 10 mM sodium phosphate buffer. The ellipticity (θ) spectra show the typical B-form signature of a positive band centered near 275 nm, a negative band near 250 nm, and a crossover at ~260 nm. For details see Section 2.3.1.

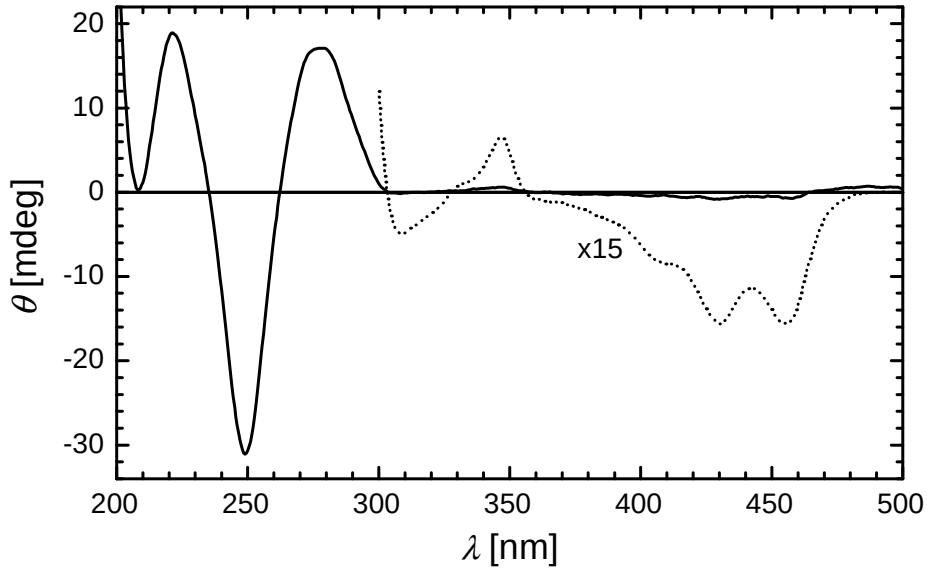

Fig. 4.6: Circular dichroism spectrum of duplex X^+(AT) at pH 7.2 in 10 mM sodium phosphate buffer. The strong interactions between the chromophore and the chirally arranged base pairs lead to an induced CD spectrum in the visible and near-UV wavelength range. For clarity the induced spectrum has been scaled by a factor of 15.

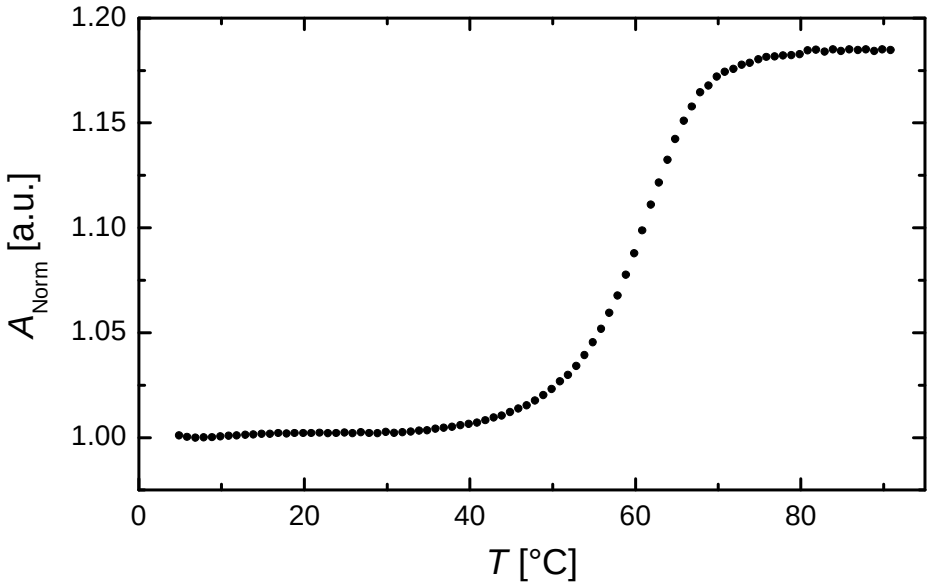

Fig. 4.7: Melting curve of the duplex 3′-X^+G_{13} at 260 nm, in 10 mM sodium phosphate buffer, 100 mM NaCl at pH 7.2. The melting temperature was determined to T_m = 58 °C. A_{Norm} is the absorption at temperature T normalized to the absorption intensity at low temperatures.

Moreover, incorporation of X^+ into an abasic site leads to an increase in melting temperature of the modified duplex as compared to an unmodified duplex. Since the relative change in the melting behavior due to replacing a thymidine phosphate with the X^+ modification is expected to be more pronounced in shorter sequences, this effect was studied with the 13-base pairs duplexes $X^+(AT)_{13}$ and 3′-X^+G_{13} (the sequences are shown in Fig. 4.2). For $X^+(AT)_{13}$ a melting temperature of 54.5 °C is found, as compared to 53 °C for an unmodified analog under identical conditions. For the duplex 3′-X^+G_{13} the measurement yields 58 °C in comparison to 56 °C for an identical sequence containing a thymidine phosphate instead of X^+. A representative melting curve is shown in Fig. 4.7. The increase of 1–2 K in the melting temperature in ACMA-modified duplexes is in accord with previous results[65] and can be attributed to strong π–π and dipolar interactions between the intercalated chromophore and neighboring nucleobases. Such a tight binding situation can also be deduced from a forthcoming 2D-NMR structure.[2]

[2] in cooperation with H. Neubauer und C. Griesinger (Max-Planck-Institut für Biophysikalische Chemie, Göttingen)

4.2.2 Transient Absorption Spectroscopy

Femtosecond pump–probe measurements were performed using two amplified Ti:sapphire laser systems differing in time resolution and excitation wavelength (Section 2.1). For measurements with a probe wavelength of 450 nm excitation pulses at 390 nm were used, whereas for all other measurements the excitation was tuned to 455 nm. Both 390 and 455 nm pump pulses allow for excitation of the $S_1 \leftarrow S_0$ transition of the chromophore (Fig. 4.3). Unless explicitly stated otherwise the experiments presented in this section refer to duplexes labeled by 3′-X^+ in Fig. 4.2.

Excited-State Dynamics of the Reference Duplex X^+(AT)

Upon photoexcitation of X^+ in the duplex X^+(AT), several transient features are observed in the spectral region between 450 nm and 850 nm. These correspond to excited-state absorption (550–850 nm), ground-state recovery (<460 nm), and stimulated emission (470–530 nm). Whereas the values in brackets indicate the wavelength range dominated by the corresponding transition, it should be emphasized that especially the excited-state absorption spectrum is very broad and probably has a non-negligible contribution even at $\lambda < 500$ nm. Figure 4.8a shows the kinetic traces of X^+(AT) obtained at probe wavelengths of 650 nm, 500 nm, and 450 nm. All traces are monoexponential and show lifetimes >5 ns.[3] Using nanosecond time-resolved absorption spectroscopy on a laser system allowing probing in the nanosecond to millisecond time window, the monoexponential lifetime of $^1(X^+)^*$, measured using 455 nm pump and 650 nm probe pulses, is 18 ns. This value is in reasonable agreement with the fluorescence decay time of 22.8 ns reported for a similar ACMA-labeled duplex containing only A:T base pairs in the proximity of the chromophore.[22]

[3] The fast recovery features seen in the kinetics under 390 nm pump and 450 nm probe conditions are instrument limited and seem to be an artifact. This is strongly supported by the broadband absorption spectra for X^+(AT) (Fig. 5.2), which do not show any indication of a femtosecond component.

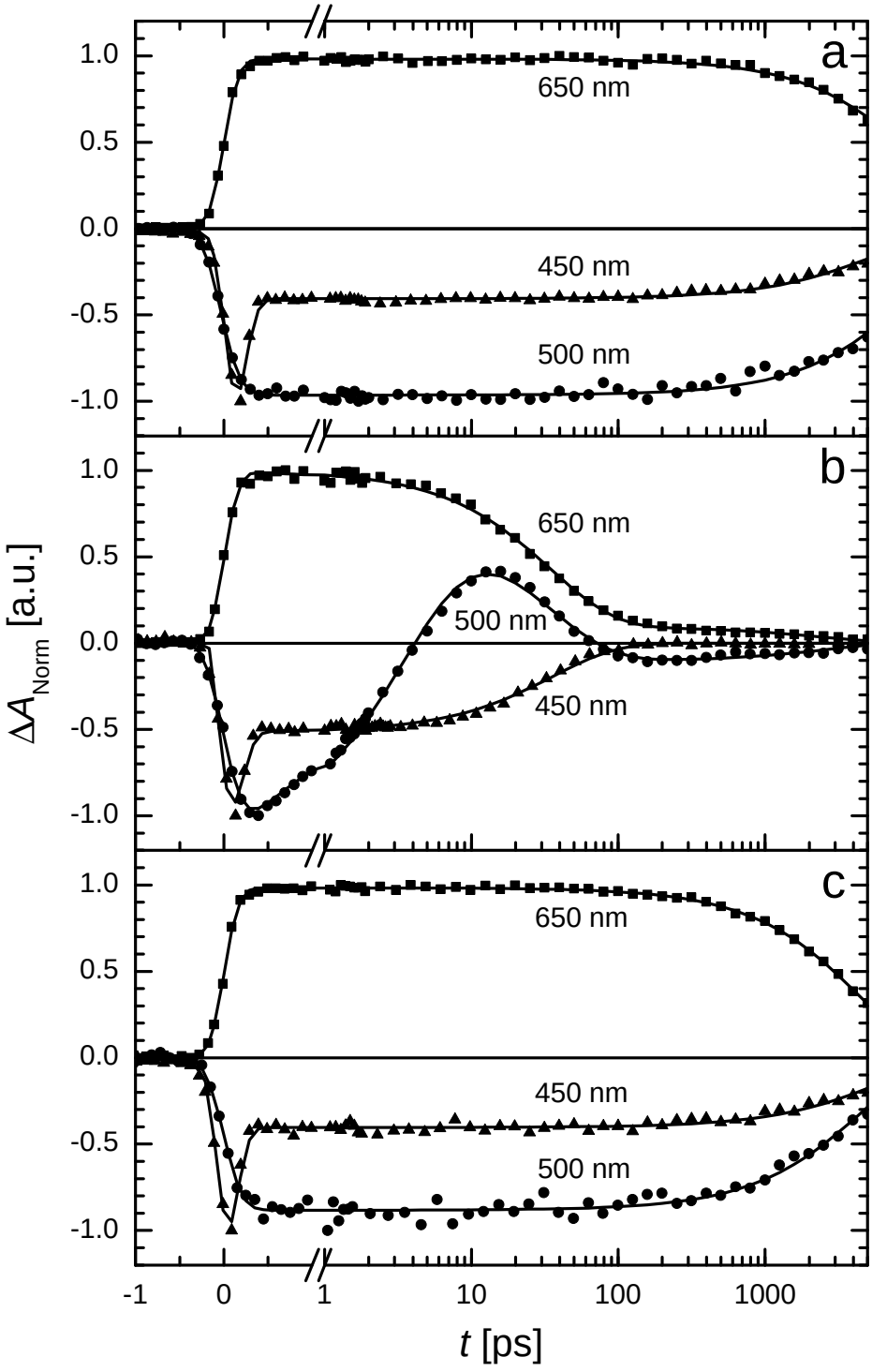

Fig. 4.8: Transient pump-probe kinetics measured in duplexes (a) X^+(AT), (b) 3′-X^+G, and (c) 3′-X^+AG. 390 nm, ~150 fs pump pulses were used for excitation when probing at 450 nm and 455 nm ~200 fs pump pulses were used when probing at all other wavelengths. The probe wavelength used for each kinetic trace is noted in (a)–(c). The solid lines are nonlinear least-squares fits to the data, whose fit parameters are listed in Table 4.1.

Hole Transfer Dynamics in the Different G and Z Containing Duplexes

When a G:C base pair is placed next to X^+, duplex 3′-X^+G, a new positive feature is observed in the stimulated emission region (Fig. 4.8b) which rises with a time constant of 3.8 ps and decays with 35 ps. In previous transient absorption measurements on other acridine derivatives, broad radical absorption bands were observed in the visible region. Poulos et al. have reported that the 10-methylacridinyl radical absorption spectrum in an acetonitrile-water mixture ranges from 450 to 550 nm with a maximum around 500 nm.[86] The radical of non-derivatized acridine was also found to show a broad absorption band around 500 nm, extending into the 600 nm range in some solvents.[87] Therefore, this new band observed around 500 nm is assigned to absorption of the product state $X^\bullet$ formed via picosecond photoinduced hole transfer from $^1(X^+)^*$ to G:

$$^1(X^+)^* + G \rightarrow X^\bullet + G^{\bullet+} \tag{4.1}$$

This assignment is supported by the finding that the decay time of this positive band matches the observed recovery time of the X^+ ground state (450 nm probe). Accordingly, the $X^\bullet$–$G^{\bullet+}$ radical pair recombines in a reverse hole transfer process, leading to G and X^+ in the ground state:

$$X^\bullet + G^{\bullet+} \rightarrow X^+ + G \tag{4.2}$$

It should be noted that there is no evidence for an absorption of the guanine radical cation at 450 nm. This may be due to several reasons. The extinction coefficient of $G^{\bullet+}$ at this wavelength is only about 2000 $M^{-1}cm^{-1}$.[88] Compared to the cross section of the bleached $S_1 \leftarrow S_0$ ground-state absorption,[4] only a minor contribution from the absorption of the guanine radical cation is expected. Additionally, the excited-state absorption band of X^+ probably extends into this wavelength range[5] leading at least to a partial cancellation of the contributions of these two components to the observed signal. In X^+(AT) the positive feature at 650 nm is excited singlet state absorption. However, in the duplex 3′-X^+G both $^1(X^+)^*$ and $X^\bullet$ absorb at this wavelength, and as hole transfer occurs there is an evolution between the two states which masks the rise characteristics of $X^\bullet$. For probe wavelengths tuned further to the red (>650 nm) the absorption from the excited state dominates yielding kinetics with two decay components: a ~4 ps component corresponding to the excited-state

[4] $\varepsilon_{450} \approx 9500\ M^{-1}\ cm^{-1}$ for 9-amino-6-chloro-2-methoxyacridine[89]

[5] This can be concluded from the strong contribution of the excited-state absorption to the difference absorption signal at wavelengths around 430 nm (see Fig. 5.2).

lifetime and a 35 ps component corresponding to the lifetime of the radical. Another important feature of all measurements is that both the charge shift rate and the back transfer rate are monoexponential, and only a small fraction (<10%) of long-lived background signal is observed in the transient kinetics.

Placement of one A:T pair between X^+ and guanine (3′-X^+AG) changes the observed transient absorption features back to those found for the reference system X^+(AT) (Fig. 4.8c). The $X^\bullet$ band is not observed and the kinetics of the ground-state recovery of X^+, as well as the decay of $^1(X^+)^*$ monitored using the stimulated emission lifetime and the lifetime of the 540–850 nm band, are again monoexponential with lifetimes >5 ns. Nanosecond transient absorption measurements yield the kinetics listed in Table 4.1 for this duplex. Both the ground-state recovery and the excited-state decay are faster in 3′-X^+AG than those measured in X^+(AT), implying a guanine-specific quenching mechanism for $^1(X^+)^*$ in this duplex. When two A:T base pairs are placed between X^+ and G, duplex 3′-X^+AAG, there is no excited-state quenching of X^+, indicating the absence of hole transfer in this duplex.

After placing a Z:C base pair next to X^+, duplex 3′-X^+Z, the transient absorption features resemble those observed for 3′-X^+G. The product state $X^\bullet$, monitored at 500 nm, is formed within 700 fs and decays with a lifetime of 6.4 ps (Fig. 4.9a).[6] The hole transfer processes are analogous to those in Eqs. (4.1) and (4.2), involving 7-deazaguanine as hole acceptor instead of guanine:

$$^1(X^+)^* + Z \rightarrow X^\bullet + Z^{\bullet+} \tag{4.3}$$

$$X^\bullet + Z^{\bullet+} \rightarrow X^+ + Z \tag{4.4}$$

The ultrafast decay of $^1(X^+)^*$ is consistent with the observation that 3′-X^+Z is almost nonfluorescent in steady-state measurements. Once again, single exponential forward charge shift and back transfer kinetics are observed in this duplex with negligible background signal.

Unlike in duplex 3′-X^+AG, the placement of a single A:T pair between X^+ and Z in duplex 3′-X^+AZ does not result in the disappearance of the $X^\bullet$ signal (Fig. 4.9b). Both the forward charge shift and the back transfer lifetimes slow down by a factor of about 15 with respect to their counterparts in 3′-X^+Z. However, placing two A:T base pairs between X^+ and Z does result in transient dynamics resembling those of duplex 3′-X^+AG, (Fig. 4.9c).

[6] The positive feature observed in the stimulated emission region probably also contains a contribution from excited-state absorption.

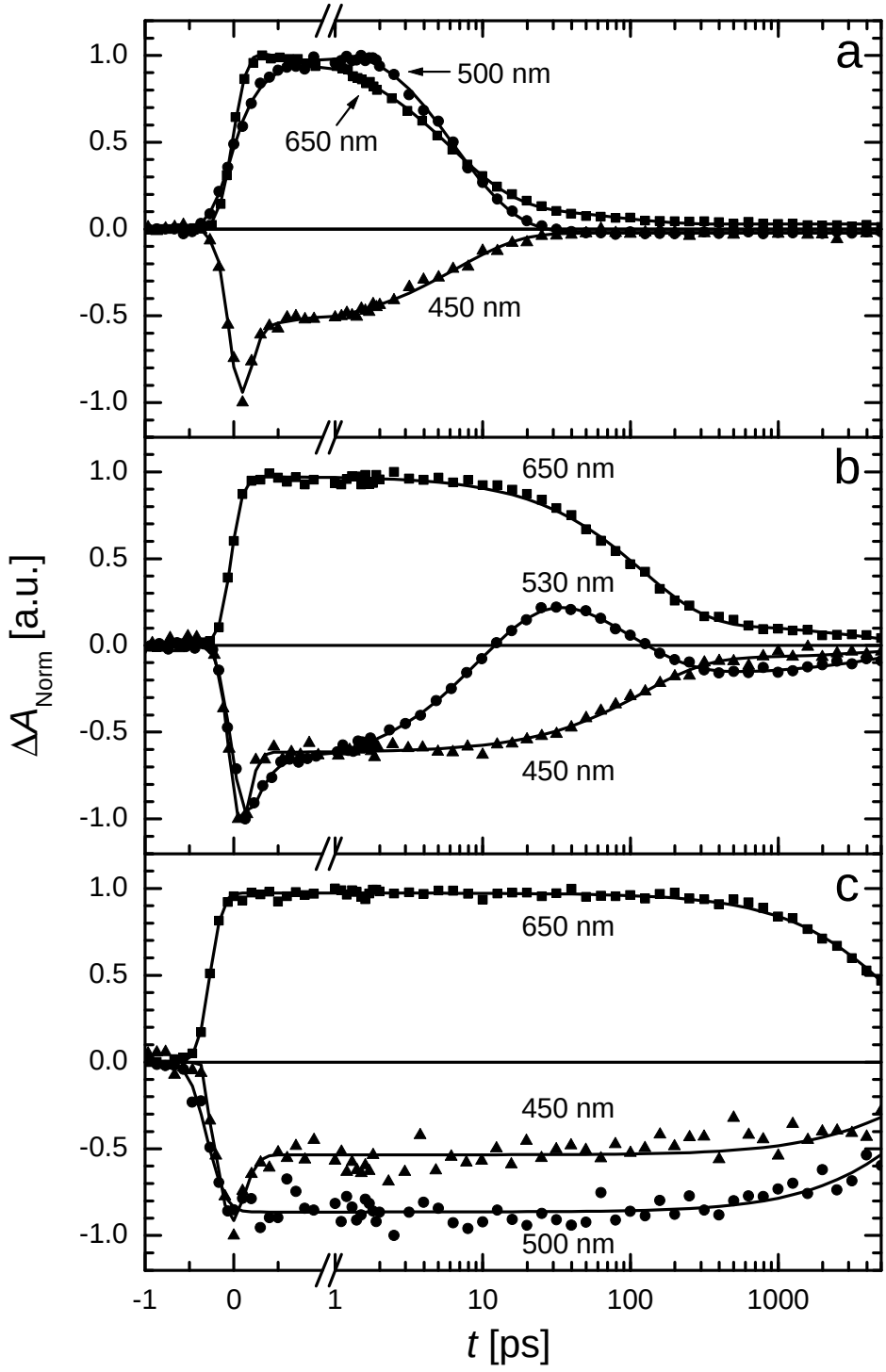

Fig. 4.9: Transient pump-probe kinetics measured in duplexes (a) 3′-X^+Z, (b) 3′-X^+AZ, and (c) 3′-X^+AAZ. 390 nm pump pulses were used for excitation when probing at 450 nm and 455 nm pump pulses were used when probing at all other wavelengths. The solid lines are nonlinear least-squares fits to the kinetic data, whose parameters are listed in Table 4.1.

In 3′-X^+AAZ, there is no observation of $X^\bullet$ and the kinetics of ground-state recovery and excited-state decay can be characterized by lifetimes >5 ns. Nanosecond transient absorption spectroscopy shows that the kinetics of ground-state recovery and excited-state decay of X^+ are monoexponential with identical rates, and faster than those observed in X^+(AT).

Directionality of the Hole Transfer Dynamics

In addition to the 3′-X^+ duplexes, hole transfer occurring in the opposite helical direction (5′-X^+ duplexes) was also studied. In all 5′-X^+ duplexes spectral features identical to those discussed above for their corresponding 3′-X^+ counterparts are observed. The lifetimes of

Table 4.1: Numerical parameters of the fit functions displayed in Figs. 4.8 and 4.9.

Duplex	λ_{Probe}	τ_1 [ps]	ΔA_1	τ_2 [ps]	ΔA_2	τ_3 [ns][b]	ΔA_3
X^+(AT)	650	-	-	-	-	>5 (18)	1.00
	500	-	-	-	-	>5	–1.00
	450[a]	-	-	-	-	>5	–1.00
3′-X^+G	650	-	-	35	0.91	2.5	0.09
	500	3.8	–0.66	34	0.30	3.5	–0.04
	450[a]	-	-	36	–1.00	-	-
3′-X^+AG	650	-	-	-	-	>5 (6.9)	1.00
	500	-	-	-	-	>5	–1.00
	450[a]	-	-	-	-	>5 (7.4)	–1.00
3′-X^+Z	650[c]	-	-	5.8	0.84	3.5	0.04
	500	0.7	–0.34	6.4	0.65	-	-
	450[a]	-	–1.0	6.8	-	-	-
3′-X^+AZ	650	9	–0.06	105	0.81	3.3	0.13
	530[d]	11	–0.48	98	0.26	>5	–0.06
	450[a]	-	-	122	–0.87	>5	–0.13
3′-X^+AAZ	650	-	-	-	-	>5	1.00
	500	-	-	-	-	>5 (8.4)	–1.00
	450[a]	-	-	-	-	>5	–1.00

$\Delta A_{1,2,3}$ are the relative amplitudes of the time constants $\tau_{1,2,3}$. [a] Excitation wavelength: 390 nm. [b] The time constants in the nanosecond region cannot be determined precisely as the delay line is restricted to times below 6 ns. Values in parentheses were measured with the nanosecond pump-probe setup. [c] Additional unassigned time constant of 42 ps (12%). [d] Additional unassigned time constant of 150 fs (20%).

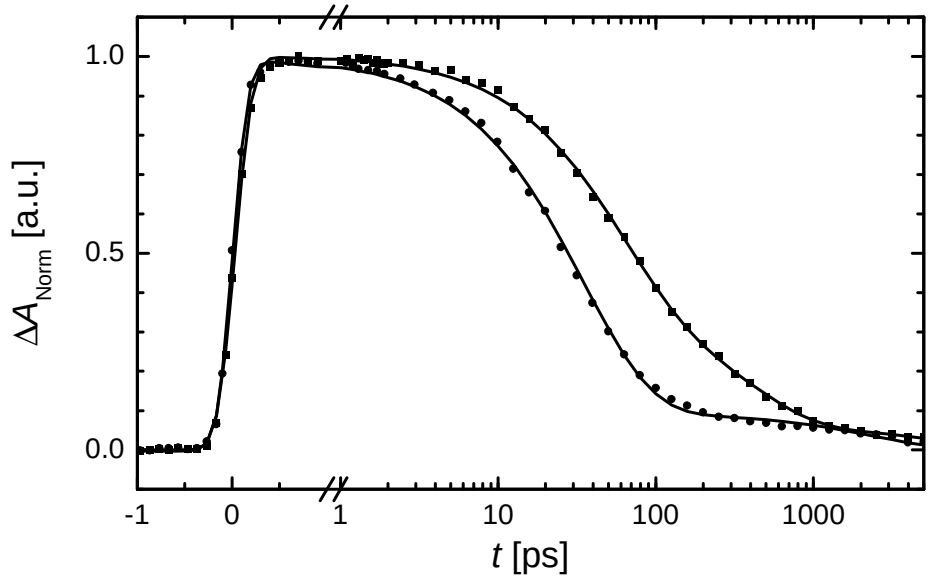

Fig. 4.10: Transient pump-probe kinetics measured in duplexes 3′-X^+G (•) and 5′-X^+G (■) using 455 nm pump pulses and 650 nm probe pulses. The different decay times, with main components of 35 ps for 3′-X^+G and 57 ps for 5′-X^+G, illustrate the directionality of hole transfer in X^+-modified duplexes. The solid lines are nonlinear least-squares fits to the kinetic data.

the excited state and the $X^\bullet$ state measured for duplexes with the same distance between the X^+ hole donor and an acceptor nucleobase are of the same order magnitude, with rate constants in the 3′-X^+ duplexes consistently larger than those in the 5′-X^+ duplexes (Table 4.2). This is illustrated in Fig. 4.10 for the duplexes 3′-X^+G and 5′-X^+G.

4.3 Discussion

The kinetic data of Section 4.2 are compiled in Table 4.1. The rate constants of the forward hole shift k_1 can be calculated according to Eq. (4.5).

$$k_1 = \frac{1}{\tau_{ES}} - \frac{1}{\tau_0} \tag{4.5}$$

In this equation, τ_0 is the excited-state lifetime of the reference duplex X^+(AT) (18 ns), and τ_{ES} the excited-state lifetime of a sample with hole transfer. The rate constants for the backward charge shift k_2 are obtained from the radical lifetimes and the ground-state recovery times. The rate constants k_1 and k_2 for all duplexes are summarized in Table 4.2.

Table 4.2: Forward and backward charge shift rate constants k_1 and k_2.

Duplex	k_1 [s^{-1}][a]	k_2 [s^{-1}][b]
3′-X^+G	2.6×10^{11}	2.9×10^{10}
5′-X^+G	1.7×10^{11}	2.0×10^{10}
3′-X^+AG	8.9×10^{7}	-
5′-X^+AG	2.8×10^{7}	-
3′-X^+Z	1.4×10^{12}	1.6×10^{11}
5′-X^+Z	1.1×10^{12}	1.3×10^{11}
3′-X^+AZ	9.1×10^{10}	1.0×10^{10}
5′-X^+AZ	8.3×10^{10}	5.9×10^{9}
3′-X^+AAZ	7.4×10^{7}	-
5′-X^+AAZ	3.0×10^{7}	-

[a] Forward hole shift rate constants calculated from excited-state lifetimes according to Eq. (4.5). [b] Rate constants for the backward charge shift obtained from the radical lifetimes and the ground-state recovery times.

As noted in the previous section, an important feature of all measurements is that both the charge shift rate and the back transfer rate are monoexponential and that there is only a small fraction of long-lived background signal observed in the transient kinetics. Monoexponential electron transfer rate constants point to well-defined electronic couplings in these duplexes. Since these couplings reflect short range interactions, one majority incorporation site for the X^+ chromophore is highly probable. The absence of distributed kinetics even on the subpicosecond time scale shows that structural fluctuations on any longer time scale are not reflected by a distribution of electronic couplings between X^+ and the nucleobases within the base stack. This invariance could be the result of strong π–π and dipolar interactions between the intercalated chromophore and the neighboring nucleobases, interactions which lead to an increased rigidity of the local structure around the intercalator and the X^+-specific features observed in the visible and near-UV CD spectrum of these duplexes. However, it is also possible that structural inhomogeneities are not reflected in the kinetics because variations of the electronic couplings are compensated by concomitant changes in the energetics.

Since very similar kinetics and transient absorption spectra are observed for hole transfer between X^+ and a hole acceptor at a fixed base pair separation in either helical direction of the duplex (Table 4.2), the following discussion is restricted to the phenomenology of 3′ duplexes. Moreover, preliminary information from a forthcoming NMR structure indicates that the base pairs in 3′ direction from the chromophore adopt a structure close to standard B-form, whereas a more pronounced perturbation is detected in

the other direction.[90] This finding is in accord with the observation that the long-lived background signal has larger amplitudes in 5′ duplexes pointing to a less ordered structure. The observation that in 3′ duplexes the electron transfer rate constants tend to be by a factor of two larger than in 3′ duplexes might therefore either stem from a less favorable geometry leading to a decrease in the electronic couplings between donor and acceptor and/or mirror the asymmetry of the electronic interaction between the nucleobases in the two helical directions.[73]

The femtosecond time-resolved absorption experiments presented in the preceding section provide detailed information on the phenomenology of hole injection dynamics in X^+-modified DNA duplexes. The excitation and probing conditions given for these duplexes allow independent access to the kinetics of $^1(X^+)^*$ decay and X^+ ground-state recovery, as well as the formation and decay times of the charge transfer product state $X^\bullet$. Before entering a more detailed discussion of these experiments, it should be stated that the crucial information on the nature of the steep distance dependence of hole injection rates for X^+-modified duplexes can be extracted directly from the data set in Table 4.2, without any assumptions or kinetic modeling. The kinetic features of the X^+–DNA duplexes clearly point to the interplay of two effects: the decrease in electronic couplings and a concomitant increase in the activation energy for hole transfer with increasing distance between X^+ and the electron donor species G or Z.

The following discussion of the mechanism and distance dependence of the hole transfer rate constants has to be kept on a qualitative level since too little is known about the basic electron transfer parameters in this specific DNA environment so far. Nevertheless, the following interpretation of the kinetics will be based on independent estimates of the low-frequency reorganization energy. Reorganization energies in DNA may be rather complex reflecting the response of the nucleobases, of the backbone, and the aqueous solvent on the change in charge distribution associated with the ET process. The most recent experimental value of λ_s arises from the work by Lewis et al., where data analysis in the framework of a semiclassical approach yields λ_s = 0.2–0.4 eV for the charge separation reaction in stilbene-capped DNA hairpins.[91] λ_s values in this range also follow from the recent analysis of reaction yields associated with hole hopping after thermal injection.[57, 58] In contrast, model calculations of λ_s in duplex DNA yielded much higher values for the solvent reorganization energy (3.0 eV at 15 Å) for both charge shift and charge separation processes.[46] These calculations were based on the explicit consideration of the dielectric heterogeneity of the surrounding medium also taking into account the fact that λ_s should be distance dependent.

4.3.1 Hole Transfer in 3′-X^+G and 3′-X^+Z

The forward hole transfer rate constants k_1 in the duplexes 3′-X^+G and 3′-X^+Z, where the hole donor and acceptor are in direct contact, are 2.6×10^{11} s^{-1} and 1.4×10^{12} s^{-1}, respectively and, as mentioned before, essentially single exponential. Small, long-lived background signals are attributed to a minority (<10%) of modified duplexes displaying an unfavorable geometry for hole transfer.

For any analysis of the kinetic data within the framework of ET theory an estimate of the driving force (Eq. 3.5) in the systems 3′-X^+G and 3′-X^+G is needed. However, there are no reliable data either for the oxidation potentials of the nucleobases or for the reduction potential of ACMA in a DNA environment. Because of the strong stacking interactions the in situ values may differ from those reported for solution by several tenths of an electronvolt.

In view of these uncertainties, the discussion at this stage will be based on the following estimate of the driving force. The ultrafast rate measured for 3′-X^+Z implies that hole transfer occurs under either activationless ($\Delta G = \lambda$), or slightly inverted conditions ($\Delta G > \lambda$). The above experimental estimates of λ[7] limit the driving force $-\Delta G$ to the range of 0.2–0.4 eV. Assuming the oxidation potential of G to be by about 0.1–0.3 eV higher than that of Z,[80, 92, 93] it follows that $-\Delta G \approx 0.0$–0.3 eV in 3′-X^+G**.** For both systems the respective back transfer rate constants k_2 are by a factor of 9 slower than the forward rate constants k_1. In contrast to k_1 the back transfer rate is characterized by a large driving force (<–2.3 eV) resulting from 2.7 eV excited-state energy of $^1(X^+)^*$ and the limits of ΔG for k_1. Such relatively small values for k_1/k_2 can, in principle, be explained applying the explicit formalism underlying Eq. (3.7).

How do the kinetic rate constants of X^+-modified DNA relate to other DNA charge transfer duplexes reported in the literature? In femtosecond absorption spectroscopy Lewis et al. have investigated synthetic DNA hairpins containing the neutral stilbene-4-4′-dicarboxamide as a photoexcited hole donor.[9, 66] In contrast to the charge shift reactions of the protonated acridine intercalator X^+ the stilbene derivative undergoes charge separation and recombination. In spite of the differences between X^+ and the stilbene derivative, the kinetic pattern in the nearest-neighbor hairpin ($k_1 = 1.0 \times 10^{12}$ s^{-1} and $k_2 = 4.3 \times 10^{10}$ s^{-1})[9] and in the 3′-X^+G duplex ($k_1 = 2.6 \times 10^{11}$ s^{-1} and $k_2 = 2.9 \times 10^{10}$ s^{-1}) can be compared qualitatively. The different ratios of the forward to back transfer rate constants, $k_1/k_2 \approx 23$ for the stilbene system and $k_1/k_2 \approx 9$ for 3′-X^+G can be attributed to the deeper inversion of

[7] The total reorganization energy in the classical limit λ is assumed to be dominated by the medium contribution λ_s.

k_2 in the case of the stilbene DNA hairpin. The replacement of G by Z in both the X^+–DNA and the stilbene–DNA system results in an acceleration of the hole transfer rate constants by a factor of 5. Consequently, at least in the case of nearest neighbor ET in duplex DNA, charge shift and charge separation reactions tend to show similar kinetic behavior.

4.3.2 Hole Transfer in 3′-X^+AG and 3′-X^+AAG

From the data in Table 4.2 it follows that the ratio of the forward rate constants k_1(3′-X^+G)/k_1(3′-X^+AG) is 2900. In the case of ignoring the mechanistic definition of β according to Eq. (3.10) and extracting its value from these two data points, where one of them applies to direct contact and the other one to superexchange-mediated transfer, the result would be an unphysically large β value of 2.3 $Å^{-1}$. This value is even higher than the 1.5 $Å^{-1}$ attenuation factor reported by Fukui et al.[22] and in more dramatic contrast to the previously reported β values of 0.6–0.8 $Å^{-1}$.[55, 60] Such a steep distance dependence is also supported by the observation of identical excited-state decay times in 3′-X^+AAG and X^+(AT), indicating that the hole transfer in 3′-X^+AAG must be much slower than the 18 ns excited-state lifetime of X^+ in X^+(AT). Already at this stage of the discussion a β value of the order of 2 $Å^{-1}$ indicates that in X^+-labeled DNA duplexes the electronic coupling V cannot be the sole factor determining the distance dependence of the injection rate. The large β value is rather the fingerprint of two superimposed effects: a decrease in the superexchange-mediated electronic coupling V which is accompanied by a growth of the activation energy with increasing X^+–G distance. This explanation is also consistent with the finding that in the system 3′-X^+AG the product state $X^\bullet$ is not observed. This is indicative of a fast (less activated) back transfer rate constant k_2 as compared to the forward rate constant k_1. In summary, in the X^+–DNA system there are two hole transfer regimes which differ with respect to the activation energy of the forward rate constant k_1: for the direct-contact system 3′-X^+G, and also for 3′-X^+Z and 3′-X^+AZ (see below) k_1 exceeds k_2, whereas the opposite is true for the duplexes 3′-X^+AG and 3′-X^+AAZ.

In order to put the concept of a distance-dependent activation energy in X^+-labeled duplexes to test, the injection reaction in the system 3′-X^+AZ should be faster than in 3′-X^+AG since replacing G by Z is expected to increase the driving force ΔG. This expectation is also supported by the nearest neighbor behavior as discussed in Section 4.3.1.

4.3.3 Hole Transfer in 3′-X^+AZ and 3′-X^+AAZ

In contrast to the large ratio k_1(3′-X^+G)/k_1(3′-X^+AG) = 2900, the replacement of G by Z leads to k_1(3′-X^+Z)/k_1(3′-X^+AZ) = 15. Together with the observation of the 3′-$X^{\bullet}AZ^{\bullet+}$ intermediate state this ratio indeed points to a smaller activation energy as compared to the one of the system 3′-X^+AG. The reduction factor of 15 per A:T base pair between a hole donor and acceptor in DNA is similar to that observed in the previous transient absorption experiments by Lewis et al.[9] and in the yield studies of Giese and coworkers.[61] In contrast to 3′-X^+AG, in 3′-X^+AZ the back transfer rate constant k_2 is observed, whereas the dynamics in duplex 3′-X^+AAZ are similar to those of 3′-X^+AG and k_2 is not observed. This phenomenology is to be expected from a change in the charge transfer mechanism from (nearly) activationless hole transfer in 3′-X^+AZ to thermally activated injection kinetics in 3′-X^+AAZ. Hence, these experiments involving nucleobase G/Z replacement independently justify the assignment of a large β value to a change in the mechanism involving the energy parameters.

In the duplex 3′-X^+AZ the ratio of rate constants is $k_1/k_2 = 10 \pm 2$. As in the direct–contact systems 3′-X^+G and 3′-X^+Z this ratio is expected to predominantly reflect forward hole transfer in the activationless or slightly activated regime of the Marcus expression, whereas the back transfer dynamics occur under inverted conditions. Since in contrast to the nearest neighbor systems, the hole transfer dynamics in 3′-X^+AZ are mediated by superexchange interaction due to the intervening A:T base pair, this ratio may also include a smaller superexchange coupling for k_2, as compared to k_1, caused by an increased vertical energy difference between the state 3′-$X^{\bullet}AZ^{\bullet+}$ and the A:T bridge.

4.3.4 Comparison to Previous Results

The duplexes 3′-X^+G, 5′-X^+G, 3′-X^+AG, and 5′-X^+AG are direct analogs of the DNA duplexes studied earlier by Fukui and Tanaka.[21, 22] In these studies, fluorescence quantum yields and fluorescence decay times were used to investigate the distance dependence of electron transfer in DNA between 9-amino-6-chloro-2-methoxyacridine (covalently attached to the DNA through a slightly different linker from that in X^+, see Section 4.1) and a guanine nucleobase. Most likely due to instrument limitation the forward charge shift rates in the X^+G duplexes have not been resolved. Importantly, the slow hole injection rates derived from time-resolved fluorescence measurements on 3′-X^+AG duplexes in the previous work are in agreement with the pump–probe measurements in this work. In addition, the dependence of k_1 on the helical direction of transfer, e.g. a comparison of

3′-X^+AG and 5′-X^+AG, is also reproduced by the transient absorption data, although the structural details of the binding site of the chromophore might differ due to the different attachment. The ratio k_1(3′-X^+G)/k_1(3′-X^+AG) from the measurements in this work is 2900, which predicts an apparent value of β in DNA of 2.3 $Å^{-1}$, a value even higher than the value given by Fukui and Tanaka of $\beta = 1.5$ $Å^{-1}$.[22] As stated in Section 4.3.2 this large attenuation factor is attributed to the superposition of a decrease in coupling and an increase in activation energy. This result is inaccessible by fluorescence measurements alone which cannot detect the change in the ratio k_1/k_2. In the more general context of relating fluorescence data to charge transfer dynamics and mechanisms, the discrepancy between the conclusions of Fukui et al. and the present work demonstrates the inherent danger of reliance on an experimental method which cannot follow the formation and decay of an intermediate product state, e.g. $X^{\bullet}G^{\bullet+}$.

4.3.5 Distance Dependence of the Activation Energy

According to the Marcus expression for the activation energy of an ET process, Eq. (3.3), two intrinsically different scenarios have to be envisaged concerning the mechanism by which distance-dependent activation energies may arise. On the one hand, the predominant distance-dependent effect may be a loss of driving force due to excited-state relaxation of $^1(X^+)^*$, as reported for ACMA in solution,[78] competing with ET. This relaxation has been related to an inferred change of dipole moment between the ground and excited state of 13 D and, in addition, to monopole-dipole interactions due to the protonation of the acridinium nitrogen. For a mixed solvent of high viscosity (90% glycerol, 10% aqueous buffer), a 100 ps relaxation mode was reported.[78] On the other hand, the medium reorganization energy in this charge shift reaction could display a distance dependence on purely electrostatic grounds (Eq. (3.4)).[24] In the following discussion, the viability of such a relaxation scenario in the X^+–DNA system will be put to test by estimating the kinetic and energetic parameters from a simple kinetic model.

In the absence of excited-state relaxation in the system 3′-X^+AG the forward rate constant k_1 is expected in the time window 50–100 ps when $\beta \approx 0.8$ $Å^{-1}$ is implied. In fact k_1 appears to be in the nanosecond range. With the assumption that $^1(X^+)^*$ relaxation occurs in this time window, the nanosecond rate constants for 3′-X^+AG reflect the superposition of two effects: (1) a decrease in the superexchange electronic coupling with increasing X^+–G distance, which slows down k_1 and thus allows (2) an X^{+*}-specific relaxation process to compete with charge injection after a specific donor–acceptor separation is reached. At larger X^+–G separation the relaxation rate is assumed to be faster than the charge transfer

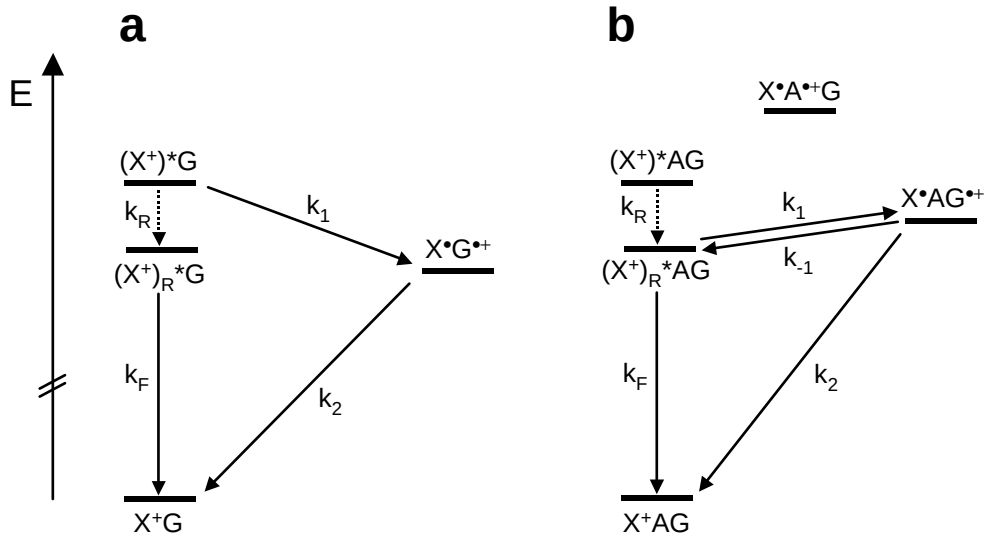

Fig. 4.11: Kinetic scheme for the distance-dependent change of mechanism in case a potential $^1(X^+)^*$ excited-state relaxation being the origin of the increase in the activation energy at larger distances. (a) Representing X^+G which is also a prototype for X^+Z and X^+AZ, whereas (b) is valid for the dynamics in X^+AG and X^+AAZ. $X^\bullet A^{\bullet+}G$ acts only as a superexchange mediator and is not an observable intermediate.

rate out of the initial Franck–Condon state. Since the relaxation process is expected to lower the driving force ΔG of charge injection, the latter becomes thermally activated. If relaxation influenced predominantly the electronic coupling V, the ratio k_1/k_2 would remain fairly constant and $X^\bullet$ should be observed in the transient absorption of 3′-X^+AG, in contrast to reality.

In Fig. 4.11 the dynamics of activationless or slightly activated and thermally activated electron transfer after X^+ excited-state relaxation are illustrated. If the steady-state approximation holds, the measured decay rate constant of $^1(X^+)_R{}^*$ in Fig. 4.11b is given by:

$$k_{\text{obs}} = k_{\text{F}} + \frac{k_2 k_1}{k_2 + k_{-1}} \tag{4.6}$$

In this equation k_F is the rate constant of fluorescence from the relaxed excited state $^1(X^+)_R{}^*$. In the following, ΔG denotes the difference in free energy between the states $^1(X^+)_R{}^*$ and $X^\bullet$ (Fig. 4.11b):

$$\frac{k_1}{k_{-1}} = \exp\left(-\frac{\Delta G}{k_{\text{B}} T}\right) \tag{4.7}$$

The validity of the steady-state approximation is supported by the monoexponentiality[8] and by the identical time constants observed for the X^+ excited-state decay and ground-state recovery in these duplexes. With the assumption that X^+ excited-state relaxation primarily affects k_1 and not k_2 (due to the insensitivity of k_{ET} to changes in the energetics in the inverted region) and taking an experimental value of 15 for the decrease in electronic coupling upon insertion of one A:T base pair,[9] then $k_2 \approx 1.9 \times 10^9\ s^{-1}$ in 3′-X^+AG and $k_2 \approx 6.7 \times 10^8\ s^{-1}$ in 3′-X^+AAZ. Due to the uncertainties involved, only the simplest case will be discussed, i.e., the relaxed system is assumed to be in the steady-state limit with $k_2 > k_{-1}$. In this case Eq. (4.6) can be rewritten as

$$k_{obs} = k_F + k_1 \tag{4.8}$$

where k_1 can be calculated according to Eq. (4.8). With the above expectation values of k_2 and using a value for the reorganization energy of $\lambda \approx 0.4$ eV (Section 4.3), an estimate for ΔG after relaxation can be obtained. Since $k_{obs} - k_F$ is $8.9 \times 10^7\ s^{-1}$ in 3′-X^+AG and $7.4 \times 10^7\ s^{-1}$ in 3′-X^+AAZ, after relaxation ΔG amounts to about +0.016 eV in the Z duplex and +0.053 eV in the G duplex. From these values the difference in the oxidation potentials between G and Z follows to be $\Delta E_{ox} = 0.037$ eV, which is a factor of 3 smaller than the estimated lower limit of 0.1 eV.[92] However, the tacit assumptions of invariant electronic couplings and reorganization energies in G and Z containing sequences and identical relaxation patterns might not be valid.

Importantly, the above estimates can explain the steep distance dependence of the rate constants only if the relaxation in the excited state is assumed to lead to a substantial energy loss (≥0.3 eV). Large energy losses in the excited state are difficult to reconcile with the steady-state absorption and fluorescence spectra (Fig. 4.3). Moreover, the monoexponential kinetics observed in the reference system X^+(AT) and also in the duplexes 3′-X^+AG and 3′-X^+AAZ in the wavelength region 450–750 nm do not support a relaxation process.

These results are in contrast to previous experiments on ACMA by Hélène and coworkers suggesting that in viscous media nuclear relaxation and electronic redistribution in the excited state may take place on the 100 ps time scale.[78] Moreover, a dynamic Stokes shift on this time scale has been reported for a coumarin dye incorporated into an oligonucleotide in place of a normal purine-pyrimidine base pair.[95] This shift occurs with components near 300 ps and 13 ns as measured with 100 ps time resolution. Since the

[8] In general, relaxation phenomena are complex processes leading to distributed kinetic behavior.[94] However, the kinetics observed in this work are almost monoexponential. Thus it has to be assumed that a potential relaxation occurs within a relatively narrow temporal window.

question of a potential energy loss due to excited-state relaxation is crucial for the interpretation of the results, a dedicated study has been performed and will be presented in the next chapter.

5 Excited-State Photophysics of ACMA Selectively Intercalated in Duplex DNA

In this chapter broadband femtosecond transient absorption spectroscopy in the wavelength region from 300–650 nm is employed to study quantitatively the excited-state relaxation in 9-amino-6-chloro-2-methoxyacridine-modified DNA duplexes. Upon excitation of the chromophore, changes in its charge distribution or polarizability may cause the local environment to reorganize. This reorganization would reduce the energy of the system and shift the fluorescence or stimulated emission spectrum of X^+ (the latter has been resolved in time in this work) to lower energies. The resulting energy losses would be maximal in the presence of dipolar or charged species, such as the hydrogen-bonds in the base pairs bases and the phosphate groups in the DNA backbone in the present X^+–DNA system. Since DNA is not per se a rigid structure, these experiments might also yield information about the time scale of structural fluctuations. The measurements were performed in the laboratories of N. P. Ernsting (Institut für Chemie, Humboldt-Universität zu Berlin) in collaboration with S. A. Kovalenko and J. L. Pérez Lustres.

The experimental results for the photophysics of X^+ in DNA will be compared to both the solution-phase behavior of the free chromophore 9-amino-6-chloro-2-methoxyacridine (ACMA) and its derivative quinacrine and to recent semiempirical calculations by A. A. Voityuk and N. Rösch (Institut für Physikalische und Theoretische Chemie, Technische Universität München).

5.1 Introduction

Strong and specific interactions of many natural and artificial compounds with DNA are crucial for their function as potent antitumor or antibiotic drugs.[96] Exogenous compounds binding to DNA by intercalation form an important class of such drug-DNA complexes. Good intercalators are usually heteroaromatic polycyclic systems which insert between two base pairs in a DNA duplex. ACMA derivatives are known to have the ability to intercalate efficiently into a DNA double helix.[97] This random intercalation into DNA results in

significant unwinding of the helix and a local increase in the base pair spacing. Binding of the intercalator within an abasic site in DNA, as discussed in Chapter 4, forms an alternative intercalation scenario that is advantageous since it implies a well-defined incorporation site and a non-random localization of the intercalator in the duplex.

Such transfer of a conjugated chromophore from aqueous solution to an intercalation site in the duplex often affects the photophysics of this species significantly, resulting for instance in a pronounced change of its fluorescence quantum yield.[98] For quinacrine at pH 7.0 a value of $\Phi = 0.74$ was reported in case of intercalation,[1] in contrast to $\Phi = 0.17$ for the chromophore in solution,[99] indicating that the environment inside the base stack of DNA is very different from that in aqueous solution. Indeed, the core of the duplex is normally considered as a medium of low dielectric constant.[100] Together with the deoxyribose–phosphate backbone the nucleobases protect the chromophore from collisional fluorescence quenching by oxygen.[101] Although the photophysics of intercalated chromophores is far from being understood, it has become an important tool in studies of DNA structure and dynamics, detection of DNA hybridization,[102] fluorescent imaging of DNA in gels, and fluorescent staining of chromosomal DNA.[103]

In this chapter the excited-state dynamics of protonated ACMA intercalated into a specific abasic site in a DNA duplex (Section 4.1) will be investigated with femtosecond broadband spectroscopy in order to clarify the entailed photophysics. The central questions are to which extent and on which time scale changes in the charge distribution cause a local reorganization of the environment.

5.2 Photophysics of ACMA in DNA

In order to rule out possible charge transfer deactivation pathways, the experiments were performed on the reference duplex X^+(AT) (for the sequence see Fig. 4.2). In this sequence complete exclusion of electron transfer from guanine to the X^+ excited singlet state is achieved by separating donor and acceptor by more than two A:T base pairs (Chapter 4). Under these conditions the excited-state lifetime of $^1(X^+)^*$ (18 ns) is too short to oxidize adenine in a thermally activated reaction.[104]

The ground-state absorption and steady-state fluorescence spectra of the X^+(AT) duplex at room temperature are shown in Fig. 5.1. All experiments presented in this chapter were performed at this temperature. In comparison to the spectra at 283 K (Fig. 4.3), increasing the temperature leads to a less pronounced vibronic fine structure, as can be seen in the

[1] This value refers to a duplex containing only A:T base pairs. The quantum yield of ACMA intercalated into an abasic site, as discussed in Chapter 4, was reported as $\Phi = 0.655$ at pH 7.2.[21]

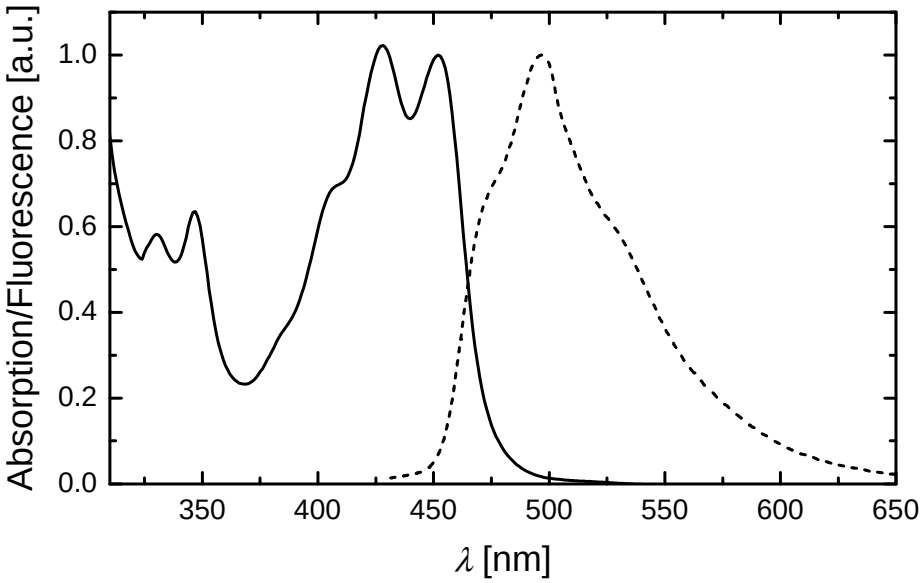

Fig. 5.1: Steady-state absorption (—) and fluorescence (---) spectra of X^+(AT) at 295 K. The absorption spectrum shows $S_1 \leftarrow S_0$ absorption bands at 452 and 428 nm and $S_2 \leftarrow S_0$ bands at 347 and 330 nm. The fluorescence emission has its maximum at 498 nm.

emission spectrum, e.g. in the decreased intensity of the side band at approximately 470 nm. This finding is in accord with previous measurements[22] and probably points to a less rigid chromophore binding site at higher temperatures. The peak positions of all bands in both the fluorescence and the absorption spectra remain unchanged.

Femtosecond transient absorption spectra were measured after excitation within the $S_1 \leftarrow S_0$ transition at 400 nm with 40 fs pulses and probed simultaneously in the 300–650 nm range with a supercontinuum. The optical setup of the laser system is described in Section 2.1.8. Figure 5.2 shows the transient absorption spectra obtained directly after excitation and in a final quasi-stationary state. Importantly, there are only very minor changes in the spectrum with time at all probe wavelengths. The analysis of 10 measurements yielded time constants ranging from 25 ps to 100 ps and a spectral change after 60 ps which is similar to the one shown in Fig. 5.2: a small decrease in ΔA in the ultraviolet and red, and no change or a small increase in the bleached band at 450 nm. The variation of the time constants may simply reflect the fact that the evolution is close to the detection limit. Therefore, the apparent change could also be due to a systematic error, such as loss of spatial overlap between pump and probe, which was optimized at small delays. In comparison with the steady-state absorption and emission spectra and together with the monoexponential kinetics for selected probe wavelengths discussed in the previous chapter, the result of negligible spectral change is readily extended into the nanosecond range.

The spectra can be understood qualitatively in comparison with the steady-state spectra

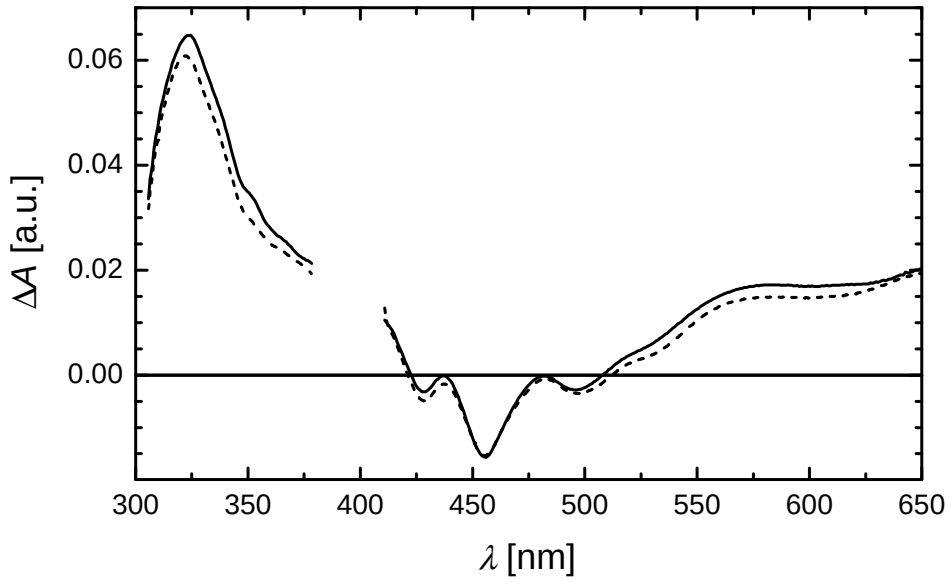

Fig. 5.2: Transient absorption spectra of the duplex X^+(AT) at 295 K obtained with 40 fs excitation at 400 nm after 220 fs (—) and 60 ps (---).

shown in Fig. 5.1. Positive ΔA signifies excited-state absorption. It appears prominently at 320 nm but also at wavelengths >510 nm and increases to the red edge of the observation window. Negative difference absorption (ΔA) around 455 nm and 425 nm is recognized as bleached $S_1 \leftarrow S_0$ ground-state absorption whereas negative ΔA near 500 nm indicates stimulated emission at the peak of the fluorescence band. The shoulder at 530 nm is also seen in stimulated emission.[2]

At this stage an important observation can be made regarding the femtosecond transient spectra of the X^+ chromophore intercalated in DNA: There is no evidence of a spectral shift of the stimulated emission band. Rather, the stimulated emission band attains its fixed spectral position within 220 fs, as given by the time resolution of the experiment. This is in contrast to the behavior reported for free ACMA and quinacrine in low-viscosity aqueous solution which will be discussed in the next section.

5.3 Comparison to the Solution Phase

ACMA and quinacrine, differing from ACMA only by the aliphatic chain extending from the 9-position of the middle ring (Fig. 5.3), were reported to display similar steady-state

[2] Note that the fluorescence quantum distribution over the wavelength λ, as in Fig. 5.1, must be scaled with λ^4 to obtain the corresponding cross section for stimulated emission which enters Fig. 5.2.

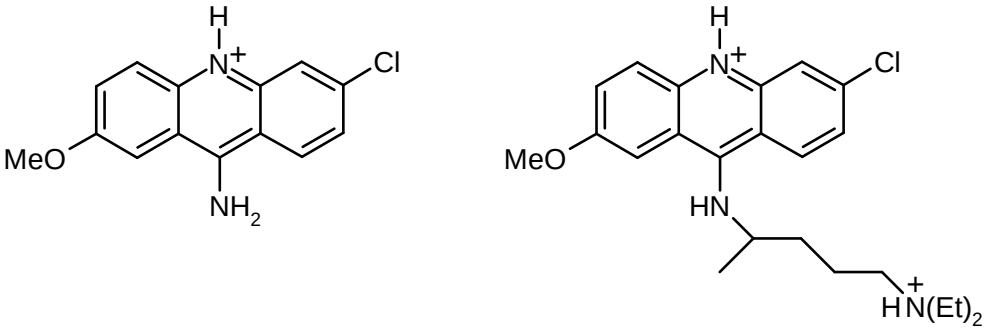

Fig. 5.3: Chemical structures of ACMA (left) and quinacrine (right) in their prototropic forms prevailing at pH 7.

spectroscopic properties.[105] The steady-state spectra of quinacrine in its prototropic form prevailing at pH ~7 are shown in Fig. 5.4.[3] The absorption spectrum is characterized by a broad band centered at 424 nm with vibronic bands at 443 and ~400 nm, which previously have been assigned to the $S_1 \leftarrow S_0$ electronic transition.[82] The extinction coefficient has been determined to be ~10 000 M^{-1} cm^{-1} at 424 nm.[89] The emission spectrum is broad and structureless with a peak around 510 nm.

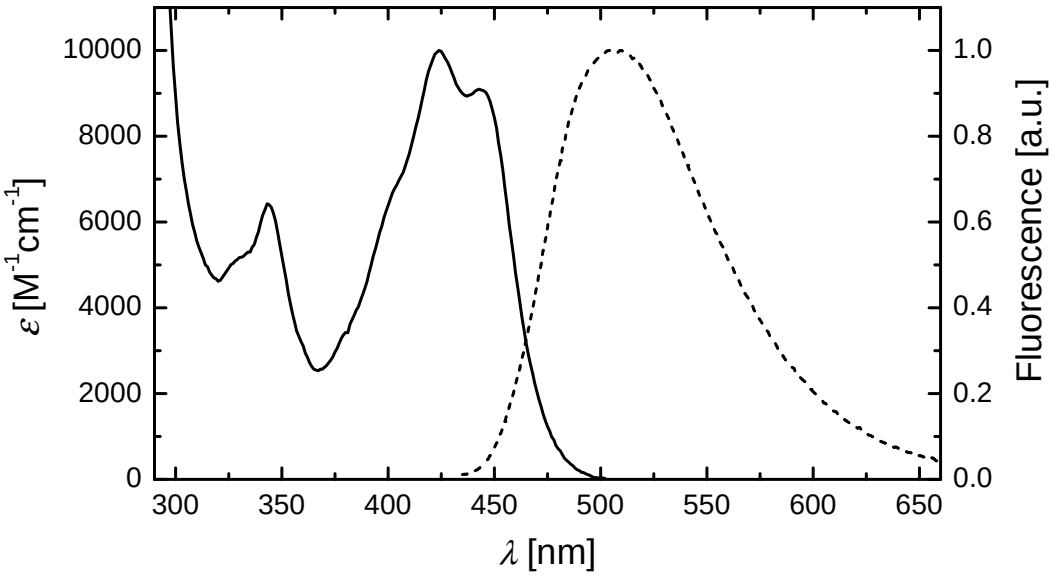

Fig. 5.4: Steady-state absorption (—) and fluorescence (---) spectra of quinacrine at 295 K, pH 6.88. The absorption spectrum shows $S_1 \leftarrow S_0$ absorption bands at 424 and 443 nm. The fluorescence spectrum has its maximum at about 510 nm.

[3] The pK_a values for the deprotonation of the acridinium nitrogen have been reported as 8.6 and 8.3 for ACMA and quinacrine, respectively.[78, 105]

Despite the wide use of quinacrine and ACMA as fluorescence labels in various applications their excited-state dynamics in aqueous solution are not well understood. Both molecules are known to display a complex fluorescence emission behavior.[77-79] For ACMA a time-dependent Stokes shift on the 1–4 ns time scale has been reported by several groups and different interpretations have been suggested.[78, 79] Sun et al. have interpreted their experiments in terms of an unusually slow solvent relaxation around the excited state of the chromophore,[78] whereas Fan et al. have discussed similar results within the framework of an excited-state cis-trans isomerization involving the chromophore's methoxy group.[79] The slow solvent relaxation has been related to a large change of dipole moment between the ground and excited state of 13 D and, in addition, to monopole-dipole interactions due to the protonation of the acridinium nitrogen. As mentioned before (Section 4.3.5), for a mixed solvent of high viscosity (90% glycerol, 10% aqueous buffer), a 100 ps relaxation mode was reported.[78] The concept of cis-trans isomerization was backed up by quantum chemical calculations on ACMA under isolated conditions (gas phase)[106] using the semiempirical AM1 method. In the electronic ground state the protonated ACMA was predicted to be most stable in a planar geometry. Due to a small barrier to rotation a rapid equilibration of the cis-isomer (with the methyl moiety of the methoxy group oriented toward the amino group, see Fig. 5.5) and the trans isomer was expected. However, for the S_1 state a relatively large barrier of 5.4 kcal mol^{-1} resulted from these calculations, thus supporting cis-trans isomerization of the methoxy group as the most plausible mechanism and as the explanation of the complex pattern of the fluorescence decay of ACMA in aqueous solution.

Such quantum chemical calculations have been extended in two ways: (1) The optimization was carried out without any constraints, and (2) for both isomers the effect of a polar environment (water) was taken into account in the calculations of the energies and spectroscopic characteristics.[107] According to these calculations, in aqueous solution the

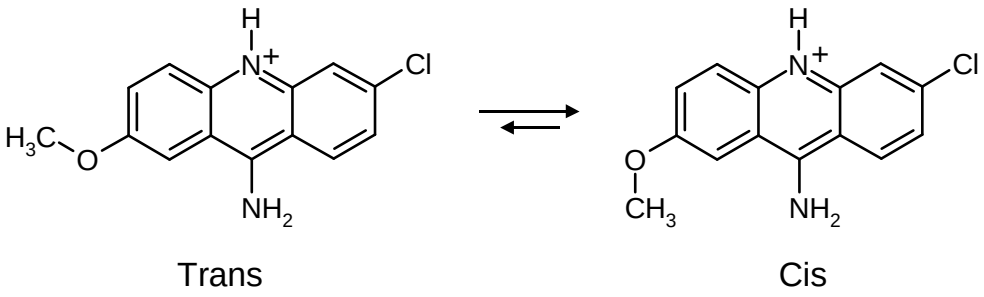

Fig. 5.5: Cis and trans conformations of the methoxy group of ACMA. The cis-isomer is more stable than the trans-isomer in the ground and the first excited state.

Table 5.1: AM1 calculated spectroscopic properties of ACMA in water. $h\nu$, λ, and f denote the energy, wavelength, and oscillator strength of the vertical excitations. Also given is the change of the dipole moment between the ground and excited state, $\Delta\mu$, for each transition.

Isomer	$h\nu$ [eV]	λ [nm]	f	Transition	$\Delta\mu$ [D]
Cis	3.105	399	0.06	HOMO → LUMO+1	2.60
	3.162	392	0.23	HOMO → LUMO	3.68
Trans	3.104	399	0.07	HOMO → LUMO+1	2.73
	3.138	395	0.23	HOMO → LUMO	4.14

free energies of the trans- and the cis-isomers of ACMA in their monoprotonated form are quite similar. The cis-isomer is more stable than the trans-isomer in the ground and the first excited state: The difference in energy is found to be 0.3 kcal mol^{-1} for the electronic ground state and 1.5 kcal mol^{-1} for the excited S_1 state. Additional B3LYP/6–31G* calculations of the cis and trans compounds with full geometry optimization also yield essentially isoenergetic conformers in the ground state (the difference is 0.05 kcal mol^{-1}). As stated previously,[106] the barrier to rotation of the methoxy group changes considerably upon electronic excitation. In aqueous solution the activation energy for cis-trans isomerization of ACMA in water is 1.0 kcal mol^{-1} and 6.6 kcal mol^{-1} for the S_0 and S_1 states, respectively. The calculated spectroscopic properties of ACMA are compiled in Table 5.1.

A calculation of vertical, or Franck-Condon, excitations predicts two closely lying transitions at 392–395 nm and 399 nm. The energies of these transitions are in agreement with the experimental spectrum which exhibits an intensive absorption band in the region 380–430 nm peaking at ~408 nm.[78] The adiabatic (vibrationally and configurationally relaxed) excitation energies in water are calculated at 446 nm and 438 nm (2.78 eV and 2.83 eV for the cis and trans forms, respectively). Therefore, the corresponding reorganization energies of the ACMA excited singlet state are 0.33 eV and 0.27 eV, resulting in a Stokes shift for the system of about 0.6 eV. In aqueous solution at pH 6 a Stokes shift, as determined from the absorption and emission maxima, of about 0.55 eV has been reported.[78] For quinacrine the spectra shown in Fig. 5.4 yield a value of 0.5 eV. The larger part of that shift is attributed to the reorientation of the polar solvent molecules triggered by the change of charge distribution upon excitation of ACMA. The calculations show that this change of the dipole moment by vertical excitation amounts to only 3–4 D in contrast to the previously inferred value of 13 D.[78]

Due to the red shift of the absorption spectrum and the blue shift of the emission spectrum upon intercalation (Figs. 5.1 and 5.4) the Stokes shift between the absorption and fluorescence maxima of ~0.4 eV for X^+ in X^+(AT) is smaller than the one observed for ACMA and quinacrine in aqueous solution. This shift is already developed within 200 fs (Fig. 5.2) implying that the repolarization of the nuclear degrees of freedom of the DNA pocket is ultrafast. As shown in detail for coumarin 153 in polar and non-polar environments,[108, 109] the Stokes shift, and thus the reorganization energies in all solvents are dominated by interactions between the different charge distribution of the solute and the permanent charge distributions of the solvent molecules. The only distinction between the strongly polar and non-polar solvents (and eventually media like rigid hydrogen-bonded nucleobases forming π–π-stacks with the chromophore in DNA) is that in the former case the electrostatics mainly involves solvent dipole-solute dipole interactions, whereas in non-polar solvents the interactions are with quadrupole and higher-order multipole moments of the solvent. Maroncelli et al. have shown that these interactions are by no means negligible compared to dipole-dipole interactions.[109]

5.4 Conclusions

In the present system of X^+ intercalated into DNA both π–π-interactions between X^+ and the adjacent nucleobases, as well as polar interactions exerted for instance by the hydrogen bonds of these base pairs, may contribute to environmental reorganization induced by the dipole moment change of 3–4 D. The maximal Stokes shift of 0.4 eV is smaller than the one observed in aqueous solution. In contrast to aqueous solution, where the Stokes shift still develops on the nanosecond time scale, in the duplex it reaches a constant value within 200 fs and persists up to the lifetime of about 20 ns of the X^+ excited state. These results indicate that the replacement of a thymidine phosphate unit by X^+ in DNA leads to a structure which is fundamentally different from an aqueous environment. The invariance of the entire difference absorption spectrum at times longer than 200 fs allows to rule out excited-state deprotonation since this process would imply significant changes in the band structure of the absorption spectrum.[105] Additionally, the ultrashort time scale of the relaxation process allows one to dismiss the role of thermal fluctuations of the DNA structure in the excited-state dynamics of $^1(X^+)^*$.

Nevertheless, the constancy of the Stokes shift within the time window from 200 fs to >5 ns is extremely relevant to the interpretation of the distance dependence of the activation energies for hole injection that was postulated in Chapter 4. Since a loss of energy expressed in a red shift of the stimulated emission spectrum is not observed on this

time scale, a relaxation in the excited state competing with ET can be ruled out as the origin of the observed experimental behavior. Moreover, the results also indicate that hole injection from X^+ to G or Z in the direct contact systems already occurs from the totally relaxed excited state (Section 4.3.1), thus rendering all measurements comparable in terms of the excited-state energetics.

In the Chapter 6, the change of activation energy with increasing donor–acceptor separation will be quantified and related to the medium reorganization energy.

6 Distance-Dependent Activation Energies for Hole Injection into Duplex DNA

The results on the apparently anomalous attenuation factor for photoinduced hole injection into DNA duplexes modified by protonated 9-amino-6-chloro-2-methoxyacridine, as presented in Chapter 4, led to the conclusion that in addition to the electronic couplings the activation energy must also be distance dependent. In this chapter, this postulate will be verified by direct measurements of the activation energies for a series of X^+-modified DNA duplexes which sample an appreciable range of donor–acceptor distances (~4–10 Å). It will be shown that the resulting changes in the thermal activation energy can be explained self-consistently within the framework of a distance-dependent reorganization energy. The full sequences of all strands considered in this chapter are shown in Fig. 4.2.

6.1 Preparations for the Measurements

6.1.1 Accessible Temperature Range

Transient absorption measurements on the modified DNA duplexes in aqueous solution can only be performed in a very limited temperature range. A lower limit is imposed by the freezing point of the aqueous solution whereas the upper limit is given by the melting point of the DNA double strands. In order to avoid any effects related to partial unwinding of the double helix, measurements were only performed at temperatures at least 20 K below the melting points. Preliminary temperature-dependent experiments showed that the resulting temperature window (273–305 K) was too small to obtain reproducible results for the activation energies.

To increase the accessible temperature range sucrose was added to the buffer solutions as freezing point depression agent. Sucrose is a common cryoprotectant for proteins and has also been used for nucleic acids.[110] The buffer/sucrose solutions prepared as described in Section 2.3.1 had freezing points of ~245 K. Moreover, the addition of sucrose was found to increase the melting point of the duplex $3'$-X^+G_{13} by more than 6 °C. The temperature range studied was 245–305 K.

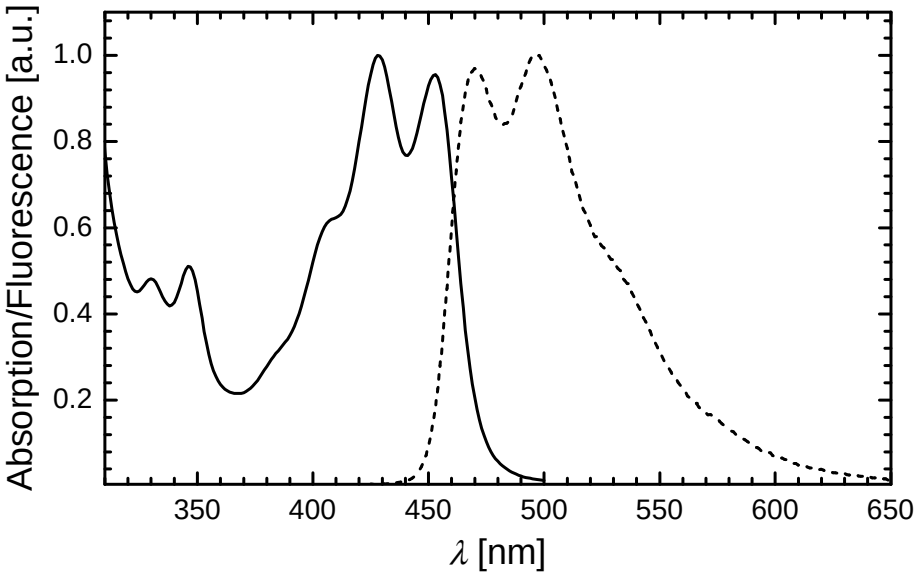

Fig. 6.1: Normalized absorption (—) and fluorescence emission (---) spectra of X^+ in duplex X^+(AT) at 283 K in buffer/sucrose solution.

6.1.2 Characterization of the Samples in Buffer/Sucrose Solution

The absorption and fluorescence spectra of the duplex X^+(AT) in buffer/sucrose solution at 283 K are shown in Fig. 6.1. The peak positions of both the absorption and the fluorescence bands remain almost unchanged ($\Delta\lambda \leq 2$ nm), as compared to the spectrum in pure buffer (Fig. 4.3). Especially in the emission spectrum, but also to a smaller extent in the absorption spectrum, addition of sucrose leads to a more pronounced vibronic structure and a narrowing of the bands, as expected from a more viscous medium.

For proteins it is known that a change of external conditions (e.g. cryoprotector addition) can induce structural perturbations. In time-resolved measurements multiple binding sites will be reflected by dispersive kinetics. In the X^+–DNA system, these changes are likely to be quite minor as indicated by the following observations: The near-invariance of the CD spectra and only minor changes of the rate constants at 283 K upon addition of sucrose (Tables 4.2 and 6.1) indicate that the intercalation geometry of X^+ and the overall B-form of the duplex are maintained. Additionally, temperature-dependent structural effects on the coupling are also expected to be small, as indicated by the monoexponentiality of the injection rates, the linearity of the Arrhenius plots, and the invariance of the CD spectra down to 263 K (Fig. 6.2). However, it should be noted that in some samples the addition of sucrose led to a slight increase in the amplitude of the long-lived background signal. This signal is ascribed to a minority (<15%) of modified duplexes displaying an unfavorable geometry for hole transfer. A comparison of experiments performed in buffer/sucrose solution with preliminary measurements in pure buffer in the

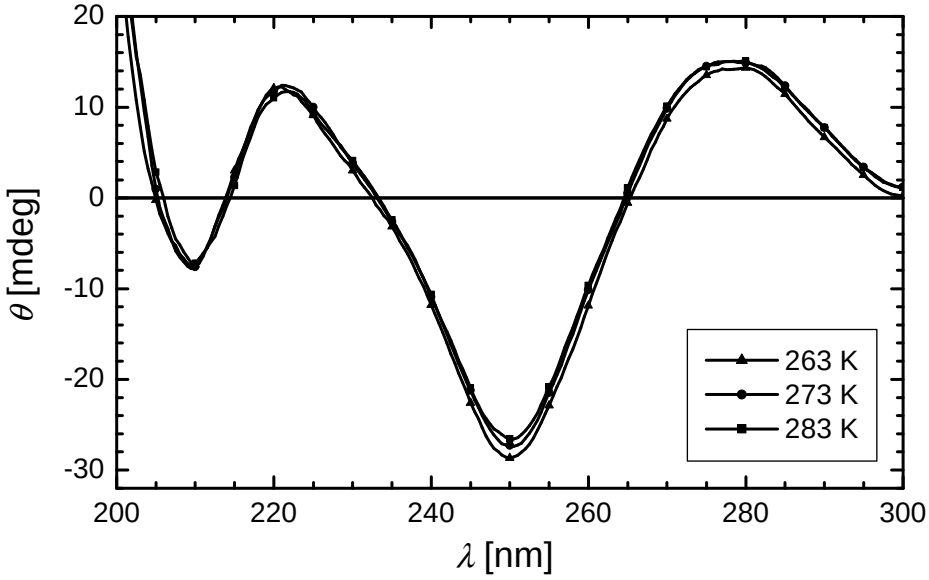

Fig. 6.2: Temperature dependence of the CD spectra of the duplex 3′-X^+AAZ in buffer/sucrose solution.

temperature range 275–305 K indicates that the activation energies do not change within the experimental error bars upon addition of sucrose.[1] Finally, as will be shown in the following sections, the experimental activation energies explain the large changes in the observed rates (Chapter 4) in a self-consistent way.

6.2 Temperature-Dependent Measurements

The temperature dependence of the hole transfer kinetics in the G and Z containing duplexes 3′-X^+G, 3′-X^+Z, 3′-X^+AG, 3′-X^+AZ, and 3′-X^+AAZ was studied with time-resolved absorption spectroscopy. The transient features that can be observed after photoexcitation of the chromophore were discussed in detail in Chapter 4. For the duplexes 3′-X^+G, 3′-X^+Z, and 3′-X^+AZ, the formation and decay of the $X^\bullet$ intermediate could be monitored in the 500–530 wavelength range. For these samples the singlet state $^1(X^+)^*$ and the radical state $X^\bullet$ absorb at 650 nm. The kinetics at longer times are dominated by the decay of the radical. However, for 3′-X^+AG and 3′-X^+AAZ, the kinetics at 650 nm reflect the decay of the excited singlet state. The temperature-dependent measurements are shown in Figs. 6.3–6.6.

[1] For example, the activation energy for the backward charge shift process in 3′-X^+G was determined to be $E_a = 0.13 \pm 0.03$ eV in buffer and $E_a = 0.14 \pm 0.02$ eV after adding sucrose.

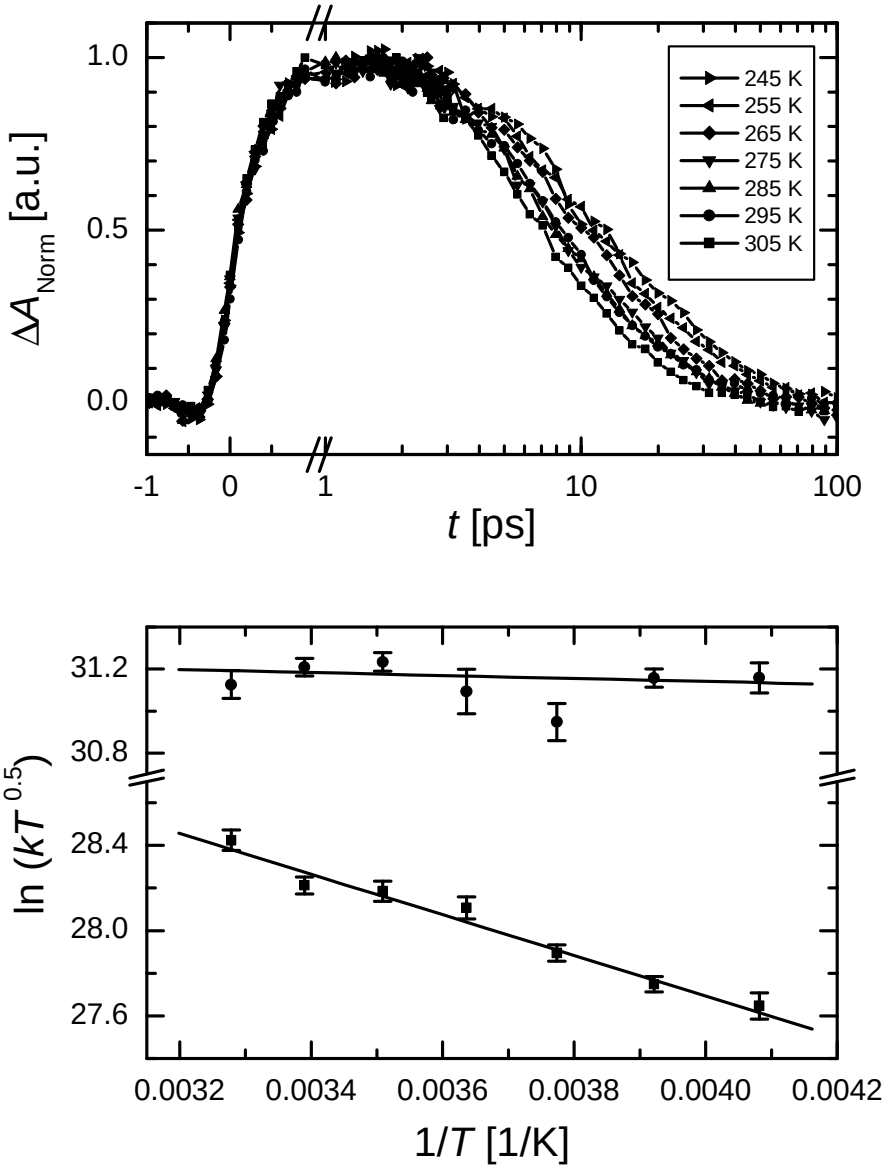

Fig. 6.3: Temperature dependence of hole transfer in the duplex 3′-X^+Z. Transient pump-probe kinetics measured using 455 nm pump and 500 nm probe pulses (top). Arrhenius plots (according to Eq. (6.1)) for the forward (●) and backward (■) hole transfer rate constants (bottom).

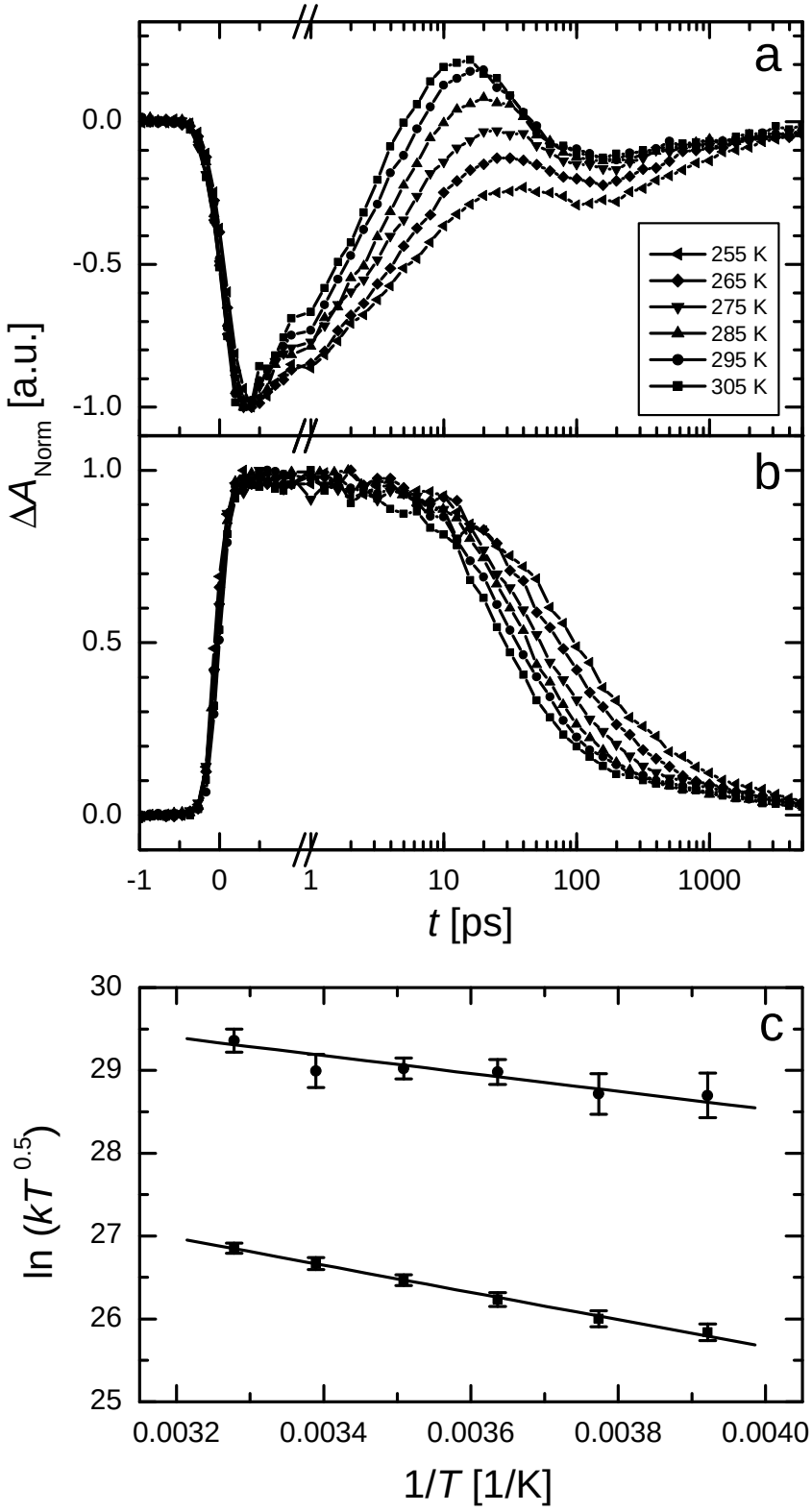

Fig. 6.4: Temperature dependence of hole transfer in the duplex 3′-X^+G. Transient pump-probe kinetics measured using 455 nm pump and either 500 nm (a) or 650 nm (b) probe pulses. (c) Arrhenius plots for the forward (●) and backward (■) hole transfer rate constants.

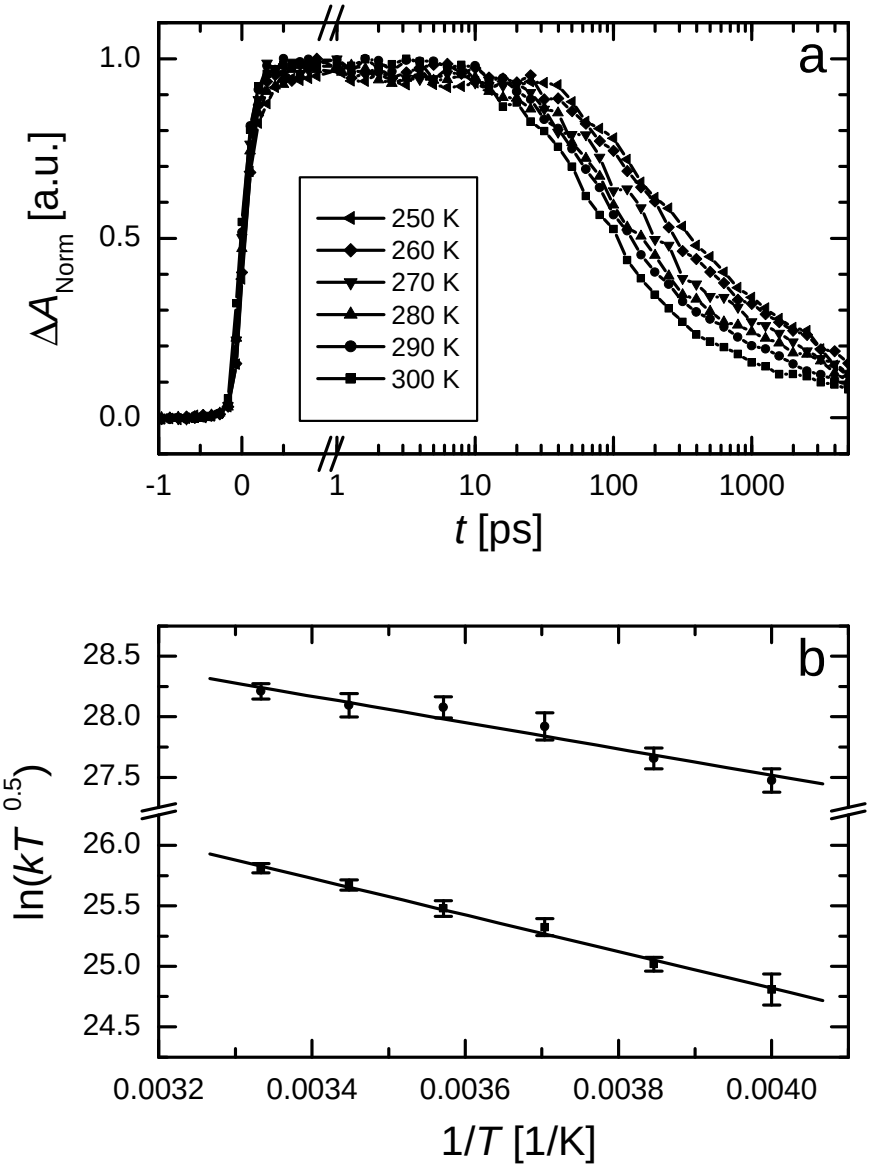

Fig. 6.5: Temperature dependence of hole transfer in the duplex 3′-X^+AZ. (a) Transient pump-probe kinetics measured using 455 nm pump and 650 nm probe pulses. (b) Arrhenius plots (according to Eq. (6.1)) for the forward (●) and backward (■) hole transfer rate constants.

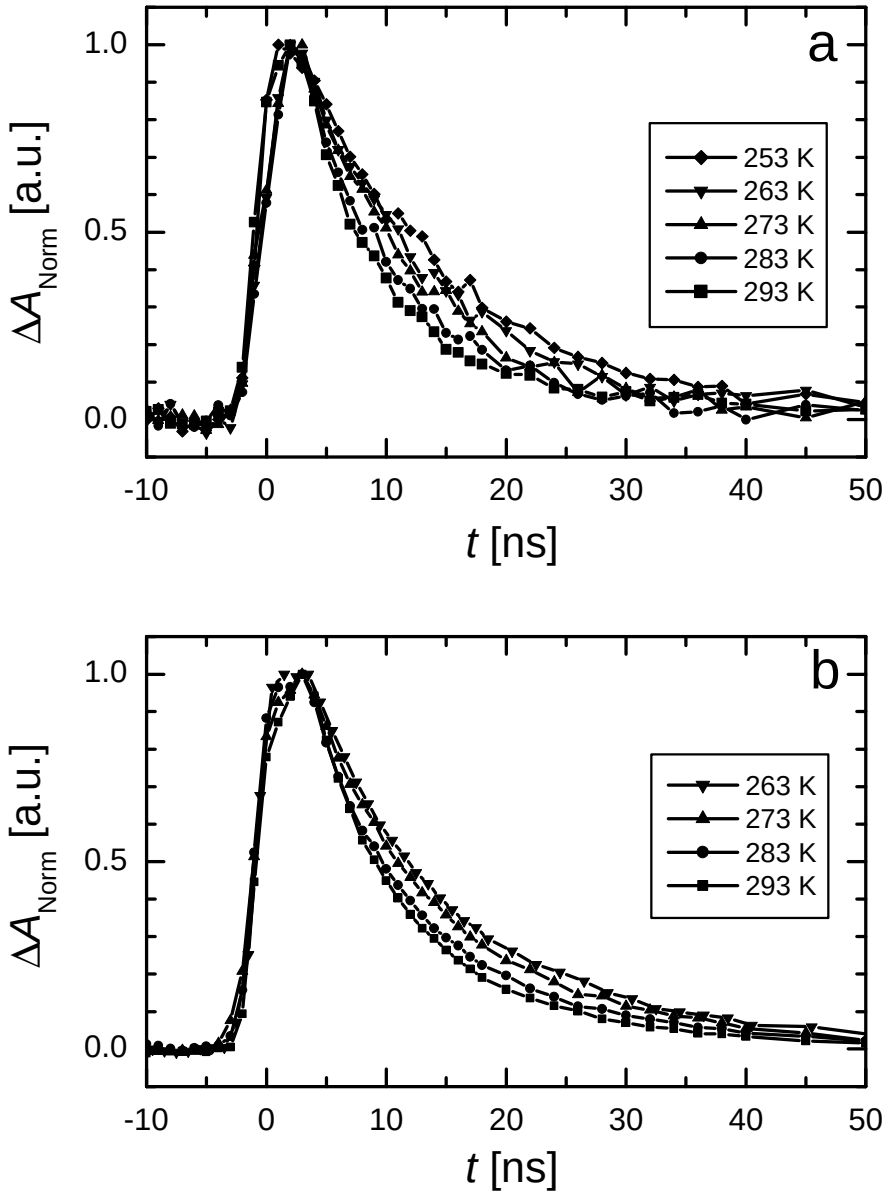

Fig. 6.6: Temperature dependence of hole transfer in the duplexes 3′-X^+AG (a) and 3′-X^+AAZ (b). Transient pump-probe kinetics measured using 450 nm pump and 660 nm probe pulses. The Arrhenius plot for (b) is shown in Fig. 6.7.

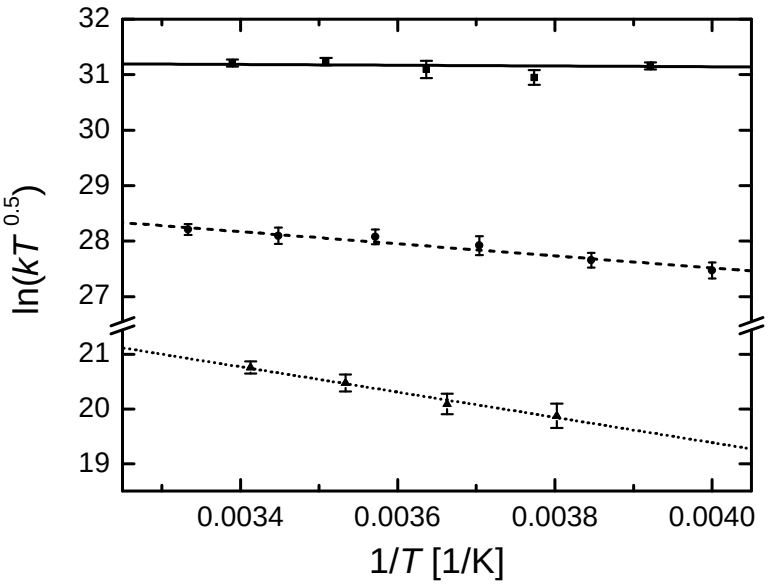

Fig. 6.7: Effect of temperature on the rate constants for the forward hole transfer in 3′-X^+Z (■), 3′-X^+AZ (●), and 3′-X^+AAZ (▲). Each successive insertion of an A:T pair between X^+ and Z leads to an increase in the activation energy of about 0.1 eV.

In the absence of hole injection, duplex X^+(AT), the X^+ excited-state lifetime of 18 ns is observed to be independent of temperature over the range studied.

According to Eqs. (3.2) and (3.3), the temperature dependence of the ET rate constant can be described by:

$$k_{\mathrm{ET}}\sqrt{T} = A\exp\left[-\frac{E_a}{k_{\mathrm{B}}T}\right] \tag{6.1}$$

It follows from Eq. (6.1) that a plot of $\ln(k_{\mathrm{ET}}T^{0.5})$ versus $1/T$ should yield a straight line with the slope being proportional to the activation energy. As can be seen from Figs. 6.3–6.6, the experimental data are indeed well described by linear Arrhenius plots and there is no indication of processes leading to a more complicated behavior. For example, a temperature dependence of the electron transfer kinetics that does not simply follow Eq. (6.1) has been reported for donor–bridge–acceptor molecules with a tetracene donor and a pyromellitimide acceptor.[111] The observed complicated behavior has been related to torsional motions of the phenylenevinylene bridge molecules which seem to gate the ET process. Based upon the linearity of the plots in the present system, temperature-dependent effects on the coupling, as caused by structural changes, are expected to be small over the investigated temperature range. The activation energies are summarized in Table 6.1.

Table 6.1: Forward and backward hole transfer rate constants k_1 and k_2 at 283 K and the corresponding activation energies E_a. Also listed is the preexponential factor A for the forward hole transfer.

Duplex	k_1 [s^{-1}] [a]	E_a [eV] [b]	A [s^{-1} $K^{0.5}$]	k_2 [s^{-1}] [c]	E_a [eV] [b]
3′-X^+G	2.0×10^{11}	0.08 ± 0.04	9.1×10^{13}	1.9×10^{10}	0.14 ± 0.02
3′-X^+AG	6.5×10^{7}	0.20 ± 0.04	4.0×10^{12}	-	-
3′-X^+Z	2.0×10^{12}	<0.015	$<6.2 \times 10^{13}$	1.0×10^{11}	0.08 ± 0.01
3′-X^+AZ	9.3×10^{10}	0.09 ± 0.01	6.3×10^{13}	6.9×10^{9}	0.13 ± 0.02
3′-X^+AAZ	4.6×10^{7}	0.20 ± 0.02	2.8×10^{12}	-	-

[a] Forward hole shift rate constants calculated from excited-state lifetimes according to Eq. (4.5). [b] Error bars of the activation energies are estimated from the Arrhenius plots (based on the error bars of the individual time constants) and by repetition of identical measurements. [c] Rate constants for the backward charge shift obtained from radical lifetimes.

As can be seen from Table 6.1, each successive insertion of an A:T pair between X^+ and G or Z leads to an increase in the activation energy for forward charge shift of about 0.1 eV (Fig. 6.7). In contrast, the activation energies for backward charge shift seem to show a weaker distance dependence which explains why for 3′-X^+AG and 3′-X^+AAZ only the forward charge shift can be observed (Chapter 4). Thus it can be concluded that the anomalously steep distance dependence of hole injection rate constants in X^+–DNA duplexes carrying zero, one, or two A:T pairs between X^+ and G or Z is dominated by distance-dependent activation energies.

6.3 Discussion

6.3.1 Analysis of the Activation Energies and Rate Constants

With Eq. (6.1) the relative contributions of the activation term and the preexponential factor to the observed rate constants can be estimated. The preexponential factor A mainly reflects the electronic couplings, with a weak contribution from the reorganization energy:

$$A \propto \frac{V^2}{\sqrt{\lambda}} \tag{6.2}$$

Using the values for E_a and k_1 from Table 6.1, it will be investigated whether the experimental activation energies can explain the large difference in rate constants for the

pairs 3′-X^+AG/3′-X^+AZ and 3′-X^+AZ/3′-X^+AAZ. The preexponential factors for the injection step are also listed in Table 6.1.

For the pair 3′-X^+AZ and 3′-X^+AAZ, the ratio of the rate constants for forward hole transfer is about 2000. From Table 6.1 it follows that hole transfer slows down by a factor of about 90 due to activation and only by a factor of 20–25 due to the decrease in electronic couplings (with the contribution of the reorganization energy estimated on the basis of the results presented in the next section). The purely electronic reduction factor is consistent with the range of 10–30 reported for other DNA-based donor–acceptor systems.[55, 60] The large difference in the rate constants between 3′-X^+AZ and 3′-X^+AG can be explained in an analogous way. Here, the difference in activation energies accounts for a factor of $\exp(\Delta E_a/k_B T) \approx 90$. The ratio of A(3′-X^+AZ)/A(3′-X^+AG) ≈ 15 may imply different couplings of G and Z. However, it should be explicitly stated that due to the uncertainties involved in estimating the preexponential factors the above values have to be considered as crude estimates. Finally, it follows from Table 6.1 that A(3′-X^+Z)/A(3′-X^+AZ) ≈ 1. The direct contact case (3′-X^+Z) cannot be expected to follow Eq. (3.10) since the exponential decay of the electronic couplings is valid only for superexchange-mediated ET processes. Often this is not taken into account in the interpretation of kinetic data from donor–bridge–acceptor systems.

In conclusion, independent of the energetic parameters involved the activation energy can explain the observed large changes in rate constants in a self-consistent way.

6.3.2 Distance Dependence of the Reorganization Energy

The following analysis will be restricted to the activated hole injection reactions for which the classical Marcus expression (Eq. (3.3)), which relates E_a to the thermodynamic driving force ΔG and the reorganization energy λ, can be employed. Equation (3.3) is a useful starting point since quantum effects are expected to be small in the normal region ($-\Delta G < \lambda$) near room temperature.[2] This behavior is in contrast to the back transfer reactions which occur under strongly exergonic conditions ($-\Delta G > \lambda$) in the inverted regime. For these latter reactions a quantum mechanical treatment of the vibrational degrees of freedom is essential.

[2] Entropy contributions to ΔG and λ are assumed to be negligible. Both ΔG and λ are free energy parameters and therefore temperature dependent. Recently, the absolute values of the temperature derivatives ($\delta\lambda_s/\delta T$) and ($\delta\Delta G/\delta T$) for an intramolecular ET reaction were estimated to be about 0.001 eV/K,[112] implying a potential change of up to ~0.05 eV over the temperature range studied. In view of the uncertainties of ΔG and E_a in the present system these effects will be neglected.

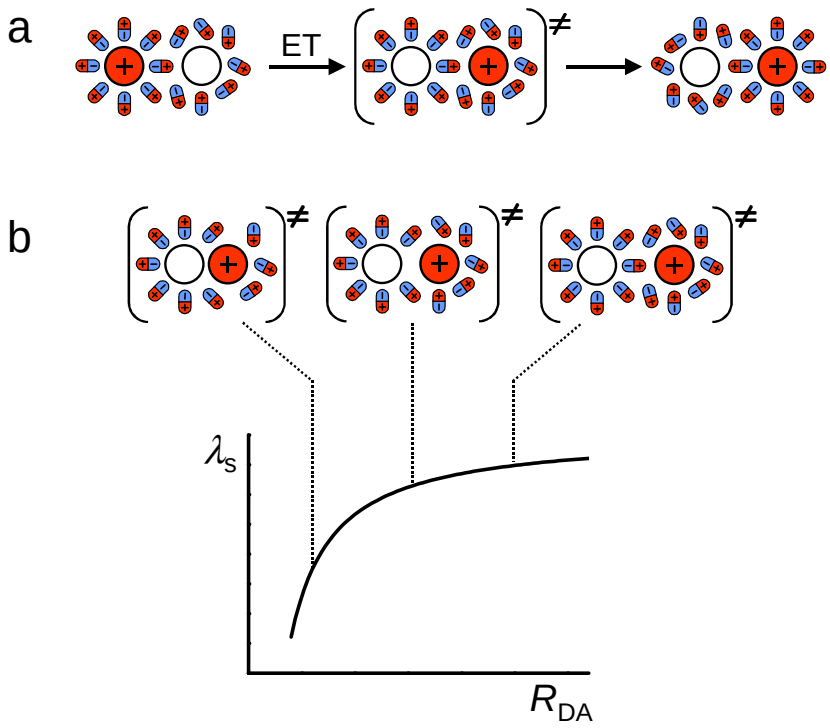

Fig. 6.8: Origin of the distance dependence of the medium reorganization energy λ_s, illustrated for two spherical reactants in a dipolar medium. (a) The medium polarization is frozen on the time scale of electron transfer, thus resulting in a nonequilibrium state directly after the charge is transferred (denoted with "≠"). This state is higher in energy than the initial state. (b) This increase in energy after charge transfer is dependent on the donor–acceptor separation R_{DA}.

It is known that distance-dependent activation energies of ET rates can arise from the distance dependence of both ΔG and λ_s on purely electrostatic grounds.[24, 76] In the present situation an important simplification is that, in contrast to charge separation reactions, for charge shift reactions ΔG (as calculated on the basis of Eq. (3.5)) is expected to have little or no distance dependence. Therefore, E_a for charge shift reactions should normally be distance dependent due only to λ_s. The measurements of the temporal evolution of the stimulated emission spectrum in the reference duplex X^+(AT) on the 200 fs to 60 ps time scale, discussed in Chapter 6, exclude any time-dependent (and therefore distance-dependent) change of ΔG that may be due to specific excited-state dynamics of the chromophore. Thus the present distance-dependent activation energies are attributed solely to the reorganization energy.

The origin of the distance dependence of the reorganization energy is illustrated in Fig. 6.8. The reactants and products of a hole shift reaction are modeled as spheres in a dipolar medium. Before the hole transfer, the polar medium is fully equilibrated to the

charge in the hole donor sphere (Fig. 6.8a). The solvent polarization is frozen on the time scale of the transfer since the time required for electron transfer is much less than that for nuclear motion. As a consequence, the energy of the system after hole transfer is higher than that of the initial state. This increase in energy after ET is dependent on the distance between the reactants (Fig. 6.8b). The closer the donor gets to the acceptor, the more the charge in the acceptor sphere begins to benefit from the frozen polarization around the donor sphere. In short, the reorganization energy decreases as the distance between donor and acceptor diminishes. As can be seen from Table 6.1, this behavior is reflected in the experimental activation energies.

In the absence of absolute values for ΔG (see Section 4.2.1), the analysis will start from a comparison of E_a values for the systems 3′-X^+AG and 3′-X^+AZ, assuming the in vivo oxidation potential of the easier-to-oxidize Z to be separated from G by $\Delta\Delta G = \Delta G_{3'\text{-}X^+AG} - \Delta G_{3'\text{-}X^+AZ} \approx 0.2$ eV. This value is based on the dynamics of hole transport from $G^{\bullet+}$, formed via photoinduced hole transfer to a Z separated from $G^{\bullet+}$ by one A:T base pair,[93] and is about 0.1 eV smaller than the difference of the oxidation potentials reported for the isolated nucleobases in solution.[80, 81] Utilizing $\Delta G_{3'\text{-}X^+AG} = -0.15$ eV and $\Delta G_{3'\text{-}X^+AZ} = -0.35$ eV, a fit of Eq. (3.3) to the corresponding E_a values in Table 6.1 provides a range of permissible values: $0.85\ \text{eV} \le \lambda \le 1.10$ eV. Importantly, the calculated reorganization energy seems to be mainly dependent on the donor–acceptor distance and almost independent of the nature of the hole acceptor G or Z. Applying the above values of ΔG to 3′-X^+G and to 3′-X^+AAZ yields $\lambda = 0.6 \pm 0.1$ and $\lambda = 1.4 \pm 0.1$ eV, respectively. It is problematic to extend this procedure to 3′-X^+Z since the (almost) zero activation energy does not allow to discriminate between an activationless or (slightly) inverted charge shift reaction. However, assuming that hole injection in 3′-X^+Z can be treated within the classical Marcus formalism $\lambda = 0.6 \pm 0.1$ eV is obtained, which is in agreement with 3′-X^+G.

In view of the uncertainties associated with the estimate of $\Delta\Delta G \approx 0.2$ eV, it should be explicitly stated that only the small range of $\Delta\Delta G$ values between 0.15–0.3 eV leads to self-consistent fits of the type cited above. This range is also in accord with the estimate from a theoretical analysis of chemical yield experiments.[92] The sensitivity of the fits to other parameters will be discussed in the next section.

It follows from this analysis that the steep distance dependence of the hole injection rate constants in X^+-modified DNA duplexes is due to two effects: (1) a decrease in couplings, and (2) an increase in reorganization energy with increasing donor–acceptor separation (Fig. 6.9). The ultrafast hole transfer time and the very low E_a value point to almost activationless hole transfer in 3′-X^+Z ($-\Delta G \approx \lambda$). In contrast, due to the higher oxidation

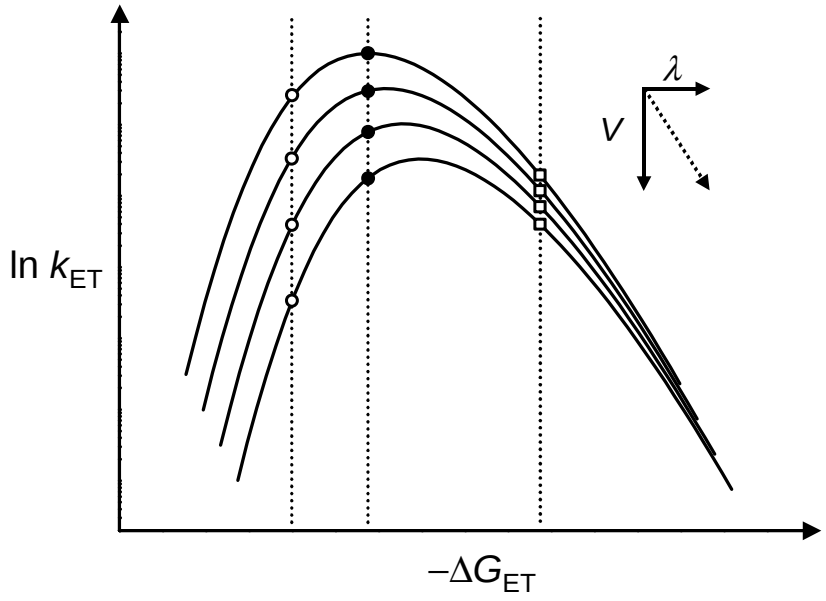

Fig. 6.9: Schematic illustration of the dependence of electron transfer rate constants on the donor–acceptor distance. The figure shows the combined effects of increasing λ_s and decreasing V. At constant values of $-\Delta G_{ET}$ different distance dependences are observed for the ET rate constant in the normal (○), activationless (●), and inverted (□) regions.

potential of G versus Z forward hole transfer in duplexes 3′-X^+G and 3′-X^+AG takes place in the normal region ($-\Delta G < \lambda$). This is consistent with the E_a values observed for these duplexes (Table 6.1). For all backward hole transfer reactions in the studied duplexes $-\Delta G >> \lambda$. At constant driving force the combined effects of increasing λ_s (shifting the ln k_{ET} vs $-\Delta G_{ET}$ curves to the right) and decreasing V (shifting the curves down) give rise to a weaker dependence of k_{ET} on distance in the activationless and inverted regions than in the normal region. This is reflected in the observed rate constants (Tables 4.2 and 6.1). In addition, the figure explains why the activation energies for backward charge shift show a weaker distance dependence and why for 3′-X^+AG and 3′-X^+AAZ only the forward hole transfer can be observed. Whereas Fig. 6.9 can explain the kinetic data in Table 6.1 on a qualitative level, for a more detailed treatment potential differences in coupling between G and Z and between the direct contact systems (3′-X^+Z and 3′-X^+G) and the superexchange samples (3′-X^+AZ, 3′-X^+AG, and 3′-X^+AAZ) also have to be considered.

The λ values estimated above contain a contribution from molecular (λ_v) as well as medium (λ_s) modes. Since λ_v is not expected to depend appreciably on the donor–acceptor separation[113] and since the overall λ for the contact cases studied here (3′-X^+G and 3′-X^+Z) is estimated to be rather small (about 0.6 eV), it can be concluded that λ_v is also likely to be rather small (a few tenths of an electronvolt), a result consistent with previous

work showing that for an organic donor–acceptor pair λ_v can be as small as 0.1 eV.[114]

Using the semiclassical electron transfer model of Bixon and Jortner,[115] the contribution of λ_v to the observed overall reorganization energy can be estimated. Within the framework of vibrational ET theory (Eq. (3.7)) the total activation energy E_a can be defined as the weighted sum of the activation energies $E_a(n)$ for each separate reaction channel into the product vibrational level n:

$$E_a = \sum_{n=0}^{\infty} \frac{k_n}{\sum_{n=0}^{\infty} k_n} E_a(n) \tag{6.3}$$

$$E_a(n) = \frac{(\Delta G + \lambda_s + n\hbar\omega_c)^2}{4\lambda_s} \tag{6.4}$$

In Eq. (6.3) k_n is the rate constant for ET into the product vibrational level n:

$$k_n = \frac{2\pi}{\hbar} \frac{V^2 \exp(-S_c)}{\sqrt{4\pi\lambda_s k_B T}} \frac{S^n}{n!} \exp\left(- \frac{(\Delta G + \lambda_s + n\hbar\omega_c)^2}{4\lambda_s k_B T} \right) \tag{6.5}$$

Since only relative values for k_n are needed for the calculation of the activation energy according to Eqs. (6.3) and (6.4), the electronic coupling is set to $V = 1$. The calculations of the activation energies according to Eqs. (6.3)–(6.5) were performed employing an effective vibrational frequency of 1500 cm^{-1} (see Section 3.2.2) and λ_v values ranging from 0.1–0.4 eV. The results are illustrated in Fig. 6.10.

Even in the normal region, some degree of nuclear tunneling associated with the high-frequency modes can be expected to reduce the activation energy relative to the classical limit. As a result of this tunneling, the quantity λ in Eq. (3.3) may be viewed as an effective λ corresponding to the sum of λ_s and some fraction of λ_v, expressed with a fractional coefficient α:

$$\lambda_{eff} = \lambda_s + \alpha\lambda_v \tag{6.6}$$

λ_{eff} can be rationalized as the reorganization energy in the classical Marcus expression Eq. (3.3), which reproduces the semiclassical activation energies. For the systems in the normal region (3′-X^+G, 3′-X^+AG, 3′-X^+AZ, and 3′-X^+AAZ), α values of only ~5–20% are required to obtain equivalence between the semiclassical E_a values and their classical counterparts. Thus the λ estimates cited above are expected to be dominated by λ_s.

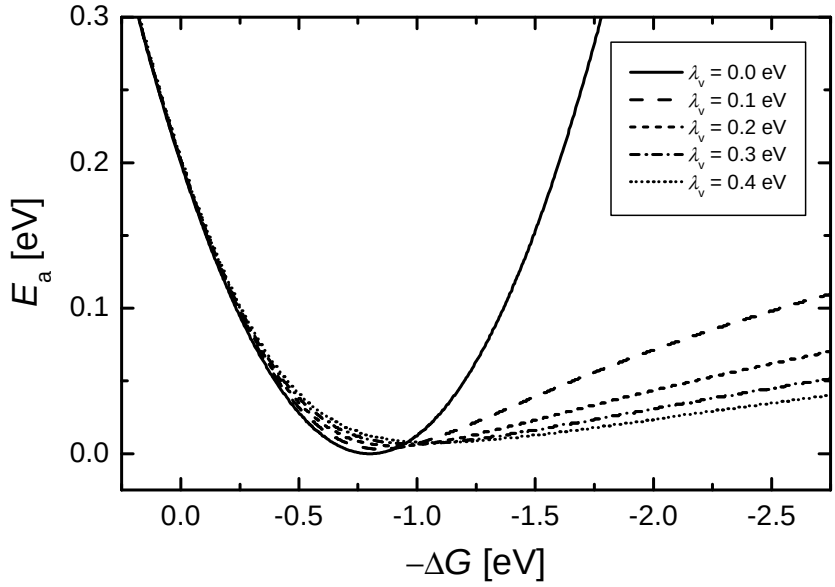

Fig. 6.10: Activation energies for hole transfer with different contributions from the vibrational reorganization energy λ_v. The activation energies were calculated according to the semiclassical model (Eqs. (6.3)–(6.5)) using $\lambda_s = 0.8$ eV and $\omega_c = 1500$ cm^{-1}.

This is illustrated in Fig. 6.10, which shows the semiclassical activation energies calculated for $\lambda_s = 0.8$ eV and a varying contribution of the vibrational reorganization energy. Based on the estimated range of permissible values for the classical reorganization energy of $0.85\text{ eV} \le \lambda \le 1.20\text{ eV}$, such a situation should be valid for the duplexes 3′-X$^+$AG and 3′-X$^+$AZ. Clearly, the quantum effects are small in the normal region. However, the contribution of the vibrational modes is essential in the inverted regime, i.e., for the backward charge shift processes. For the backward hole transfer process in 3′-X$^+$AZ an activation energy of 0.13 ± 0.01 eV was found (Table 6.1). An estimate for the vibrational contribution to the total reorganization energy for this specific duplex can also be obtained by globally applying semiclassical ET theory (Eq. (3.7)) to the forward and backward hole transfer rate constants. Using the values for k_1 and k_2 given in Table 6.1 and the above estimates for the medium reorganization energy $\lambda_s = 0.7$–0.8 eV, a variation of the driving force in the range $\Delta G = -(0.4\text{–}0.6)$ eV yields λ_v values in the range of 0.3–0.4 eV.[3] For these values of λ_s and λ_v and a driving force of about –2.3 eV for the backward charge transfer the semiempirical model predicts $E_a < 0.05$ eV (Fig. 6.10). This estimate is much lower than the observed value of 0.13 eV. Similar arguments can also be applied for the back transfer in the duplexes 3′-X$^+$Z and 3′-X$^+$G. The origin of the observed

[3] In this treatment, the range of acceptable values for ΔG and λ_s is constrained since the larger $(\Delta G + \lambda)$, the larger the value of V. E.g. using $\lambda_s = 0.7$ eV and $\Delta G = -0.5$ eV yields $\lambda_v = 0.4$ eV and $V = 50$ cm^{-1}.

high activation energies for the backward charge shift in 3′-X^+Z, 3′-X^+G, and 3′-X^+AZ cannot be explained yet.

6.3.3 Sensitivity of the Reorganization Energy to Parameters

The values of the distance-dependent reorganization energy derived in the last section are based on estimates for the driving force in the DNA donor–acceptor systems and also on the difference in ΔG for duplexes containing guanine or 7-deazaguanine as the hole acceptor. In the following, the sensitivity of λ to changes in these parameters will be analyzed and lower limits will be estimated for the total reorganization energy at different donor–acceptor separations.

The main input parameter is the difference in the driving force between 3′-X^+AG and 3′-X^+AZ, $\Delta\Delta G = \Delta G_{3'\text{-}X^+AG} - \Delta G_{3'\text{-}X^+AZ}$. As stated above, there are indications that the difference between the in situ potentials of G and Z may be as low as 0.15 eV.[92, 93] The absolute values of λ also depend on the ΔG values utilized for 3′-X^+AG and 3′-X^+AZ. More specifically, a variation of $\pm\delta$ in the ΔG values, maintaining the value for $\Delta\Delta G$, yields a variation of $\pm 2\delta$ in the fitted λ values. Using the minimum values $\Delta G_{3'\text{-}X^+AG} = 0.0$ eV and $\Delta\Delta G = 0.15$ eV the following lower limits for the reorganization energy can be estimated: $\lambda = 1.1 \pm 0.1$ eV for 3′-X^+AAZ, $\lambda = 0.6$–0.8 eV for 3′-X^+AG and 3′-X^+AZ, and $\lambda = 0.2$–0.4 eV for the direct contact systems 3′-X^+G and 3′-X^+Z. All values contain a contribution from λ_v, which is independent of the donor–acceptor separation.[113] As indicated by the small total λ for 3′-X^+G and 3′-X^+Z this contribution must be small, in agreement with the analysis in the previous section.

In addition to the above uncertainties, potential entropy contributions to ΔG and λ and the temperature dependence of these parameters have been neglected. Therefore the absolute values of the reorganization energy have to be considered as first estimates.

6.3.4 Comparison between Theory and Experiment

As shown in the previous sections, the distance-dependent activation energies can be explained by an increase in the medium reorganization energy as the donor–acceptor distance in the DNA duplexes is getting larger. The magnitude of λ_s, as well as the degree of distance dependence, rely on a number of factors including the effective size and shape of the donor and acceptor sites, their effective separation distance, and the effective polarity of their surroundings.[24, 116] With respect to the last point, the DNA duplex is a

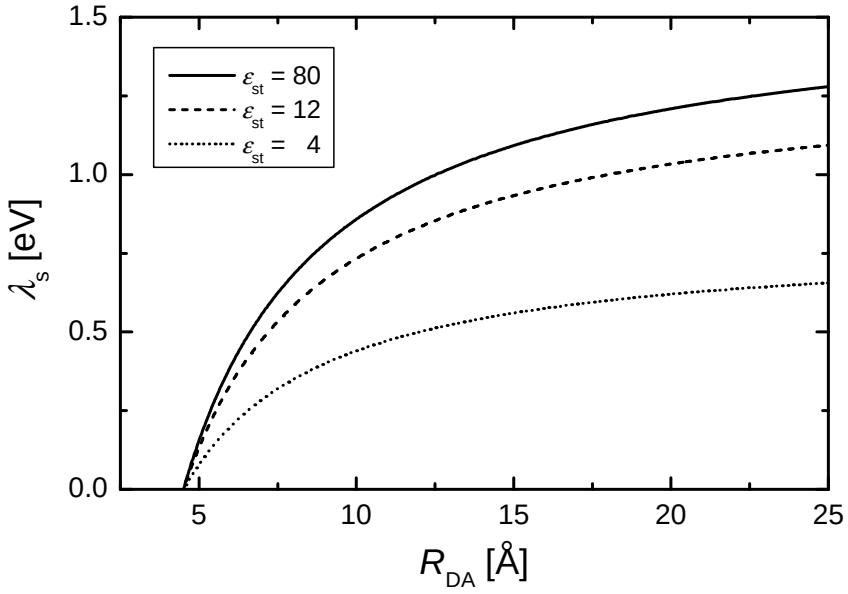

Fig. 6.11: Distance dependence of the medium reorganization energy λ_s according to the two-sphere-model (Eq. (3.4)). The radii of both the donor and acceptor spheres were taken to be 4.5 Å and the optical frequency dielectric constant was set to $\varepsilon_{op} = 2.0$.

heterogeneous dielectric environment. The combined effects of the polar stacked nucleobases, the charged sugar–phosphate backbone, and the surrounding water have to be taken into account. For the DNA base stack no reliable value for the static dielectric constant ε_s has been reported yet. Estimates range from $\varepsilon_{st} = 2$ to 12.[46, 72, 100] As can be seen from Fig. 6.11, varying the static dielectric constant within this range yields large changes in the magnitude of the medium reorganization energy.

The first model calculations of λ_s in duplex DNA reported by Tavernier et al. were based on the explicit consideration of the dielectric heterogeneity of the surrounding medium.[46] In these calculations a DNA duplex in which two of the DNA bases served as donor and acceptor sites was considered. The base stack was described with the dielectric constants of pyridine ($\varepsilon_{op} = 2.27$ and $\varepsilon_{st} = 12.4$). The sugar–phosphate backbone regions were assigned characteristics between those of pyridine and water, with $\varepsilon_{op} = 1.90$ and $\varepsilon_{st} = 20.0$, whereas water was used as surrounding solvent ($\varepsilon_{op} = 1.77$ and $\varepsilon_{st} = 78.3$). These calculations yielded very high absolute values for λ_s (e.g. $\lambda \approx 3.0$ eV at 15 Å).[46] However, the reported increase of about 1 eV as the donor–acceptor distance changes from 3–4 Å (contact) to about 10 Å (two intervening A:T base pairs) is consistent with the observed behavior in the X^+-modified duplexes. Based on their calculations, Tavernier et al. suggested that the main distance dependence of the rate constant for hole transfer in DNA might be due to the distance dependence of the medium reorganization energy.[46] In

contrast, in a recent quantum chemical study the reorganization energy was found to exhibit only a weak distance dependence, and the contribution of λ to the decay parameter β of the rate constant was estimated to be only about 0.1 $Å^{-1}$.[72] The large difference to the previous results were mainly related to the high dielectric constants used by Tavernier and coworkers.

Both theoretical calculations are based on unperturbed DNA donor–acceptor systems with two of the DNA bases serving as donor and acceptor sites, respectively. From space-filling molecular models of DNA duplexes it is evident that within the base stack there is no substantial amount of space for water molecules.[46] In this case, the magnitude of the reorganization energy depends predominantly on whether the DNA base stack is assumed to be a low or medium dielectric region. However, this situation might be different in actual DNA donor–acceptor systems. On the one hand any modification is expected to perturb the structure to some extent and on the other hand the attached or incooperated donor or acceptor molecules might be accessible to the polar solvent molecules or in close contact with the charges and dipoles on the DNA backbone.

The contribution of distance-dependent activation energies to the hole transfer kinetics measured for other DNA-based systems is still an open question. In general, a significant contribution of the *FC* factor to the observed distance dependence of the rates in molecular donor–acceptor systems may be expected if the medium reorganization energy is appreciable and the charge-transfer step is relatively short-range, i.e., occurring over ≤10–15 Å (see Fig. 6.11). In addition, the driving force should be in the normal region ($-\Delta G < \lambda$) of the Marcus expression.[4] The most reliable estimates of the distance dependence of hole transfer rates in DNA have been published by Lewis et al. and by Giese and coworkers.[55, 60] In the following, the results for X^+-modified duplexes will be compared to these specific DNA-based donor–acceptor systems.

Lewis et al. have investigated the distance dependence of photoinduced hole transfer for a family of synthetic DNA hairpins in which a stilbene dicarboxamide (SA) forms a bridge connecting two oligonucleotide strands.[9, 66] Base pairing between these strands results in the formation of hairpins in which the stilbene is approximately parallel to the adjacent base pair. In analogy to 9-amino-6-chloro-2-methoxyacridine the singlet stilbene is selectively quenched by guanine, but not by the other nucleobases, via a charge-transfer mechanism in which the stilbene singlet state is the hole donor and guanine is the hole acceptor. With time-resolved fluorescence and absorption measurements the fluorescence quenching and the formation of the stilbene anion radical $SA^{-\bullet}$ was monitored as a function of the number of A:T base pairs between the donor and the acceptor. This process shows

[4] Related effects in the inverted region have also been noted.[117, 118]

an exponential decrease in the rate constant with distance described by a parameter $\beta = 0.7 \pm 0.1$ Å^{-1}.[9, 66] Obviously, this relatively small value mainly reflects the decay of the electronic couplings with distance and any potential contribution of a distance-dependent activation energy must be small. In these hairpins the end-capped chromophore is partially surrounded by water. Therefore the medium reorganization energy may be appreciable for the ET process. Additionally the measurements were performed at short D–A distances (4–17 Å) where a large contribution of a distance-dependent *FC* factor is expected. The fact that in these experiments there was no observable indication of an increase in λ with distance suggests an activationless or inverted injection process in the SA-hairpins. As discussed above, a distance-dependent reorganization energy has a weaker effect on the ET rates in the activationless and inverted regime than in the normal region.

However, the driving force for hole transfer from ^{1}SA* to G was reported to be about –0.2 eV. Based on the estimates for the reorganization energy in Section 6.3.2, such a driving force would be in the normal region. In the absence of in vitro potentials ΔG was estimated from the redox potentials of the chromophore and the guanine nucleobase in solution. It is known that the strong stacking interactions in the DNA hairpins may lead to significant changes in the oxidation and reduction potentials of the donor and acceptor molecules. A driving force that is by a few tenths of an electronvolt more negative would place the injection process in the SA-linked hairpins into the activationless or inverted region. Such a situation would be consistent with the ultrafast injection rate measured in the direct contact system and the observation that the hole transfer rate is not very sensitive to changes in the driving force. Replacing G by Z leads to changes in the observed rate of less than a factor of two,[93] whereas much larger changes are observed in the X$^+$-labeled duplexes (Chapter 4). Furthermore, even in the presence of a distance-dependent reorganization energy its effect on the hole transfer rates may not be reflected in the experimental data by Lewis and coworkers. In contrast to the charge shift occurring in X$^+$–DNA, in the charge separation reaction between SA and G the driving force should display a distance dependence of its own (Eq. 3.6). The values of ΔG and λ_s may display a much stronger dependence on the SA–G distance than the overall rate constants because ΔG and λ_s are summed to calculate E_a and some of their differences may cancel each other when the rate constant is calculated.[46] Therefore even if the reorganization energy is appreciable the overall changes in thermal activation with increasing donor–acceptor separation might be small.

In conclusion, the apparent discrepancy between the distance dependence of the rates observed in the SA-hairpin system and in X$^+$-modified DNA may be explained with different energetics and the inherent differences between charge shift and charge separation reactions. Additional contributions to the larger distance dependence in

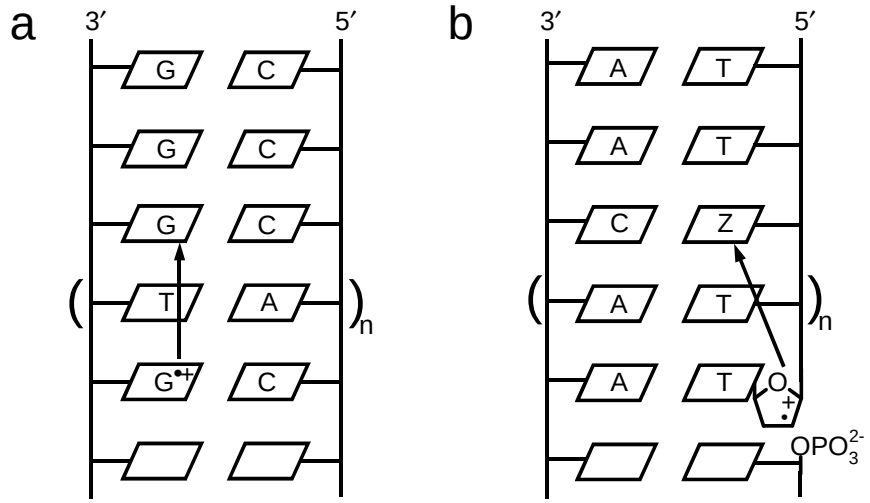

Fig. 6.12: Assays for the determination of the distance dependence of the hole transfer rate constant used by Giese and coworkers.[55] (a) Hole transfer from a single $G^{\bullet+}$ to a GGG unit, (b) hole transfer from a deoxyribose radical cation to a Z (or G).

X^+–DNA duplexes could result from a larger energy difference between the initial and bridge states or from weaker coupling between the excited hole donor and the bridge.[75, 119] Due to its apparent insensitivity to changes in the energy parameters stilbene-linked hairpins seem to be well-suited for the investigation of the pure electronic β in DNA.

A second reliable approach to the determination of the distance dependence of ET rates in DNA are the thermal hole transfer studies by Giese and coworkers which are based on relative strand-cleavage efficiencies.[55] Through heterolytic cleavage, a deoxyribose radical cation is generated which selectively oxidizes a nearby guanine nucleobase. The charge shift from this guanine radical cation to a GGG unit was studied varying the number of intervening A:T base pairs (Fig. 6.12a) and a decay parameter $\beta = 0.7 \pm 0.1$ Å^{-1} was reported.[61] From a kinetic analysis of the chemical yield data provided by these experiments a medium reorganization energy of about 0.4 eV is obtained, which indicates a relatively low effective polarity of the surrounding medium.[58]

However, Giese et al. have also investigated the distance dependence of the primary charge transfer step from the sugar radical cation to a guanine or 7-deazaguanine acceptor (Fig. 6.12b). Recent results indicate that an exponential distance dependence is only observed for donor–acceptor distances >9 Å.[120] For these distances the relative rate constants yield a decay parameter $\beta = 0.55 \pm 0.1$ Å^{-1}. At shorter distances the hole transfer occurs faster (by a factor of about 10) than expected for this β value. As in the X^+-modified duplexes this effect can be ascribed to the distance dependence of the medium reorganization energy. The finding that the effect is smaller can be rationalized by the fact

that the shortest D–A distance accessible is 6.1 Å. Therefore, this system seems to be insensitive to the large changes in λ_s which occur at shorter distances (see Fig. 6.11).

A comparison of the two experimental asseys employed by Giese and coworkers suggests that the results may be rationalized in terms of different effective polarities of the medium surrounding the hole donor. In the $G^{\bullet+}$/GGG system the guanine radical cation donor is located within the base stack. The medium reorganization energy of about 0.4 eV, obtained from kinetic modeling of these data, is relatively small and no contribution to the distance dependence of the rates is observed. Since both the donor and acceptor molecules are intrinsic DNA bases the structural perturbations can be assumed to be small. Thus the low reorganization energy might reflect the effective polarity provided by a largely unperturbed DNA environment. When the sugar radical cation serves as the hole donor, the data are consistent with a contribution from a distance-dependent activation energy, and therefore with an appreciable value of λ_s. Such an interpretation would be in accord with the increased solvent accessibility of a charge on the sugar–phosphate backbone and the interaction with the phosphate ions in the immediate environment. Moreover, the method used by Giese and coworkers for charge injection is based on the heterolytic cleavage of the phosphate ester C,O-bond in a 4′-DNA radical.[55] This strand breakage upon charge generation and the resulting changes in local structure may further promote solvation of the deoxyribose radical cation.

In analogy, the relatively large reorganization energies for the X^+-labeled DNA duplexes point to a local defect structure at the chromophore binding site that allows for a relatively large effective dielectric constant. Such a deviation from the standard B-form structure may lead to an increased solvent accessibility to the intercalated chromophore. However, in the absence of detailed structural information it cannot be excluded that some part of the 9-amino-6-chloro-2-methoxyacridine is not fully intercalated and may therefore be exposed to the solvent.

6.4 Conclusions

The temperature-dependent measurements presented in this chapter verify the assumption that the steep distance dependence of the hole injection rate constant in X^+-modified DNA duplexes is not solely caused by a decrease in electronic couplings, but also by a concomitant increase in activation energy with increasing donor–acceptor separation. An analysis of the rates and activation energies shows that the hole transfer rate constants slow down by a factor of about 100 due to activation and by a factor of 20 due to the decrease in electronic couplings. The latter value corresponds to an electronic tunneling parameter of

$\beta \approx 0.9$ Å^{-1}, which is in agreement with estimates from the literature.[55, 60] An artificial intramolecular donor–acceptor system, in which the distance dependence of the activation parameters is larger than that of the electronic factor, has been reported before.[121] There, the large overall distance dependence of the rate constant for ET from Os^{II} to Ru^{III}, linked by a polyproline bridge, was reported to be due to a superposition of the decay of the electronic couplings ($\beta_{el} = 0.68$ Å^{-1}) and that of the nuclear factor ($\beta_{FC} = 0.91$ Å^{-1}).

The increase in thermal activation energy with distance can be self-consistently explained within the framework of a distance-dependent reorganization energy. These fits yield lower limits for the medium reorganization energy of about 0.8 eV at 10 Å donor–acceptor separation. The quantitative modeling of λ_s for the present DNA duplexes would require detailed information about the structure of the X^+ chromophore in its binding site, including any specific perturbations of the DNA structure. This information is expected from a forthcoming NMR structure. However, the large reorganization energy strongly suggests the presence of highly polarizable molecular dipoles or ions in the immediate environment of either the donor and/or acceptor species.

It is a task for the future to test different donor–acceptor systems derived from proteins or DNA duplexes for the contribution of distance-dependent Franck–Condon factors to the empirical attenuation factor β. In such systems β is often discussed exclusively in terms of electronic couplings, although the potentially crucial role of the Franck–Condon factor has been noted in the general electron transfer literature.[117, 118, 121, 122]

7 Nucleobase Oxidation Kinetics and the Role of the Nucleobase Environment

In the previous chapters the distance and temperature dependence of the hole transfer rate constants in 9-amino-6-chloro-2-methoxyacridine-modified DNA were studied with duplexes of the type 3′-$X^+(A)_nB$ and 5′-$X^+(A)_nB$, where B = G or Z and n = 0–2. Increasing the driving force by replacing guanine with its easier-to-oxidize analog 7-deazaguanine was found to increase the hole transfer rates substantially. Moreover, the temperature-dependent measurements in Chapter 6 show that hole transfer over one A:T base pair can be significantly activated.

This activated behavior and the accompanying sensitivity of the hole transfer rates to changes in driving force are utilized in the experiments discussed in Section 7.1. The influence of the oxidation potential of the hole acceptor on the transfer rate is investigated employing modified purine nucleobases as potential hole acceptors. Section 7.2 deals with the role of the intervening bridge comparing the systems 3′-$X^+(B)_nZ$ with B = A and T. Whereas all experiments reported so far involved hole donors and acceptors located on the same strand of the double helix an interstrand hole transfer experiment will be presented in Section 7.3. Finally, Section 7.4 discusses the influence of the identity of the nucleobases bracketing a hole accepting base on the dynamics and energetics of hole transfer (Section 7.4).

7.1 Hole Transfer to Various Purine Nucleobases

As illustrated by guanine and 7-deazaguanine, which differ only in the replacement of N_7 by a CH group, subtle changes in the structure of a purine base can lead to a significant increase or decrease in the oxidation potential. This change is reflected in the observed hole transfer rates (Chapter 4). In this section, the modified purine nucleobases inosine (I), 7-deazaadenine (A^Z), 2-aminopurine (2AP), and 8-bromoguanine (8BrG) are tested as potential hole acceptors. The chemical structures of these nucleobase analogs are shown in Fig. 7.1. In addition to changes in the redox potential the chemical modification of adenine

Duplexes 3′-X$^+$P P = G, Z, I, 2aP, 8BrG, A^z
5′-GCG TTA TAA **P**(**X**$^+$)A TAA TAT GCG-3′

Duplexes 3′-X$^+$AP P = G, Z, I, 2aP, 8BrG, A^z
5′-GCG TTA TA**P A**(**X**$^+$)A TAA TAT GCG-3′

Duplexes 3′-X$^+$TZ and 3′-X$^+$TTZ
5′-GCG TTA AA**Z T**(**X**$^+$)A TAA TAT GCG-3′
5′-GCG TTA A**ZT T**(**X**$^+$)A TAA TAT GCG-3′

Duplex 3′-X$^+$Z$_c$
5′-GCG TTA AAT **C**(**X**$^+$)A TAA TAT GCG-3′
3′-CGC AAT TTA **Z A** T ATT ATA CGC-5′

Duplex 3′-X$^+$A$_c$Z$_c$
5′-GCG TTA AA**C T**(**X**$^+$)A TAA TAT GCG-3′
3′-CGC AAT TT**Z A A** T ATT ATA CGC-5′

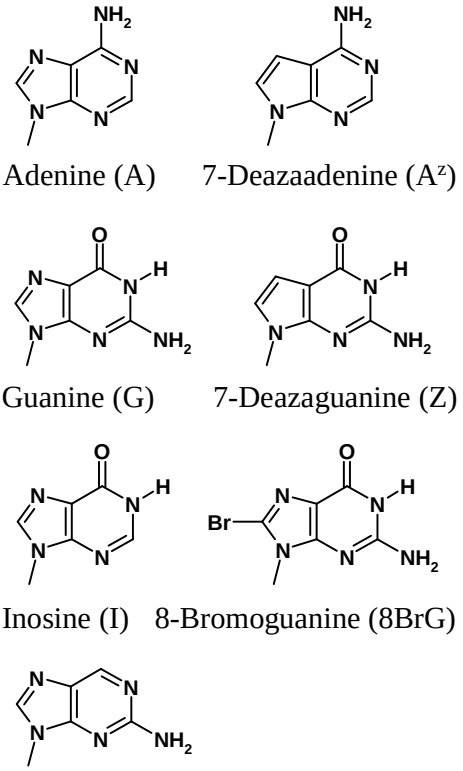

Fig. 7.1: Chemical structures of the modified purine nucleobases and base sequences of the X$^+$-modified single strands utilized to produce the duplexes discussed in Sections 7.1–7.3. The counter strands are not shown. However, all nucleobases were placed in a standard Watson–Crick pair and an adenine was placed opposite to X$^+$. Both the X$^+$-modified strands and the counter strands are shown for the duplexes 3′-X$^+$Z$_c$ and 3′-X$^+$A$_c$Z$_c$.

or guanine can also influence the electronic couplings due to changes in size, electronic distribution, and even the nucleoside sugar conformation.[123]

Using time-resolved transient absorption spectroscopy the photoinduced dynamics in the X$^+$-modified duplexes 3′-X$^+$P and 3′-X$^+$AP, with P = I, 2AP, 8BrG, or A^z, were studied. The sequences of the oligonucleotide strands are shown in Fig. 7.1. The results will be compared to the systems containing A, G, and Z, which have been discussed in Chapter 4. In the direct contact systems 3′-X$^+$P strong, base-specific electronic interactions between the hole donor and acceptor will play an important role. These effects are expected to be minimized in 3′-X$^+$AP, where the local chromophore environment always consists of two flanking A:T base pairs and the variable base pair is placed one A:T base pair away from X$^+$ in the 5′ direction of the X$^+$-modified strand.

7.1.1 Experimental Results

Steady-State Spectroscopy

The sequences of the duplexes 3′-X^+P and 3′-X^+AP are shown in Fig. 7.1. The counterbase to adenine (A), 2-aminopurine (2AP), and 7-deazaadenine (A^z) is thymine (T), whereas the counterbase for guanine (G), inosine (I), 8-bromoguanine (8BrG), and 7-deazaguanine (Z) is cytosine (C).

The steady-state absorption spectra of all duplexes 3′-X^+P and 3′-X^+AP are similar to that of X^+(AT). Figure 7.2 shows representative absorption spectra of 3′-X^+AA^z and 3′-X^+A(2AP). In the latter, the X^+ $S_2 \leftarrow S_0$ band overlaps with the red absorption tail of the 2AP nucleobase.[124]

The fluorescence spectra of 3′-X^+(2AP), 3′-X^+I, 3′-X^+A(2AP), and 3′-X^+AI are similar in both spectral features and in overall intensity to that of X^+(AT). The duplexes 3′-X^+AA^z and 3′-X^+A(8BrG) display similar overall spectral features but a lower fluorescence intensity comparable to the one in 3′-X^+AG. Almost complete quenching of the fluorescence is found in 3′-X^+(8BrG) and 3′-X^+A^z.

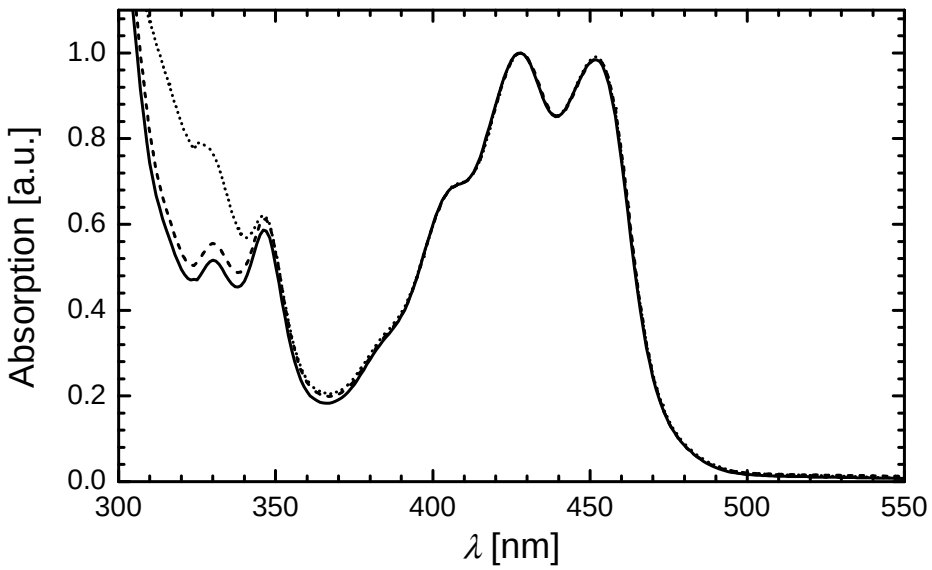

Fig. 7.2: Normalized steady-state absorption spectra of the duplexes X^+(AT) (—), 3′-X^+AA^z (---), and 3′-X^+A(2AP) (·····) at 283 K. In 3′-X^+A(2AP) the X^+ $S_2 \leftarrow S_0$ band overlaps with the absorption of the 2AP nucleobase.

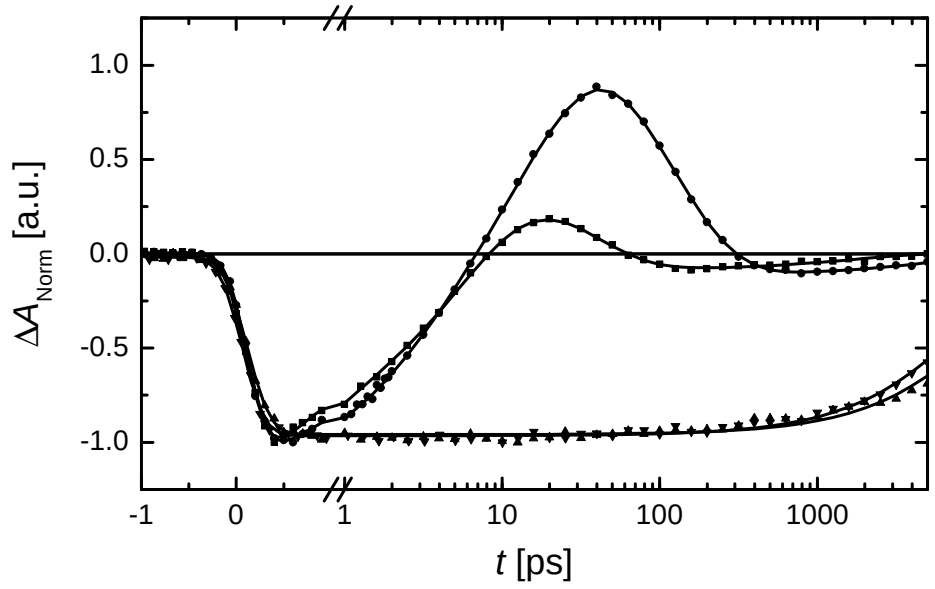

Fig. 7.3: Transient pump-probe kinetics measured in the duplexes 3′-X^+A^z (•), 3′-X^+I (▲), 3′-X^+A(8BrG) (■), and 3′-X^+(2AP) (▼) using 455 nm pump pulses and 500 nm probe pulses. The solid lines are nonlinear least-squares fits to the kinetic data, whose parameters are given in Table 7.1.

Hole Transfer in Duplexes 3′-X^+P and 3′-X^+AP

The kinetics observed in duplexes 3′-X^+P and 3′-X^+AP using 455 nm pump and 500 nm probe pulses are shown in Figs. 7.3 and 7.4. Under these conditions the probe pulses monitor both the decay of the excited state $^1(X^+)^*$ by stimulated emission and the absorption of the acridine radical $X^\bullet$ (Chapter 4). In both 3′-X^+I and 3′-X^+(2AP) the excited state decays monoexponentially with a lifetime too long for the 6 ns detection window of the femtosecond laser system (Fig. 7.3). As shown in Fig. 7.4, almost identical transient dynamics are observed for the duplexes 3′-X^+AI and 3′-X^+A(2AP). In analogy to the reference duplex X^+(AT), nanosecond absorption spectroscopy yields excited-state decay times of 18 ns for all these duplexes (Table 7.1).

Placing an 8BrG:C or a A^z:T pair next to or separated by one A:T base pair from X^+ leads to fluorescence quenching and spectroscopic features similar to those observed before in the G containing duplexes 3′-X^+G and 3′-X^+AG. In the direct contact systems 3′-X^+A^z and 3′-X^+(8BrG) the $^1(X^+)^*$ excited-state decay occurs on a picosecond time scale and the absorption of the product state $X^\bullet$, formed via photoinduced hole transfer, is observed (Fig. 7.3). For both duplexes the excited state and the radical state decay with time constants a little longer than observed in 3′-X^+G (Tables 7.1 and 7.2). As can be seen

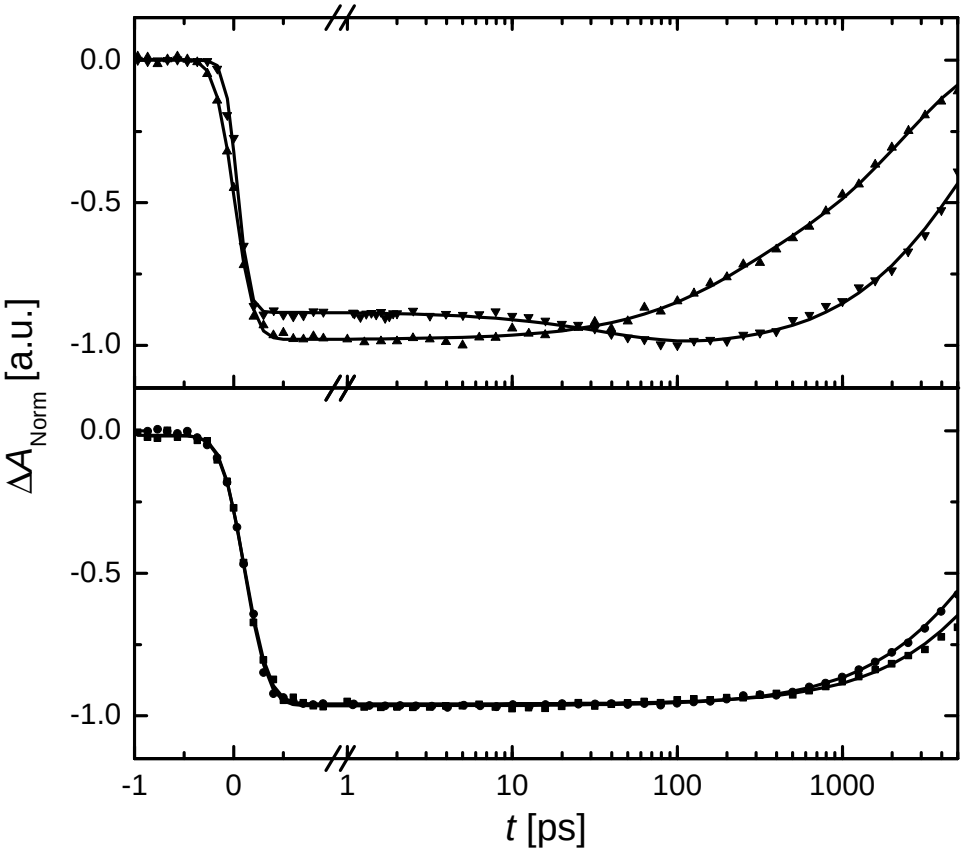

Fig. 7.4: Transient pump-probe kinetics measured in the duplexes 3′-X^+A(8BrG) (▼), 3′-X^+AA^z (▲), 3′-X^+AI (●), and 3′-X^+A(2AP) (■) using 455 nm pump pulses and 500–530 nm probe pulses. The solid lines are nonlinear least-squares fits to the kinetic data, whose parameters are given in Table 7.1.

from Table 7.1, an additional small component (10–20% amplitude) is needed to describe the excited-state decay in 3′-X^+A^z and 3′-X^+(8BrG) satisfactorily. Only a small fraction (<10%) of long-lived background signal is observed in the transient kinetics.

Placing A^z or 8BrG one A:T base pair away from X^+ leads to quenching of $^1(X^+)^*$ on a nanosecond time scale (Fig. 7.4), similar to 3′-X^+AG (Chapter 4). The lifetime of $^1(X^+)^*$ is 7.9 ns in 3′-X^+A(8BrG) and 2.3 ns in 3′-X^+AA^z. In both systems the ground-state recovery occurs on a time scale identical to the excited-state lifetime. However, in analogy to the direct contact systems the hole transfer kinetics in 3′-X^+A(8BrG) and 3′-X^+AA^z contain a small additional component that is not found in the kinetics of 3′-X^+AG (Table 7.1). In 3′-X^+A(8BrG) the additional component has a lifetime of ~100 ps and an amplitude of 10–15%, depending on the probe wavelength (Table 7.1). In the stimulated emission region a short time component with a lifetime of 150 ps (20%) can be observed in the duplex 3′-X^+AA^z.

Table 7.1 Numerical parameters of the fit functions displayed as solid lines in Figs. 7.3 and 7.4.

Duplex	τ_1 [ps]	ΔA_1	τ_2 [ps]	ΔA_2	τ_3 [ps]	ΔA_3	τ_4 [ns][b]	ΔA_4
3′-X^+A^z	2.3	–0.53	16.5	–2.17	111	1.68	>5	–0.16
3′-X^+(8BrG)	0.5	–0.37	6.3	–1.42	31	0.62	2.0	–0.09
3′-X^+I	-	-	-	-	-	-	>5	–1.00
3′-X^+(2aP)	-	-	-	-	-	-	>5	–1.00
3′-X^+AA^z	-	-	-	-	180	–0.23	2.0	–0.77
3′-X^+A(8BrG)[a]	-	-	-	-	42	0.13	>5 (7.9)	–1.01
3′-X^+AI	-	-	-	-	-	-	>5 (18)	–1.00
3′-X^+A(2aP)	-	-	-	-	-	-	>5 (18)	–1.00

$\Delta A_{1,2,3}$ are the relative amplitudes of the time constants $\tau_{1,2,3}$. [a] For all measurements the probe wavelength was set to 500 nm except for 3′-X^+A(8BrG), where the probe wavelength was at 530 nm. [b] The time constants in the nanosecond region cannot be determined precisely as the delay line is restricted to times below 6 ns. Values in parentheses were measured with the nanosecond pump-probe setup.

7.1.2 Discussion

As can be seen from Fig. 3.4, ET reactions are not sensitive to ΔG near the top of the Marcus curve ($\Delta G \approx \lambda$). Therefore, a thermally activated electron transfer reaction ($\Delta G << \lambda$) must be used to correlate changes in ET rate constants with those in the oxidation potential of the hole donor E_{ox}. As shown in Chapter 6, this requirement is met by X^+-modified duplexes. The forward hole transfer reactions in 3′-X^+AZ and 3′-X^+AG, for instance, were found to be activated by about 0.1 eV and 0.2 eV, respectively.

The results of the transient absorption measurements on the duplexes 3′-X^+P and 3′-X^+AP are summarized in Tables 7.2 and 7.3. In the presence of only A and T nucleobases (duplex X^+(AT)) there are no hole transfer reactions from $^1(X^+)^*$ and the unquenched excited-state lifetime of X^+ in duplex DNA of 18 ns is observed (Chapter 4). The excited-state decay times listed in Table 7.3 indicate that neither 2AP nor I are oxidized within the lifetime of $^1(X^+)^*$. In contrast, the four purine nucleobases G, Z, A^z, and 8BrG are capable of undergoing photoinduced hole transfer with X^+. This points to favorable hole transfer free energies due to appropriately low oxidation potentials of these nucleobases in duplex DNA. However, the oxidation potential is not the only factor controlling hole transfer rates. As stated before, chemical modification of the purine nucleobases may significantly influence the electronic couplings via either different electronic distributions or structural changes.

Table 7.2: Excited-state lifetimes and forward and backward hole transfer rate constants in the duplexes 3′-X^+P at 283 K.

Duplex	τ_{ES} [ps]	k_1 [s^{-1}][a,b]	k_2 [s^{-1}]
3′-X^+A^z	2.3 (21%) 16.5 (79%)	6.1×10^{10}	7.1×10^{9}
3′-X^+(8BrG)	0.5 (19%) 6.3 (81%)	1.6×10^{11}	2.0×10^{10}
3′-X^+G	3.8	2.6×10^{11}	2.9×10^{10}
3′-X^+Z	0.7	1.4×10^{12}	1.6×10^{11}

[a] Forward charge shift rate constants calculated from the excited-state lifetimes according to Eq. (4.5).

[b] Based on the majority component of τ_{ES} for 3′-X^+A^z and 3′-X^+(8BrG).

Origin of the Biexponential Kinetics in the Duplexes Containing A^z and 8BrG

The biexponential kinetics observed in the duplexes containing A^z or 8BrG may originate from such structural effects. Seela et al. have reported that the replacement of A by A^z shifts the melting transition of DNA duplexes to lower temperatures.[125] Upon replacement of one A by A^z in the duplex $d(A–T)_6$ the melting point was lowered by 3 °C. This effect was explained by an altered dipole moment of A^z, which might influence the strength and orientation of stacking interactions of this base within a DNA duplex. Additionally, due to changed donor or acceptor properties of N_1 and the amino group because of the N_7–CH replacement, hydrogen bonding in the A^z:T base pair could be affected.[125] In contrast, in a more recent study of the same group a $d(A^z–T)_6$ duplex was reported to be slightly more stable than $d(A–T)_6$.[126] However, the complete replacement of A by A^z may affect the overall structure of this duplex and can therefore give no reliable indication of the effect of a single A–A^z replacement, as, e.g., in the duplex 3′-X^+AA^z. In this context, recent computational results suggest that the overall structural changes are likely to be small when an A:T base pair is replaced by A^z:T.[72]

There is more known about the structure of 8BrG in duplex DNA. Due to the bulky bromine substituent 8-bromoguanine adopts the syn orientation about the glycosyl link. This is in contrast to standard B-form DNA where the nucleotides are found exclusively in the anti configuration.[123] Therefore, the incorporation of 8BrG is expected to lead to a local defect structure, a feature which is most likely responsible for the biexponential kinetics in 3′-X^+(8BrG) and 3′-X^+A(8BrG). However, the structures of the A^z and 8BrG containing X^+-labeled duplexes are not known. Thus conclusions on the role of base-

Table 7.3: Excited-state lifetimes and forward hole transfer rate constants in the duplexes 3′-X^+AP at 283 K and relative one-electron oxidation potentials of purine nucleobases in solution.

Duplex	τ_{ES} [ns]	k_1 [s^{-1}][a]	Base	E_{ox}[c] [eV]
3′-X^+(AT)	18.0	-	A	0.45-0.49
3′-X^+AI	18.2	-	I	~0.2
3′-X^+A(2AP)	18.2	-	2AP	-
3′-X^+A(8BrG)	7.9[b]	7.1×10^7	8BrG	~0.01
3′-X^+AG	6.9	8.9×10^7	G	0.0
3′-X^+A^zA	2.0[b]	4.4×10^8	^zA	~0.01
3′-X^+AZ	0.011	9.1×10^{10}	Z	–0.32

[a] Forward charge shift rate constants calculated from the excited-state lifetimes according to Eq. (4.5).
[b] Additional picosecond time component (see Table 7.1). [c] The value of G has been set to 0.0 eV. The references for the oxidation potentials are given in the text.

specific structural effects in the observed biexponential hole transfer dynamics must await future NMR structural studies. The following discussion of the hole transfer rate constants will focus exclusively on the decay components with the largest amplitudes (>75% amplitude) in the A^z or 8BrG duplexes. These rates reflect the hole transfer dynamics of the large majority of duplexes.

Hierarchy of the Rate Constants for Nucleobase Oxidation

In the following, it will be investigated whether the results obtained for the duplexes 3′-X^+AP and 3′-X^+P (Tables 7.2 and 7.3) can be solely rationalized by differences in the redox potentials of the purine nucleobases (Table 7.3). As the absolute values in the literature vary considerably only differences in oxidation potentials with respect to the value of guanine are reported in Table 7.3. Adenine[12, 13] and inosine[60, 127] are the bases of highest oxidation potentials. This is reflected in the dynamics, showing that A and I are not oxidized within the lifetime of $^1(X^+)^*$. No oxidation potential could be found for the nucleobase analog 2-aminopurine. The experimental results strongly suggest that the potential for this base analog is similar to those reported for A and I.

For 7-deazaguanine the ultrafast rates observed in 3′-X^+Z and 3′-X^+AZ are consistent with its low oxidation potential.[80, 81] The oxidation potentials of A^z, G, and 8BrG in solution were reported to be almost identical.[81] This is reflected by the similarity of the

injection rate constants for these bases. From this qualitative comparison of the hole injection rate constants with the oxidation potentials in solution, it seems that differences in structure and electronic coupling play a minor role.

Comparing the results for A^z, G, and 8BrG in more detail, it can observed that the order of rate constants changes upon introduction of one A:T base pair between donor and acceptor: $k_1(3'\text{-}X^+G) > k_1(3'\text{-}X^+(8BrG)) > k_1(3'\text{-}X^+A^z)$ whereas $k_1(3'\text{-}X^+AA^z) > k_1(3'\text{-}X^+AG) > k_1(3'\text{-}X^+A(8BrG))$. These results cannot be rationalized solely on the basis of changes in the driving force and therefore point to different contributions of the electronic couplings to the hole transfer rates in $3'\text{-}X^+P$ and $3'\text{-}X^+AP$. The electronic matrix element for any donor–acceptor system is sensitive to the relative orientation and distance of the donating and accepting species. In the direct contact systems $3'\text{-}X^+P$ changing the identity of P may perturb the geometry of the X^+ binding site and hence perturb the electronic matrix element for hole transfer. These base-specific perturbations of the acridine binding site are expected to be of minor importance in duplexes $3'\text{-}X^+AP$ since the chromophore is always flanked by two A:T base pairs.

In summary, from the single-step hole injection rate constants in duplex DNA (duplexes $3'\text{-}X^+AP$) the hole accepting properties of purine bases increase in the order A ~ I ~ 2AP < 8BrG ~ G ≤ A^z < Z (Table 7.3). From the comparison with the in vitro oxidation potentials reported for all bases studied in this work it can be concluded that the hierarchy of these potentials seems to be largely conserved upon incorporation of purine bases into duplex DNA.

For the bases A, I, G, A^z, and Z these findings can be compared to experimental and theoretical results. Nakatani et al. have performed chemical yield experiments where two GGG triplets were separated by a TTBTT unit, with B = A, G, A^z or Z.[128] A theoretical analysis of these experiments provides free energies of purine radical cations in DNA in the order $E(TA^+T) > E(TA^{z+}T) \geq E(TG^+T) > E(TZ^+T)$.[92] Additionally, base stacking is expected to lower the oxidation potentials and to exert a leveling effect on the effective oxidation potentials: For example, a G–A energy gap of about 0.2 eV was suggested,[92] which is much smaller than the difference of the respective solution potentials $E_{ox}(A) - E_{ox}(G) \approx 0.45$ eV.[12, 13] Additional evidence for a lowering of the gap between purine nucleobases in DNA was reported by Lewis and coworkers. Based on the dynamics of hole transport from $G^{\bullet+}$ formed via photoinduced hole transfer to a Z separated from $G^{\bullet+}$ by one A:T base pair the Z–G energy gap in DNA was found to be only 0.19 eV, in contrast to the value of 0.3 eV reported for solution.[93]. Such a small energy gap is also in accord with the range of values 0.15–0.30 eV obtained from the fits of the temperature-dependent data in Chapter 6. Recent semiempirical calculations indicate that guanine and 7-deazaadenine have almost identical ionization energies:[72] $IP(A) = 8.53$ eV >

$IP(A^Z)$ = 8.07 eV ~ IP(G) = 8.06 eV > IP(Z) = 7.66 eV. The trend I ~ A > G > Z for the oxidation potentials is also in accord with time-resolved hole transfer studies in DNA. In these experiments either a photoexcited 2-aminopurine[63] or a stilbene derivative[91] served as the hole injector.

Finally, the above discussion suggests that the major consequence of a purine–purine base replacement is a change in the driving force via E_{ox}. The correlation between the ET rates and the in situ oxidation potentials is expected to be supported by measurements of the activation energies for the injection reactions in the duplexes 3′-X^+AP. These experiments are in progress.

7.2 Hole Transfer Across a $(T)_n$ Bridge

In all previous experiments of this work dealing with bridge-mediated hole transfer the hole donating 9-amino-6-chloro-2-methoxyacridine modification and the chosen hole acceptor were separated by one or two adenine bases. In this section, the role of the intervening bridge will be investigated using the duplexes 3′-X^+TZ and 3′-X^+TTZ in which the bridging adenine nucleobases are replaced by thymine. The full sequences of the modified oligonucleotides are shown in Fig. 7.1.

In 3′-X^+TZ the transient absorption features resemble those observed for 3′-X^+AZ (Table 7.4). Hole injection and backward hole shift slow down by approximately a factor of two as compared to 3′-X^+AZ. The dynamics in duplex 3′-X^+TTZ are similar to those in 3′-X^+AAZ. Nanosecond transient absorption spectroscopy shows that the excited state decays with a 15 ns time constant. The product state $X^\bullet$ is not observed, which is indicative of less activation in the back transfer rate constant k_2 as compared to the forward rate constant k_1. From the ratio of rate constants k_1(3′-X^+TZ)/k_1(3′-X^+TTZ) ≈ 4000[1] an apparent decay parameter $\beta > 2$ Å^{-1} can be calculated. This ratio of is slightly larger than that obtained for the system 3′-$X^+(A)_nZ$, which points to either a steeper decrease in electronic couplings or a stronger increase in activation energy with distance. However, in view of the steep overall distance dependence the difference between 3′-$X^+(A)_nZ$ and 3′-$X^+(T)_nZ$ is rather small, namely $\Delta\beta \approx 0.1$–0.3 Å^{-1}.

Changes in the rate constants after replacing A by T might, in principle, be due to both

[1] For 3′-X^+TTZ the excited-state decay time is τ_{ES} = 15 ns, which is close to τ_{ES} = 18 ns for the reference duplex X^+(AT). Assuming an error bar of ±10% for all decay times τ_{ES}, a lower limit for the ratio of the rate constants k_1(3′-X^+TZ)/k_1(3′-X^+TTZ) > 2230 can be obtained from Eq. (4.5), as compared to the upper limit for the duplexes containing bridging adenines with k_1(3′-X^+AZ)/k_1(3′-X^+AAZ) < 1800.

Table 7.4: Excited-state decay times and forward and backward hole transfer rate constants k_1 and k_2 in duplexes 3′-$X^+(B)_{1\text{-}2}Z$ with B = A and T.

Duplex	τ_{ES} [ns]	k_1 [s^{-1}]	k_2 [s^{-1}]
3′-X^+AZ	0.011	9.1×10^{10}	1.0×10^{10}
3′-X^+AAZ	8.4	7.4×10^{7}	-
3′-X^+TZ	0.022	4.5×10^{10}	5.0×10^{9}
3′-X^+TTZ	15	~1.1×10^{7}	-

[a] Forward charge shift rate constants calculated from the excited-state lifetimes according to Eq. (4.5).

changes in the electronic couplings and the increase in energy difference between the initial and the bridge states. Based on the in vitro oxidation potentials (Table 7.2) this injection barrier is about 0.2 eV higher for thymine than for adenine.[12] Such an increase in the injection barrier is expected to lead to a higher β parameter.[75] In contrast, a recent quantum chemical modeling study reports identical values for $(A)_n$ and $(T)_n$ bridges,[72] in agreement with the experimental findings for stilbene-linked DNA hairpins.[66]

The results for the X^+-modified duplexes also suggest a similar decay of the rate constant for superexchange hole transfer mediated by either A or T bases. The observed difference in distance dependence might reflect the change in the injection barrier, different electronic coupling matrix elements for X^+–A and X^+–T, or changes in the activation energy. Whereas it is difficult to assign differences in the hole transfer rates to either the injection barrier or the couplings, the contribution of the activation energy can, in principle, be determined from temperature-dependent measurements, as discussed in Section 6.3.1.

7.3 Interstrand Hole Transfer

The 9-amino-6-chloro-2-methoxyacridine modification and the hole acceptor do not necessarily have to be placed on the same oligonucleotide strand. It is also possible to study hole transfer in duplexes where donor and acceptor are located on different strands. Such interstrand hole transfer was investigated with the duplexes denoted 3′-X^+Z_c and 3′-$X^+A_cZ_c$ (see Fig. 7.1). The coupling between X^+ and Z in this arrangement is strongly dependent on the intercalation depth and the binding geometry of the chromophore.

Placing a C:Z base pair next to X^+, duplex 3′-X^+Z_c, results in transient absorption features almost identical to those observed for 3′-X^+Z and 5′-X^+Z (Fig. 7.5). The product

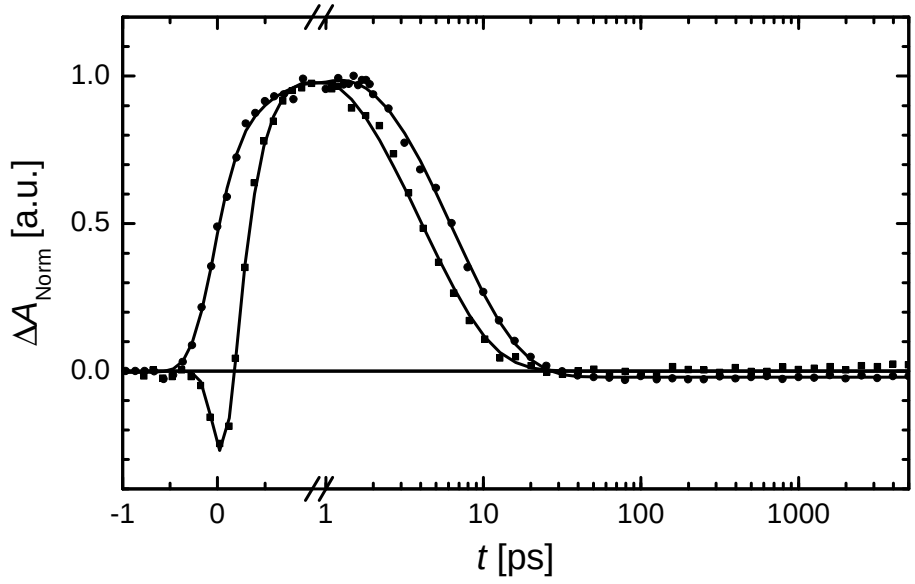

Fig. 7.5: Comparison of the transient kinetics measured in the duplexes 3′-X^+Z_c (■) and 3′-X^+Z (●) using 455 nm pump pulses and 500 nm probe pulses. The solid lines are nonlinear least-squares fits to the kinetic data.

state $X^\bullet$ monitored at 500 nm is formed within ~400 fs and decays with a lifetime of 4.0 ps. Single exponential forward charge shift and back transfer kinetics with negligible background signal are observed in this duplex. With one A:T base pair between the acridine and Z, duplex 3′-$X^+A_cZ_c$, both the forward and backward charge shift times slow down by a factor of about 25 relative to their counterparts in 3′-X^+Z_c. Hole injection and backward hole shift reactions occur with time constants of 12 ps and 90 ps, respectively and are very similar to the time constants observed for intrastrand transfer (Fig. 7.6).

These results point to a deeply intercalated ACMA chromophore, since similar time constants imply comparable donor–acceptor electronic couplings when the hole transfer direction is in either the 5′ or 3′ direction, and when the donor and acceptor are located on complementary strands. This view is consistent with preliminary information from a forthcoming NMR structure, which indicates that the adenine base opposing the acridine chromophore and to a lesser extent also its neighboring bases do not adopt a regular B-form structure.[90] This deviation from the standard DNA structure can be explained by the constraints imposed by the size of the intercalated chromophore, which forces the opposing A base out of its normal position.

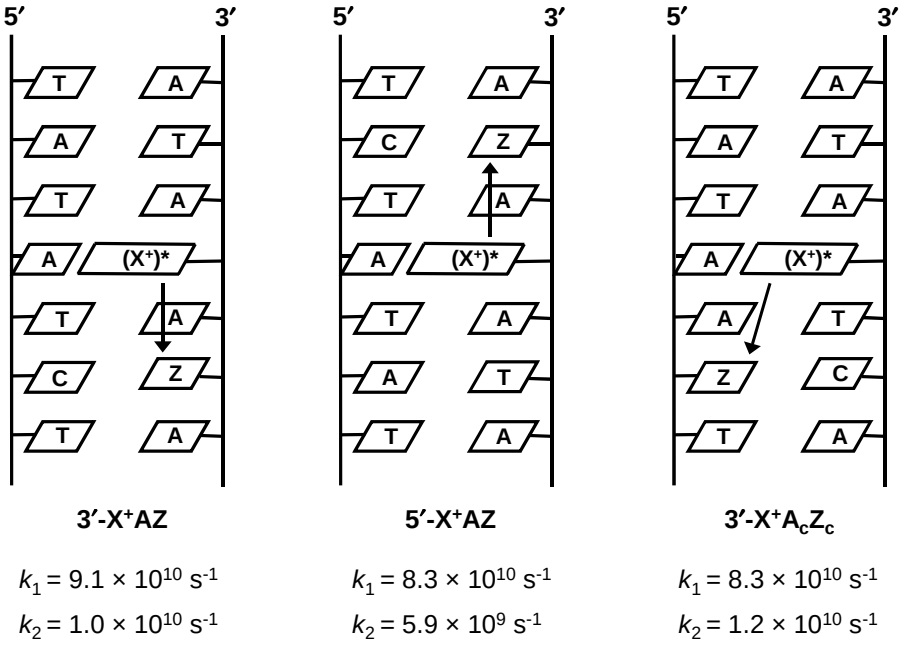

Fig. 7.6: Schematic illustration of intrastrand hole transfer in 3′-X^+AZ and 5′-X^+AZ and interstrand hole transfer in 3′-$X^+A_cZ_c$. Also given are the forward and backward hole transfer rate constants k_1 and k_2 for each duplex. Whereas all three duplexes are 21 base pairs long (see Figs. 4.2 and 7.1) for clarity only the proximity of the chromophore is shown.

7.4 Cooperative Effects of Adjacent Bases

The results of the experiments in the preceding chapters and sections could be well described as hole transfer from a photoexcited donor to a localized acceptor nucleobase separated by a number of inert bridging nucleobases. However, in view of the strong stacking interactions in DNA, it has to be taken into account that the ET parameters for hole transfer to a specific nucleobase acting as a hole acceptor may be sensitive to the nucleobase environment. Ab initio and semi-empirical calculations suggest that the energy of an oxidized base B^+ in DNA is influenced considerably by the chemical identity of the adjacent bases.[129, 130] In the following, the dependence of hole transfer to a base B on its adjacent bases will be summarized using results from this work and other studies. The sequences of the X^+-modified strands discussed in this section are given in Fig. 7.7.

X^+ABA. The hole transfer processes in X^+-modified DNA duplexes, presented in Chapter 4, can be explained by a single-step hole transfer from photoexcited X^+ to nucleobases B in the triplet ABA, where B = G, Z. The bridging adenine bases act as

3′-X⁺AG	5′-GCG TTA T	**AG A(X⁺)A**	TAA TAT GCG-3′
3′-X⁺AZ	5′-GCG TTA T	**AZ A(X⁺)A**	TAA TAT GCG-3′
3′-X⁺AP	5′-GCG TTA T	**AP A(X⁺)A**	TAA TAT GCG-3′
3′-X⁺TZ	5′-GCG TTA A	**AZ T(X⁺)A**	TAA TAT GCG-3′
3′-X⁺AGG	5′-GCG TTA T	**GG A(X⁺)A**	TAA TAT GCG-3′
5′-X⁺AG	5′-GCG TTA TAT	**A(X⁺)A GA**	T TAT GCG-3′
5′-X⁺AZ	5′-GCG TTA TAT	**A(X⁺)A ZA**	T TAT GCG-3′

Fig. 7.7: Nucleobase sequences of the X^+-modified single strands used to produce the duplexes discussed in Section 7.4, with P = I, A^z, 2AP, and 8BrG. The counter strands are not shown, however, all nucleobases were placed in a standard Watson–Crick pair and an adenine was placed opposite to X^+.

superexchange mediators. This result can be extended to other modified purine nucleobase analogs. As discussed in Section 7.1, in the duplexes 3′-X⁺AP (with P = A, I, 2AP, 8BrG, G, Z, and A^z), the hierarchy of the oxidation potentials seems to be largely conserved upon incorporation of the different nucleobases B into duplex DNA. In addition, the changes in the rates go along with a change in the driving force which is expected from the calculated ionization energies of the bases.[72] This qualitative comparison suggests that changes in electronic couplings upon the replacement of a purine nucleobase, that are due to structural effects or specific interactions with the adjacent adenines, play a minor role.

X⁺(A, T)B(A, T). As discussed in Section 7.2, changing the base that constitutes the superexchange bridge element in the sequence 3′-X⁺AZ to 3′-X⁺TZ is expected to influence the couplings and the injection barrier. In both cases, the 5′ subsequent base is an A (Fig. 7.7). Additionally, the energy of the oxidation potential of Z might be influenced by the adenine–thymine replacement. However, the hole transfer rate constants observed in 3′-X⁺AZ and 3′-X⁺TZ differ only by a factor of about two and thus point to a small overall effect. This finding is in accord with transient absorption measurements on stilbene-linked DNA hairpins with either TGT or AGA motifs.[66] However, semi-empirical calculations suggest that in 5′-(A, T)G⁺(A, T)-3′ triplet ions the stabilization of G^+ is influenced considerably by the 3′-(A, T) base, whereas the effect of the preceding base 5′-(A, T) was found to be rather small.[130] 5′-AG⁺A-3′, for example, was calculated to be more stable than 5′-TG⁺T-3′ by about 0.15 eV. These calculations cannot be compared directly to the above experiments since it is not easy to experimentally disentangle the contributions of

the electronic couplings and the energetics. More experiments with selective A–T replacements are needed to resolve the discrepancy between the rather large calculated stabilization energies and the small effects on the experimental rates.

X^+AGG(A, G). From extensive photocleavage studies it is known that GG sequences are more reactive than GA sequences. Even greater selectivity is observed for cleavage at GGG sequences.[128] The basis for this selectivity has been investigated computationally and it has been proposed that these observations are due to a lower oxidation potential of G in GG and GGG sequences.[129] Such a lowering of the oxidation potential is expected to alter the driving force and, for a hole transfer in the normal region, lead to an increase in the rate constant. Experiments in either X^+-labeled duplexes or stilbene-linked hairpins reported only small changes in the observed hole transfer rates.[131, 132] For the duplex 3′-X^+AGG, for instance, the hole injection rate constant is $k_1 = 1.7 \times 10^8$ s^{-1}[131] in comparison to $k_1 = 8.9 \times 10^7$ s^{-1} for 3′-X^+AG (Chapter 4). In contrast, recent semi-empirical calculations predict stabilization energies of 0.13–0.3 eV for $(GG)^{\bullet+}$ and $(GGG)^{\bullet+}$ relative to $G^{\bullet+}$.[130] The difference between theory and experiment may be rationalized by the fact that the calculated results refer to model duplexes in vacuum and do not incorporate solvation effects. Recent analyses of experimental data yield lower values for the stabilization energies. Bixon and Jortner analyzed the chemical yield experiments by Meggers et al.[61] and concluded that in these duplexes the free energy gap between $(GGG)^{\bullet+}$ and $G^{\bullet+}$ is only 0.062–0.096 eV.[133] Lewis et al. investigated the dynamics of hole transport from $G^{\bullet+}$ formed via photoinduced hole transfer from photoexcited stilbene to a GG or GGG sequence separated from $G^{\bullet+}$ by one A:T base pair.[132] From kinetic modeling of the delayed decay of the stilbene anion radical free energy differences were derived: GG is only 0.052 eV lower in energy than G, and GGG is only 0.077 eV lower. These results point to GG and GGG being shallow hole traps in duplex DNA.

The experimental charge transfer rates indicate that the hole-accepting site is the G nucleobase proximate to the injector.[131] The sequence selectivity observed in oxidative strand cleavage experiments, indicating that in GGG either the 5′- or central G is the preferred cleavage site,[134, 135] may be achieved by either an intraguanine tract relaxation process subsequent to the primary oxidation kinetics[131] or by a delocalization of the hole over the GG or GGG sequence. Lewis et al. suggested that the rather small effects of neighboring bases upon the dynamics and equilibria for charge transfer[66, 131, 132] and charge transport[132] processes indicate that hole delocalization occurs only to a limited degree in DNA. This view is consistent with the simple hopping model for charge transport in DNA[11, 59] and does not require the involvement of extensively delocalized polarons.[56]

8 Ultrafast Electron Transfer in the Complex Between Fluorescein and an Engineered Lipocalin Protein

Whereas the last chapters focused on details of charge transfer processes in DNA, this chapter investigates the mechanism responsible for the strong fluorescence quenching in the complex between the pigment molecule fluorescein and an engineered protein.[25]

Anticalins are small antibody-like proteins with prescribed ligand specificities derived from the lipocalin scaffold. Skerra and coworkers demonstrated that the ligand pocket of a lipocalin from *Pieris brassicae*, the bilin-binding protein, can be reshaped by combinatorial protein design such that it recognizes fluorescein, an established immunological hapten.[25] The anticalin FluA complexes fluorescein with high affinity, exhibiting a dissociation constant as low as $K_D = 35.2 \pm 3.2$ nM. In contrast to other cognate anticalins this protein effects almost complete quenching of the ligand fluorescence upon complexation ($Q_{max} = 99.7 \pm 0.3\%$).

In this chapter the underlying mechanism of this fluorescence quenching will be investigated with femtosecond transient absorption spectroscopy. The preparation of the protein samples is described in Section 2.3.2. The anticalin protein FluA was provided by A. Skerra (Lehrstuhl für Biologische Chemie, Technische Universität München).

8.1 Results

8.1.1 Steady-State Spectroscopy of Free and Protein-Bound Fluorescein

Steady-state absorption, fluorescence, and fluorescence excitation spectra of free fluorescein and of fluorescein bound to the anticalin (FluA·Fl) are compared in Fig. 8.1, both in aqueous buffer solution at pH 8.0. The fluorescence was excited at 490 nm and fluorescence excitation was probed at 540 nm. The maxima of both spectra are normalized with respect to the absorption peak at 490 nm. In Fig. 8.1a the shape and peak position of the intense absorption band at 490 nm are typical of fluorescein in its dianionic state (Fl^{2-}), which is the predominant protolytic form at pH 8.0.[136, 137] The pK_a value for protonation is 6.3. This absorption band corresponds to the π–π^* transition of the xanthene ring. The

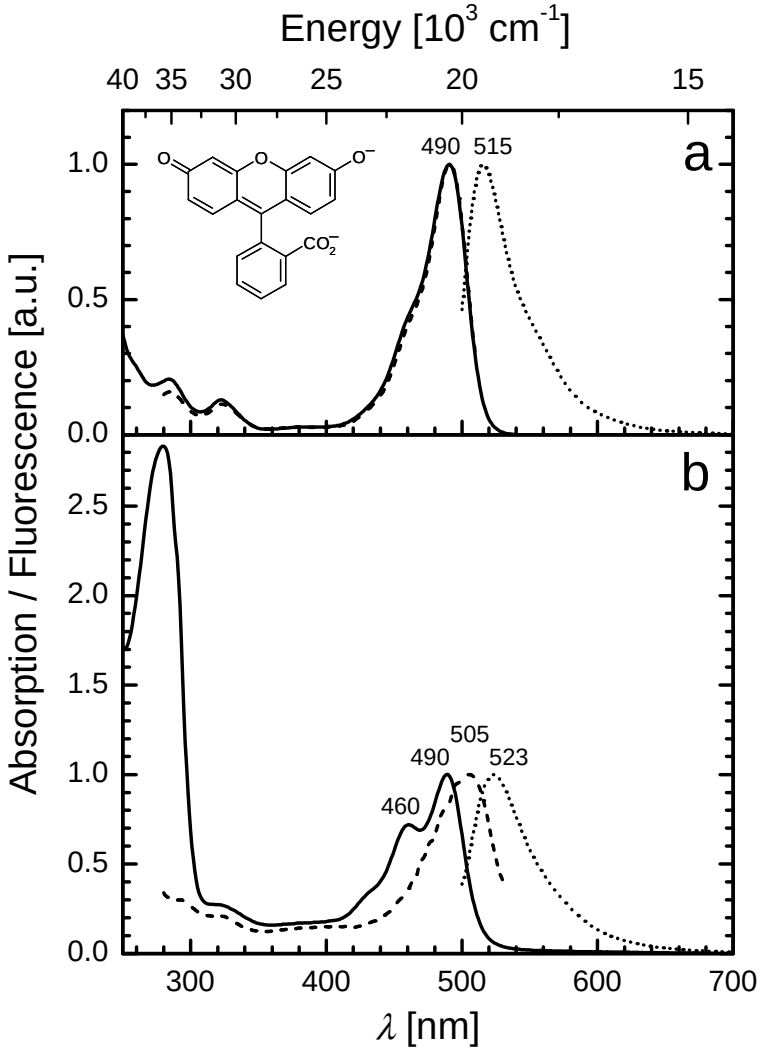

Fig. 8.1: Normalized steady-state absorption (—), fluorescence (·····), and fluorescence excitation (---) spectra of (a) free fluorescein and (b) FluA·Fl both in buffer, pH 8.0, at T = 295 K. Fluorescence was excited at 490 nm and fluorescence excitation was probed at 540 nm. Inset: Chemical structure of the fluorescein dianion.

shoulder at about 460–475 nm has been attributed to the $1 \leftarrow 0$ transition of the totally symmetric ring breathing mode.[138] In the FluA·Fl complex this shoulder develops into a pronounced peak at 460 nm, whereas the weak absorption band at shorter wavelengths around 323 nm seems to be independent of the complexation.

The similarity of the two absorption spectra in Fig. 8.1 suggests that fluorescein is bound to the protein in its dianionic state. The appearance of a pronounced vibronic band progression with a typical energy separation of about 1330 cm^{-1} reflects a reduction in the degrees of freedom, which is typical of a tight-binding situation. In FluA·Fl the UV band at 283 nm of the ligand is superimposed by the intense absorption of the protein, which predominantly arises from the aromatic side chains of tryptophan (Trp) and tyrosine (Tyr).

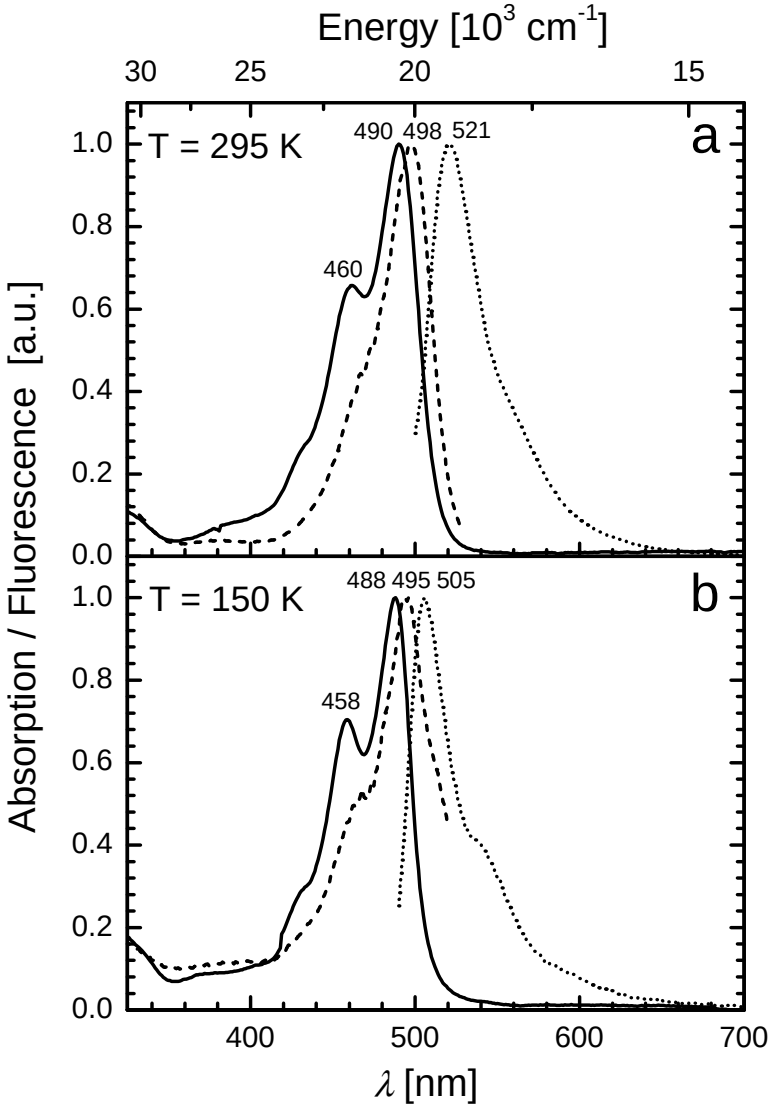

Fig. 8.2: Normalized steady-state absorption (—), fluorescence (·····), and fluorescence excitation (---) spectra of FluA·Fl in 60% glycerol/buffer, pH 8.0, at 295 K (a) and 150 K (b). The fluorescence was excited at 490 nm for T = 295 K, and at 480 nm for T = 150 K. The fluorescence excitation was probed at 540 nm for both temperatures.

Regardless of the excitation wavelength, the fluorescence spectrum of FluA·Fl is red-shifted as compared to the free chromophore in solution (Fig. 8.1a). In addition, the fluorescence excitation spectrum of FluA·Fl does not follow the absorption spectrum. It is red-shifted by 15 nm and both the vibronic shoulder at 460 nm and the protein peak at 280 nm are missing. This dramatic shift implies that the fluorescence of the majority population of the bound fluorescein is quenched and only a small subpopulation is responsible for the fluorescence. The fluorescence excitation spectrum with its peak at 505 nm is characteristic of the absorption spectrum of this subpopulation. The intensity of

this minority emission is within the previously published fraction of about 0.3%.[25] Moreover, this subpopulation of bound fluorescein cannot be excited in the protein absorption band at 280 nm, as shown in Fig. 8.1b. This points to the absence of energy transfer from aromatic amino acids due to a larger distance and/or an unfavorable geometry. This minority population is characterized by a Stokes shift of 680 cm^{-1}, which reflects its complexation by the protein since it is by 310 cm^{-1} smaller than the one measured for the free chromophore.

To gain insight into the fluorescence quenching mechanism, steady-state and time-resolved measurements at low temperatures are useful, even though they require the presence of a cryoprotector. The experimental conditions of a glassy matrix that are necessary for low temperature absorption studies were met with an aqueous protein solution containing 60% glycerol. As shown in Fig. 8.2a, the effect of glycerol on the absorption and fluorescence spectra of FluA·Fl at room temperature is negligible. This is not the case for the excitation spectrum, which is blue-shifted by 6–7 nm. If the fluorescence excitation spectrum is again attributed to the absorption of a less-quenched minority population, it becomes obvious that the addition of glycerol leads to an increase in the fluorescing minority population. This effect is consistent with a pronounced gain in the overall fluorescence intensity that was observed in these steady-state measurements.

An analogous set of spectra was recorded at lower temperatures ranging from 295 K to 90 K. The spectra in Fig. 8.2b, taken at 150 K, are representative for low temperatures since further cooling had no effect. At low temperatures the shoulder in the red wing of the fluorescence spectrum gains intensity. At the same time the appearance of a more pronounced vibronic structure and a narrowing of the absorption bands can be observed. The peak position of the absorption band remains grossly unchanged, whereas the maximum of the fluorescence band shifts by 15 nm to the blue. In contrast to room temperature (Fig. 8.2a), where the excitation spectra were invariant when probed in the maximum or in the red wing of the fluorescence band, this was not the case at low temperatures. When probed at, for example, 540 nm or 560 nm the peak position of the fluorescence excitation spectrum shifted from 495 nm to 501 nm, respectively. This effect is probably due to a loss of structural definition of the fluorescein binding site induced by glycerol, which leads to an increased spectral dispersion and lowers the probability of fluorescence quenching.

8.1.2 Femtosecond Transient Absorption Spectroscopy

FluA·Fl in Aqueous Buffer at 295 K

The protein-fluorescein complex was excited in its absorption peak at 495 nm. The temporal evolution of the resulting species was probed in specific spectral regions in order to follow the excited-state dynamics and the ground-state recovery of Fl^{2-} and to monitor the rise and decay of potential product states that may evolve after photoexcitation.

The initially excited state $^1(Fl^{2-})^*$ was probed in the stimulated emission region at 550 nm (Fig. 8.3a). This wavelength in the red wing of the fluorescence band has been chosen in order to minimize contributions of ground-state absorption. The stimulated emission decays almost monoexponentially with a time constant of τ_1 = 420 fs (92%) (Table 8.1). This time constant for the decay of the excited fluorescein dianion $^1(Fl^{2-})^*$ in the protein pocket, τ_{ES}, is by four orders of magnitude faster than the known decay time of 4.1 ns of the dianion in aqueous solution (τ_F).[137]

$$\frac{\Phi_0}{\Phi} = 1 + \frac{\tau_F}{\tau_{ES}} \tag{8.1}$$

Using the fluorescence quantum yield of the fluorescein dianion of $\Phi_0 = 0.93$,[26] Eq. (8.1) results in a value of $\Phi = 1 \times 10^{-4}$ for the fluorescence quantum yield of FluA·Fl, which is in agreement with the previous fluorescence quenching value of $99.7 \pm 0.3\%$ from comparative steady-state measurements.[25] The central question arising from this observation of an ultrashort-lived excited state addresses the mechanism of the quenching process. In particular, it has to be studied whether the ultrafast decay of $^1(Fl^{2-})^*$ leads to the formation of a defined product.

In order to elucidate the mechanism underlying the ultrafast quenching of the fluorescein excited state probing at 390 nm is of great interest since the products of a potential charge transfer process can be detected at this wavelength. When monitoring the absorbance at 390 nm, an instant rise followed by three decay components is observed (Fig. 8.3b): τ_1 = 430 fs (28%), τ_2 = 3.4 ps (61%) and τ_3 = 49 ps (11%). The subpicosecond component τ_1 is very similar to the time constant found for stimulated emission. Therefore, it can be concluded that this component reflects the decay of the fluorescein excited state $^1(Fl^{2-})^*$, which is known to absorb at this specific wavelength.[139] The main component τ_2 is probably due to a product state that is formed after photoexcitation. More specifically, the one-electron redox states of the fluorescein dianion, $(Fl^{1-})^\bullet$ and $(Fl^{3-})^\bullet$, were reported to have absorptions at 390 nm.[139, 140] This suggests photoinduced electron transfer, involving either oxidation or reduction of the fluorescein dianion, as a probable mechanism of the

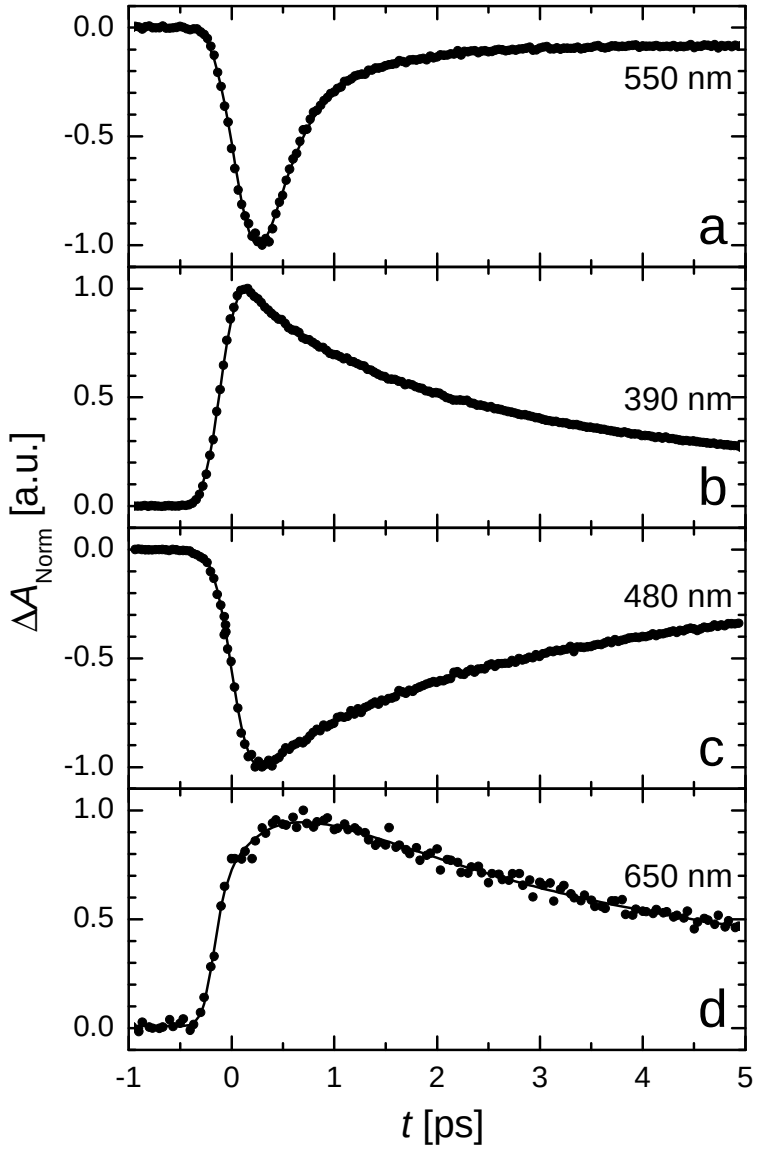

Fig. 8.3: Transient pump-probe kinetics measured in FluA·Fl using 495 nm, ~200 fs pump pulses. The probe wavelength used for each kinetic trace is noted in (a)–(d). The solid lines are nonlinear least-squares fits, whose parameters are listed in Table 8.1.

observed fluorescence quenching.

Unfortunately, the extinction coefficients of $^1(Fl^{2-})^*$, $(Fl^{1-})^\bullet$, and $(Fl^{3-})^\bullet$ are of similar magnitude in this wavelength region.[139, 140] The fact that upon probing at 390 nm no femtosecond rise component corresponding to the formation kinetics of the product state is observed, indicates that the extinction coefficient ε_{390} of $^1(Fl^{2-})^*$ is larger than ε_{390} of $^1(Fl^{3-})^\bullet$ or ε_{390} of $(Fl^{1-})^\bullet$, thus masking the rise dynamics.

Table 8.1. Numerical parameters of the fit functions displayed in Fig. 8.3 for the different spectral regions of probing (λ_{probe}).

λ_{probe} [nm]	ΔA_1	τ_1 [ps]	ΔA_2	τ_2 [ps]	ΔA_3	τ_3 [ps]
550	–0.93	0.42	-	-	–0.07	60
650	–0.57	0.45	0.76	3.1	0.24	37
480	–0.24	0.52	–0.67	4.0	–0.09	42
390	0.28	0.43	0.61	3.4	0.11	49

$\Delta A_{1,2,3}$ are the relative amplitudes of the time constants $\tau_{1,2,3}$. The short time constants τ_1 have been determined within the time window of 5 ps as depicted in the figure. The longer time constants τ_2 and τ_3 have been fitted using the full time window of 5 ns.

The recovery of the ground-state absorption of (Fl^{2-}) was probed at 480 nm (Fig. 8.3c), i.e., in the blue wing of the main absorption band (Fig. 8.1) in order to eliminate contributions from stimulated emission. In fact, the dominant component, with τ_2 = 4.0 ps (67%), resembles the decay of the product state observed above. Therefore, already at this stage a three-level reaction cycle may be postulated (Fig. 8.4). The ultrafast component in this recovery pattern with a time constant τ_1 = 520 fs (24%) is similar to the one observed when probing the stimulated emission at 550 nm. The origin of this component has not yet been fully understood. It may be due to a potential contribution of radical absorption to the observed signal. Similarly to the time traces monitored at 550 nm and 650 nm the recovery pattern contains a small slower component τ_3 = 42 ps.

A potential product of the quenching process was probed at 650 nm (Fig. 8.3d). At this wavelength, a rise component evolves with a time constant of τ_1 = 450 fs, which is similar to the one observed for the stimulated emission at 550 nm. The subsequent decay can be fitted with two exponentials. The time constant of the main component, τ_2 = 3.1 ps, is in accord with the ground-state recovery time. This absorption is probably due to a fluorescein radical ($(Fl^{1-})^{\bullet}$ or $(Fl^{3-})^{\bullet}$). The fact that no assignment for this absorption band could be found in the literature may be due to its low extinction coefficient.[1]

At all probing wavelengths the contribution of the fluorescing minority appeared to be negligible since the kinetics did not depend on the excitation wavelength in the blue wing of the absorption band (475 nm or 455 nm) where the contribution of the minority should vary drastically according to its excitation spectrum depicted in Fig. 8.1. This finding provides strong evidence against the co-existence of different prototropic forms in the

[1] $\Delta A_{max}(\lambda_{probe}$ = 390 nm) ≈ 50 $\Delta A_{max}(\lambda_{probe}$ = 650 nm). However, changes in the setup, e.g. in the pump-probe overlap at the different probe wavelengths, may also contribute to the observed factor of 50.

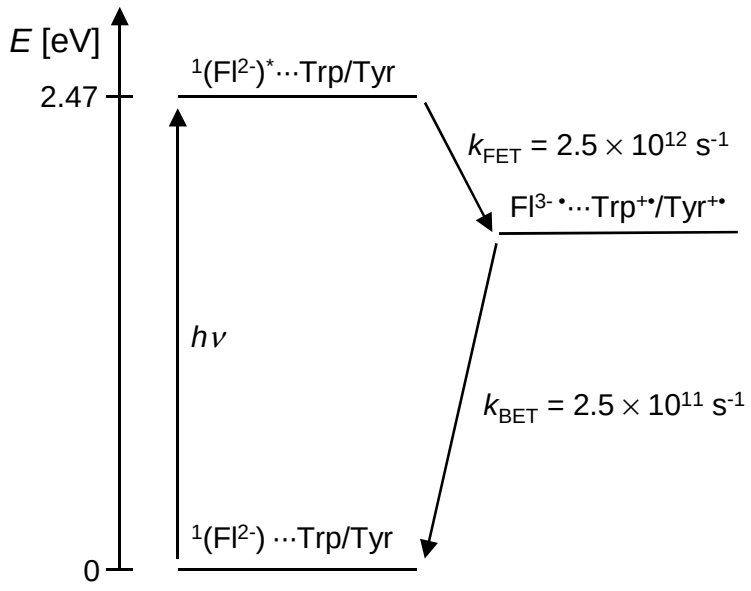

Fig. 8.4: Kinetic scheme proposed for the mechanism of fluorescence quenching in FluA·Fl. The experimental results did not allow a discrimination between the potential electron donors tryptophan (Trp) and tyrosine (Tyr) (Section 8.2.1).

protein.[136] Since the fluorescein dianion $^1(Fl^{2-})^*$ does not carry a proton with increased acidity, the independence of the observed kinetics from the excitation wavelength is also evidence against an excited-state proton transfer.

Additionally, with respect to the quenching mechanism depicted in Fig. 8.4, a variety of processes may be excluded, as e.g. ultrafast internal conversion, irreversible photochemical bond splitting, and, considering the femtosecond time scale, also intersystem crossing. Hence, the excited-state reaction cycle is postulated to be initiated by an ultrafast ET, involving either oxidation or reduction of the fluorescein dianion. Since the absorption bands of both possible products at 390 nm are superimposed with similar extinction coefficients,[139] the redox process per se can be followed, even though its direction cannot be determined directly from the measurements.

FluA·Fl in a Buffer/Glycerol Glass Matrix

Figure 8.5 compares stimulated emission signals of FluA·Fl probed at 550 nm under different conditions: in aqueous buffer (1) as well as in a 60% glycerol/buffer mixture at 295 K (2) and at 150 K (3). In the presence of glycerol the decay of the excited state at high and low temperatures is multiexponential and must be fitted with at least three time components in order to obtain a satisfying fit, the shortest being τ = 420 fs (93%) at 295 K

and $\tau = 370$ fs (65%) at 150 K. Thus the value of the shortest component is almost identical in all three cases, indicating a temperature-independent quenching process for the majority population of FluA·Fl.

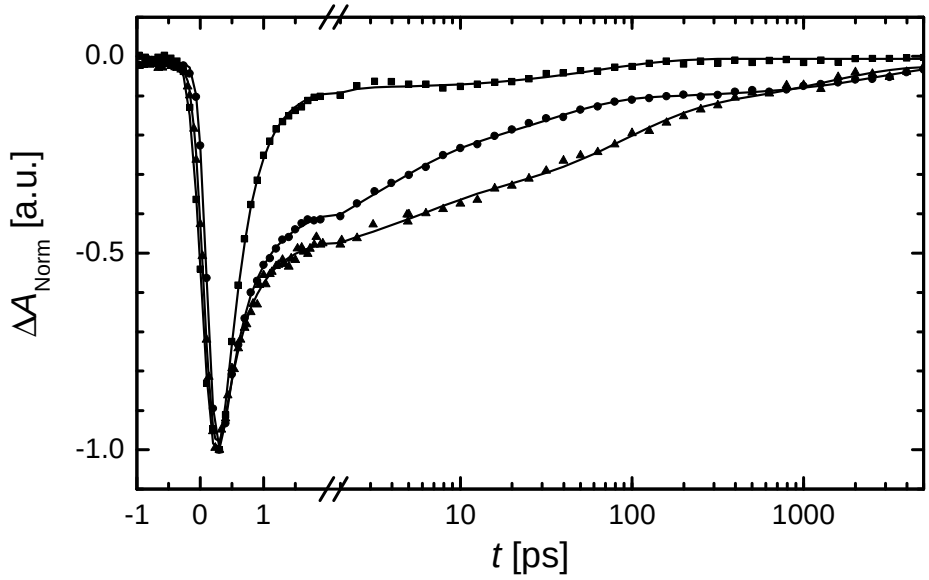

Fig. 8.5: Transient pump-probe kinetics measured in FluA·Fl using 495 nm, ~250 fs pump pulses and 550 nm probe pulses. (■) In aqueous buffer, pH 8.0, at T = 295 K, (•) in 60% glycerol/buffer, pH 8.0, at T = 295 K, and (▲) in 60% glycerol/buffer, pH 8.0, T = 150 K. The solid lines are nonlinear least-squares fits whose parameters are listed in Table 8.2.

Table 8.2.: Numerical parameters of the fit functions displayed in Fig. 8.5.

T [K]	ΔA_1	τ_1 [ps]	ΔA_2	τ_2 [ps]	ΔA_3	τ_3 [ps]	ΔA_4	τ_4 [ps]
295[a]	–0.93	0.42	-	-	–0.07	60	-	-
295[b]	–0.66	0.35	–0.17	3.3	–0.17	32	–0.11	2900
150[b]	–0.65	0.37	–0.11	5.0	–0.16	87	–0.08	1300

$\Delta A_{1,2,3,4}$ are the relative amplitudes of the time constants $\tau_{1,2,3,4}$. [a] FluA·Fl in aqueous buffer, pH 8.0. [b] FluA·Fl in 60% glycerol/buffer mixture, pH 8.0.

8.2 Discussion

8.2.1 Mechanism of Fluorescence Quenching in FluA·Fl

The key feature of the quenching kinetics of the protein-bound fluorescein is its excited-state electron transfer within 400 fs, forming an intermediate radical ion pair, which recombines within 4 ps (Fig. 8.4). Notably, the excited-state lifetime, and thus the primary ET rate, is monoexponential, which points to a highly defined binding site.

The most probable partner for the excited fluorescein dianion to undergo electron transfer is a nearby aromatic amino acid with an appropriate redox potential. Trp and Tyr residues are suitable candidates since their own fluorescence has been shown to be quenched upon excitation at 280 nm when titrating FluA with variable amounts of fluorescein.[25] The potency of Trp and Tyr as quenchers of excited fluorescein has also been discussed in the context of other spectroscopic assays. Screening of individual L-amino acids for the ability to quench fluorescein fluorescence in neutral aqueous solution resulted in the finding that L-Trp and, to a lesser degree, L-Tyr are effective quenchers.[28] Steady-state fluorescence quenching has also been observed in anti-fluorescein monoclonal antibodies like 4-4-20,[141] whose combining sites are rich in Trp and Tyr residues and which are functionally related to the FluA·Fl complex. FluA contains 15 Tyr and 6 Trp residues (plus a further Trp as part of the *Strep*-tag). Several of the Trp side chains are located close to the bound fluorescein within the β-barrel structure.

The feasibility and direction of excited-state electron transfer with respect to the change in free energy can be tested using the Rehm-Weller expression (Eq. 3.5). The Coulombic term is difficult to estimate as the donor–acceptor distance and orientation as well as the local dielectric constant are unknown. Therefore, it will be neglected in the following estimates on the directionality of the forward electron transfer.

The redox potentials are taken from electrochemical data. At pH 7.0, the oxidation potential of Tyr in aqueous solution is $E^0[Tyr^{+\bullet}/Tyr] = 0.66$ V (SCE).[142] It becomes less positive at increasing pH, thereby facilitating forward electron transfer (FET), e.g. $E^0[Tyr^{+\bullet}/Tyr] = 0.58$ V (SCE) at pH 8.0. The analogous oxidation potentials for Trp at neutral pH and pH 8.0 are $E^0[Trp^{+\bullet}/Trp] = 0.75$ V (SCE) and $E^0[Trp^{+\bullet}/Trp] = 0.69$ V (SCE), respectively.[142] The reduction potential of the fluorescein dianion is $E^0[Fl^{2-}/Fl^{3-\bullet}] = -1.19$ V (SCE),[143] and its $S_{1,0} \leftarrow S_{0,0}$ excitation energy is 2.47 eV.

Under the assumptions that within the binding pocket the difference in redox potentials is maintained the driving force for the electron transfer involving Trp and Tyr is $\Delta G_{FET} = -0.59$ eV and $\Delta G_{FET} = -0.7$ eV, respectively. These ΔG values clearly indicate the energetically favorable direction of photoinduced charge transfer either from Trp or from

Tyr to the fluorescein dianion.[2] In analogy to the ET processes in DNA discussed in the previous chapters, the chromophore acts as electron acceptor (hole donor) in its photoexcited state. Accordingly, the driving force for the back charge transfer (BET) repopulating the ground states of the fluorescein dianion and the neutral Trp and Tyr residues may be deduced as $\Delta G_{BET} = -1.88$ eV and $\Delta G_{BET} = -1.77$ eV for Trp and Tyr as the respective electron donors.

Although there seems to exist a sufficiently negative driving force for photoinduced hole transfer to the fluorescein excited state, its probability is determined by the relation between driving force and reorganization energy for given electronic couplings, as expressed in conventional ET theory. The following analysis will be based on the nonadiabatic quantum mechanical approach (Eq. 3.7), employing an averaged molecular mode with a frequency of 1500 cm^{-1} (Chapter 3).

For a (nearly) barrierless forward electron transfer, as concluded from the ultrafast rate constant of 1/400 fs, λ_s can be assumed to be approximately equal to $-\Delta G_{FET}$ or slightly smaller. The activationless nature of this rate is also supported by the temperature-dependent measurements (Fig. 8.5) where the ultrafast kinetic component is shown to be temperature independent within the accuracy of the experiments. Assuming that neither energetic nor structural parameters are grossly affected by cooling, this result is consistent with both an activationless or a weakly inverted k_{FET} rate.[48]

Using Eq. (3.7) for an estimate of the parameters λ_v and V and basing this estimate on the room temperature forward and backward rate constants, $k_{FET} = 1/400$ fs and $k_{BET} = 1/4$ ps and on the assumption of activationless electron transfer the resulting values for the electronic coupling and the molecular reorganization energy are $V = 170$ cm^{-1} (140 cm^{-1}) and $\lambda_v = 0.42$ eV (0.32 eV) for Trp (Tyr). Since the contribution of the Coulomb term to the driving force has been neglected these values have to be regarded as first estimates. Qualitatively the binding pocket might be best characterized by strong π–π interactions between the xanthene ring and a nearby Trp (Tyr) residue on the one hand, and by local electrostatic interactions between the negatively charged xanthene ring and charged or dipolar species (e.g. local water molecules and charged or dipolar amino acid residues) on the other hand.

The crude parameter set proposed for activationless charge transfer in the FluA·Fl system comprising $-\Delta G \approx 0.6$–0.8 eV, $\lambda_v \approx 0.3$–0.4 eV, and $V \approx 140$–170 cm^{-1} seems to be reasonable. Some analogy might even exist between FluA·Fl and cyclophane-bridged

[2] It is difficult to provide spectroscopic evidence for Trp and Tyr radical cations. Their absorptions in the 500 nm to 550 nm region[144] have low extinction coefficients (e.g. for $Trp^{\bullet}$ $\varepsilon \approx 2000$ M^{-1} cm^{-1} at $\lambda_{max} = 510$ nm[145]) and coincide with the strong ground-state bleaching signal of the fluorescein dianion as well as with its stimulated emission.

porphyrin-quinone systems in solution.[146] In the latter systems, where donor and acceptor are coplanar and in van der Waals contact, similar electron transfer rate constants in the range of 5×10^{12} s^{-1} were observed. These rates were independent of the polarity of the solution and fitted within the framework of Eq. (3.7) to $\lambda_v \approx 0.54$ eV and $V \approx 140$ cm^{-1}. In fact, a recent X-ray study confirms the structural analogy between the two D–A systems. In FluA·Fl the aromatic amino acid side chain of a tryptophan residue and the xanthene ring of the chromophore are coplanar with a center-to-center distance of about 3.5 Å.[147]

In contrast to the forward electron transfer, the large driving force associated with the back transfer implies that k_{BET} is deeply buried in the Marcus inverted region ($-\Delta G > \lambda_s$) and therefore slower (roughly by a factor of 10) as compared to k_{FET}. On the basis of electron transfer theory this rate constant should be weakly activated. Indeed, at low temperatures the average of slow components with lifetimes of ~8 ps at 295 K extends into the 20 ps range, which is consistent with this expectation.

8.2.2 Characterization of the Fluorescing Minority

As shown in Table 8.1, a 40–60 ps component appears in all spectral regions, indicating that such long components are common to both forward and back electron transfer processes. Although the contribution of this component to the overall kinetics is small with a relative amplitude of about 10%, it should be emphasized that it is this minority with its longer lifetime, which is mainly responsible for the low yield steady-state fluorescence shown in Fig. 8.1. In spite of the large amplitude (93%) of the 400 fs component of the stimulated emission its contribution to the steady-state fluorescence is at least by one order of magnitude smaller than the one of the 40–60 ps component. The spectral fingerprints of this fluorescing minority in FluA·Fl are the red-shifted fluorescence excitation spectrum (and correspondingly its characteristic absorption spectrum) and the relatively small Stokes shift of 680 cm^{-1}.

Similar features have been reported for fluorescein bound to antibodies, e.g. to the monoclonal anti-fluorescein antibody 4-4-20.[148, 149] However, in contrast to FluA·Fl, measurements on different antibody systems revealed a pronounced red shift of the whole fluorescein absorption band ranging from 498 to 520 nm.[149-153] This red shift in absorption has previously been postulated as the fingerprint of antibody-bound fluorescein. The results presented for FluA·Fl do not support this conclusion as a general rule since the long-wavelength maxima of the absorption spectra in Fig. 8.1 coincide. Instead, a comparison of both protein-ligand systems indicates that a red-shifted absorption spectrum neither correlates with the fluorescence quenching efficiency nor with the thermodynamic affinity for the fluorescein dianion.

8.3 Conclusions

Femtosecond absorption spectroscopy applied to FluA·Fl revealed that excited-state electron transfer is responsible for the strong fluorescence quenching effect. On the basis of redox potentials either a tryptophan or tyrosine residue may serve as electron donor to the bound fluorescein in its excited singlet state, thus leading to the formation of the fluorescein trianion radical on the 400 fs time scale. This short time represents one of the fastest electron transfer reactions resolved in a protein at physiological temperature so far. In fact, this electron transfer time is by a factor 3–4 faster than the fastest step in photosynthesis at ambient temperature.[154] For comparison, in the bacterial reaction center of *Rh. sphaeroides* electron transfer from reduced bacteriochlorophyll to bacteriopheophytin proceeds with a time constant of ~1–2 ps.[4]

As excited-state quenching via electron transfer depends in a most sensitive way on the electronic interaction between the electron donor and acceptor, these processes are easily affected by structural changes involving the donor–acceptor species and their environment. Thus, unless complex compensation effects among the different parameters in electron transfer theory play a role, the almost monoexponential ultrafast decay kinetics of the excited fluorescein dianion that is observed for FluA·Fl points to a single, well-defined binding site.

On the basis of conventional electron transfer theory globally applied to both fast, activationless forward and slower back ET rate constants the electronic interaction involved in the charge transfer process is estimated to be ~170 cm^{-1} (~140 cm^{-1}) in the case of Trp (Tyr) assuming a polar environment, i.e., electrostatic screening of the Coulomb interaction. This large electronic interaction indicates a favorable geometry and a short distance between the electron donor, tryptophan or tyrosine, and the acceptor.

The weak steady-state fluorescence is due to a 10% minority of FluA·Fl, which is characterized by its red-shifted absorption spectrum as reflected in the fluorescence excitation spectrum and by its excited-state lifetime of 40–60 ps.

9 Summary

The dynamics of photoinduced charge transfer processes in modified DNA duplexes and a protein-fluorescein complex have been investigated by means of femtosecond time-resolved absorption spectroscopy. The results demonstrate the power of this method for the elucidation of excited-state quenching mechanisms in complex biological systems.

Modified DNA Duplexes

The charge shift dynamics in DNA have been investigated in 21-base-pair duplexes with specific sequences containing a covalently attached protonated 9-amino-6-chloro-2-methoxyacridine (X^+) chromophore. This acridine derivative resides in the DNA duplex at an artificial abasic site, which seems to be highly defined, as concluded from the monoexponentiality of the kinetics. By monitoring the three observables (1) the decay of the excited singlet state $^1(X^+)^*$, (2) the formation of the hole transfer intermediate $X^\bullet$, and (3) the recovery of the ground state X^+, it was found that the photophysics depends in a sensitive way on the base sequence in the proximity of the chromophore.

In the presence of only neighboring A:T base pairs, no charge transfer occurs during the excited-state lifetime (18 ns) of the chromophore. The presence of a G:C base pair within two base pairs of X^+ results in fluorescence quenching. If a guanine nucleobase is directly next to X^+, the acridine radical is formed within 4 ps and decays on a 30 ps time scale. Placing one A:T base pair between the chromophore and guanine slows down the forward transfer rate by three orders of magnitude, corresponding to an apparent β value of >2.0 $Å^{-1}$. As verified by temperature-dependent measurements for a series of duplexes that sample an appreciable range of donor–acceptor separations (~4–10 Å), this steep distance dependence of charge injection is caused not solely by a decrease in electronic coupling, but also by a concomitant increase in the activation energy with increasing distance. Increasing the donor–acceptor distance leads to a change in charge transfer mechanism from a nearly activationless to a thermally activated regime in which the forward transfer is slower than the back transfer, and the acridine radical state is no longer observed. An analysis of the rates and activation energies shows that the hole transfer slows down by a

factor of about 100 due to activation and by a factor of 20 due to the decrease in electronic couplings. Independent of the detailed contributions to the distance-dependent activation energy, this phenomenon illustrates the potentially complex nature of experimental β values, which are often discussed exclusively in terms of the electronic couplings. However, these results indicate that X^+-modified DNA duplexes cannot be utilized for long-range hole transport studies. Due to its activation, hole transport in this system cannot compete with the backward charge shift of the initially formed $X^{\bullet}$–$G^{\bullet+}$ radical pair.

In principle, the observed increase in activation energy could have resulted from either (1) the loss of driving force due to excited-state relaxation, as reported for 9-amino-6-chloro-2-methoxyacridine in solution, competing with charge transfer, or from (2) distance-dependent changes in the energetics, predominantly of the medium reorganization energy in this charge shift reaction, on purely electrostatic grounds. By probing the stimulated emission spectrum of the chromophore with femtosecond broadband absorption spectroscopy, the Stokes shift in a duplex with only A:T base pairs was shown to reach a constant value within 220 fs. Thus mechanism (2) can be ruled out.

It was demonstrated that the increase in thermal activation energy with distance can be self-consistently explained within the framework of a distance-dependent reorganization energy. Fits which are based on the experimental data for two different hole acceptors at three different donor–acceptor distances, yield lower limits for the medium reorganization energy of about 0.8 eV at 10 Å donor–acceptor separation. In the absence of detailed structural information about the chromophore binding site, the rather large reorganization energy indicates the presence of highly polarizable molecular dipoles or ions in the immediate environment of either the donor and/or acceptor species.

It was shown that the activated nature of hole transfer in X^+-modified DNA duplexes can be used to investigate the hierarchy of oxidation potentials of modified purine nucleobases in situ. A comparison of the hole injection rates with the oxidation potentials of the nucleobases in solution points to the hierarchy of the oxidation potentials being largely conserved upon incorporation of these bases into a DNA duplex.

Apart from the detailed role of energetics and electronic couplings for electron transfer in DNA, the charge shift processes in these modified duplexes demonstrate in a dramatic way that the distance dependence of the Franck–Condon factor is superimposed on the distance dependence of the electronic coupling. Such distance-dependent energetics are expected to be relevant in all short distance (<10 Å) donor–acceptor systems, in which activated electron transfer and appreciable medium reorganization energies prevail.

Engineered Fluorescein-Binding Protein

Anticalins are a novel class of engineered ligand-binding proteins with tailored specificities derived from the lipocalin scaffold. The anticalin FluA binds the fluorescein dianion with high affinity and quenches its fluorescence. Femtosecond absorption spectroscopy revealed excited-state electron transfer from a tryptophan or tyrosine residue to the bound fluorescein group in its excited singlet state on a 400 fs time scale. This short time is one of the fastest electron transfer reactions resolved in a protein at physiological temperature so far.

The monoexponential ultrafast decay kinetics of the excited fluorescein dianion point to a well-defined binding site. The temperature independence of the rate suggests an (almost) activationless process. On the basis of conventional electron transfer theory, globally applied to both the fast forward and slower back electron transfer rates, the electronic interaction involved in the electron transfer process is estimated to be about 170 cm^{-1} (140 cm^{-1}) in the case of tryptophan (tyrosine) assuming a polar environment, i.e., electrostatic screening of the Coulomb interaction. Electronic interactions of this magnitude indicate a favorable geometry and a short distance between donor and acceptor. This view is confirmed by a recent X-ray structure of the FluA–fluorescein complex showing that the aromatic amino acid side chain of a tryptophan residue and the xanthene ring of the chromophore are coplanar with a center-to-center distance of about 3.5 Å.

The weak steady-state fluorescence is due to a 10% minority of FluA–fluorescein complexes, which is characterized by their red-shifted absorption as reflected in the fluorescence excitation spectrum and by an excited-state lifetime that is longer by a factor of 100 than the lifetime of the majority species.

In principle, steady-state absorption and fluorescence excitation spectra as well as fluorescence quantum yields cannot distinguish between heterogeneous binding sites on the one hand and distinct binding sites with reduced quenching efficiency on the other. In view of the strong interest in the structural characterization of hapten/antibody systems, in particular with respect to site-directed amino acid exchange, the experiments described in this work underline the value of time-resolved spectroscopy as a unique diagnostic tool.

References

[1] A. M. Kuznetsov, J. Ulstrup, *Electron Transfer in Chemistry and Biology*, Wiley, New York, **1999**.

[2] P. F. Heelis, R. F. Hartman, S. D. Rose, *Chem. Soc. Rev.* **1995**, 289-297.

[3] M. E. Michel-Beyerle, Ed., *The Reaction Center of Photosynthetic Bacteria*, Springer Verlag, Berlin, **1996**.

[4] W. Zinth, W. Kaiser, in *The Photosynthetic Reaction Center, Vol. 2* (Eds.: J. Deisenhofer, J. R. Norris), Academic Press, New York, **1993**, pp. 71-88.

[5] J. Deisenhofer, J. R. Norris, Eds., *The Photosynthetic Reaction Center*, Academic Press, New York, **1993**.

[6] C. J. Murphy, M. R. Arkin, Y. Jenkins, N. D. Ghatlia, S. H. Bossmann, N. J. Turro, J. K. Barton, *Science* **1993**, *262*, 1025-1029.

[7] P. J. Dandliker, R. E. Holmlin, J. K. Barton, *Science* **1997**, *275*, 1465-1468.

[8] A. M. Brun, A. Harriman, *J. Am. Chem. Soc.* **1992**, *114*, 3656-3660.

[9] F. D. Lewis, T. Wu, Y. Zhang, R. L. Letsinger, S. R. Greenfield, M. R. Wasielewski, *Science* **1997**, *277*, 673-676.

[10] P. F. Barbara, E. J. C. Olson, in *Electron Transfer: From Isolated Molecules to Biomolecules, Part Two* (Eds.: J. Jortner, M. Bixon), Wiley, New York, **1999**, pp. 647-676.

[11] J. Jortner, M. Bixon, T. Langenbacher, M. E. Michel-Beyerle, *Proc. Natl. Acad. Sci. U.S.A.* **1998**, *95*, 12759-12765.

[12] C. A. M. Seidel, A. Schulz, M. H. M. Sauer, *J. Phys. Chem.* **1996**, *100*, 5541-5553.

[13] S. Steenken, S. V. Jovanovic, *J. Am. Chem. Soc.* **1997**, *119*, 617-618.

[14] A. Heller, *Faraday Discuss.* **2000**, *116*, 1-13.

[15] S. D. Bruner, D. P. G. Norman, G. L. Verdine, *Nature* **2000**, *403*, 859-866.

[16] E. Braun, Y. Eichen, U. Sivan, G. Ben-Joseph, *Nature* **1998**, *391*, 775-778.

[17] H.-W. Fink, C. Schönenberger, *Nature* **1999**, *398*, 407-410.

[18] C. Dekker, M. A. Ratner, *Phys. World* **2001**, *14*, 29-33.

[19] V. A. Bloomfield, D. M. Crothers, I. Tinoco, Jr., *Nucleic Acids: Structures, Properties, and Functions*, University Science Books, Sausalito, **2000**.

[20] J. N. S. Evans, *Biomolecular NMR Spectroscopy*, Oxford University Press, Oxford, **1995**.

[21] K. Fukui, K. Tanaka, *Angew. Chem. Int. Ed.* **1998**, *37*, 158-161.

[22] K. Fukui, K. Tanaka, M. Fujitsuka, A. Watanabe, O. Ito, *J. Photochem. Photobiol. B: Biol.* **1999**, *50*, 18-27.

[23] K. Fukui, K. Tanaka, *Nucleic Acids Res.* **1996**, *24*, 3962-3967.

[24] R. A. Marcus, *J. Chem. Phys.* **1956**, *24*, 966-978.

[25] G. Beste, F. S. Schmidt, T. Stibora, A. Skerra, *Proc. Natl. Acad. Sci. U.S.A.* **1999**, *96*, 1898-1903.

[26] P. G. Seybold, M. Gouterman, J. Callei, *Photochem. Photobiol.* **1969**, *9*, 229-242.

[27] G. A. Weiss, H. B. Lowman, *Chem. Biol.* **2000**, *7*, 177-184.

[28] S. Bar-Noy, A. Darmon, H. Ginsberg, Z. I. Cabantchik, *Biochim. Biophys. Acta* **1984**, *778*, 612-614.

[29] L. A. Sklar, D. A. Finney, Z. G. Oades, A. J. Jesaitis, R. G. Painter, C. G. Cochrane, *J. Biol. Chem.* **1984**, *259*, 5661-5669.

[30] A. Skerra, *Biochim. Biophys. Acta* **2000**, *1482*, 337-350.

[31] A. Skerra, *Rev. Mol. Biotechnol.* **2001**, *74*, 257-275.

[32] V. May, O. Kühn, *Charge and Energy Transfer Dynamics in Molecular Systems*, Wiley-VCH, Berlin, **2000**.

[33] M. A. El-Sayed, I. Tanaka, Y. Molin, Eds., *Ultrafast Processes in Chemistry and Photobiology*, Blackwell, Berlin, **1995**.

[34] G. R. Fleming, *Chemical Applications of Ultrafast Spectroscopy*, Oxford University Press, Clarendon Press, New York, Oxford, **1986**.

[35] C. Musewald, *PhD Thesis*, Technische Universität München **1999**.

[36] M. Götz, *PhD Thesis*, Technische Universität München **2002**.

[37] C. Rullière, Ed., *Femtosecond Laser Pulses*, Springer, Berlin, Heidelberg, New York, **1998**.

[38] M. Volk, *PhD Thesis*, TU München **1991**.

[39] N. P. Ernsting, S. A. Kovalenko, T. Senyushkina, J. Saam, V. Farztdinov, *J. Phys. Chem. A* **2001**, *105*, 3443-3453.

[40] S. A. Kovalenko, A. L. Dobryakov, J. Ruthmann, N. P. Ernsting, *Phys. Rev. A* **1999**, *59*, 2369-2384.

[41] J. Jortner, M. Bixon, Eds., *Electron Transfer: From Isolated Molecules to Biomolecules*, Wiley, New York, **1999**.

[42] P. F. Barbara, T. J. Meyer, M. A. Ratner, *J. Phys. Chem.* **1996**, *100*, 13148-13168.

[43] R. A. Marcus, N. Sutin, *Biochim. Biophys. Acta* **1985**, *811*, 265-322.

[44] A. Weller, *Z. Physik. Chem. NF* **1982**, *133*, 93-98.

[45] K. Kumar, I. V. Kurnikov, D. N. Beratan, D. H. Waldeck, M. B. Zimmt, *J. Phys. Chem. A* **1998**, *102*, 5529-5541.

[46] H. L. Tavernier, M. D. Fayer, *J. Phys. Chem. B* **2000**, *104*, 11541-11550.

[47] V. O. Levich, *Adv. Electrochem.* **1966**, *4*, 249-371.

[48] J. Jortner, *J. Chem. Phys.* **1976**, *64*, 4860-4867.

[49] J. Ulstrup, J. Jortner, *J. Chem. Phys.* **1975**, *63*, 4358-4368.

[50] R. A. Marcus, *J. Chem. Phys.* **1984**, *81*, 4494-4500.

[51] R. P. Van Duyne, S. F. Fischer, *Chem. Phys.* **1974**, *5*, 183-197.

[52] M. Bixon, J. Jortner, in *Electron Transfer: From Isolated Molecules to Biomolecules, Part One* (Eds.: J. Jortner, M. Bixon), Wiley, New York, **1999**, pp. 35-202.

[53] C. C. Page, C. C. Moser, X. Chen, P. L. Dutton, *Nature* **1999**, *402*, 47-51.

[54] R. Langen, J. L. Colón, D. R. Casimiro, T. B. Karpishin, J. R. Winkler, H. B. Gray, *J. Biol. Inorg. Chem.* **1996**, *1*, 221-225.

[55] B. Giese, *Acc. Chem. Res.* **2000**, *33*, 631-636.

[56] G. B. Schuster, *Acc. Chem. Res.* **2000**, *33*, 253-260.

[57] M. Bixon, J. Jortner, *J. Phys. Chem. B* **2000**, *104*, 3906-3913.

[58] M. Bixon, B. Giese, S. Wessely, T. Langenbacher, M. E. Michel-Beyerle, J. Jortner, *Proc. Natl. Acad. Sci. U.S.A.* **1999**, *96*, 11713-11716.

[59] Y. A. Berlin, A. L. Burin, M. A. Ratner, *J. Phys. Chem. A* **2000**, *104*, 443-445.

[60] F. D. Lewis, R. L. Letsinger, M. R. Wasielewski, *Acc. Chem. Res.* **2001**, *34*, 159-170.

[61] E. Meggers, M. E. Michel-Beyerle, B. Giese, *J. Am. Chem. Soc.* **1998**, *120*, 12950-12955.

[62] V. Shafirovich, A. Dourandin, W. Huang, N. P. Luneva, N. E. Geacintov, *Phys. Chem. Chem. Phys.* **2000**, *2*, 4399-4408.

[63] C. Wan, T. Fiebig, O. Schiemann, J. K. Barton, A. H. Zewail, *Proc. Natl. Acad. Sci. U.S.A.* **2000**, *97*, 14052-14055.

[64] K. Fukui, K. Iwane, T. Shimidzu, Y. Takano, *Tetrahedron Lett.* **1996**, *37*, 4983-4986.

[65] K. Fukui, M. Morimoto, H. Segawa, K. Tanaka, T. Shimidzu, *Bioconjugate Chem.* **1996**, *7*, 349-355.

[66] F. D. Lewis, T. Wu, X. Liu, R. L. Letsinger, S. R. Greenfield, S. E. Miller, M. R. Wasielewski, *J. Am. Chem. Soc.* **2000**, *122*, 2889-2902.

[67] W. B. Davis, W. A. Svec, M. A. Ratner, M. R. Wasielewski, *Nature* **1998**, *396*, 60-63.

[68] P. Finckh, H. Heitele, M. Volk, M. E. Michel-Beyerle, *J. Phys. Chem.* **1988**, *92*, 6584-6590.

[69] G. L. Closs, J. R. Miller, *Science* **1988**, *240*, 440-446.

[70] H. Oevering, M. N. Paddon-Row, M. Heppener, A. M. Oliver, E. Cotsaris, J. W. Verhoeven, N. S. Hush, *J. Am. Chem. Soc.* **1987**, *109*, 3258-3269.

[71] A. A. Voityuk, J. Jortner, M. Bixon, N. Rösch, *J. Chem. Phys.* **2001**, *114*, 5614-5620.

[72] A. A. Voityuk, N. Rösch, *J. Phys. Chem. B* **2002**, *106*, 3013-3018.

[73] A. A. Voityuk, N. Rösch, M. Bixon, J. Jortner, *J. Phys. Chem. B* **2000**, *104*, 9740-9745.

[74] J. Olofsson, S. Larsson, *J. Phys. Chem. B* **2001**, *105*, 10398-10406.

[75] F. C. Grozema, Y. A. Berlin, L. D. A. Siebbeles, *J. Am. Chem. Soc.* **2000**, *122*, 10903-10909.

[76] Y.-P. Liu, M. D. Newton, *J. Phys. Chem.* **1994**, *98*, 7162-7169.

[77] A. Marty, M. Bourdeaux, M. Dell'Amico, P. Viallet, *Eur. Biophys. J.* **1986**, *13*, 251-257.

[78] J. Sun, M. Rougée, M. Delarue, T. Montenay-Garestier, C. Hélène, *J. Phys. Chem.* **1990**, *94*, 968-977.

[79] P. Fan, T. Härd, D. R. Kearns, *J. Phys. Chem.* **1989**, *93*, 6615-6622.

[80] S. O. Kelley, J. K. Barton, *Chem. Biol.* **1998**, *5*, 413-425.

[81] M.-H. Baik, J. S. Silverman, I. V. Yang, P. A. Ropp, V. A. Szalai, W. Yang, H. H. Thorp, *J. Phys. Chem. B* **2001**, *105*, 6437-6444.

[82] M. Nastasi, J. M. Morris, D. M. Rayner, V. L. Seligy, A. G. Szabo, D. F. Williams, R. E. Williams, R. W. Yip, *J. Am. Chem. Soc.* **1976**, *98*, 3979-3986.

[83] U. Asseline, F. Toulmé, N. T. Thuong, M. Delarue, T. Montenay-Garestier, C. Hélène, *EMBO J.* **1984**, *3*, 795-800.

[84] W. C. Johnson, in *Circular Dichroism: Principles and Applications* (Eds.: K. Nakanishi, N. Berova, R. W. Woody), VCH, New York, **1994**, pp. 523-541.

[85] M. Durand, J. C. Maurizot, U. Asseline, N. T. Thuong, C. Hélène, *Bioconjugate Chem.* **1993**, *4*, 206-211.

[86] A. T. Poulos, G. S. Hammond, M. E. Burton, *Photochem. Photobiol.* **1981**, *34*, 169-175.

[87] P. Neta, *J. Phys. Chem.* **1979**, *83*, 3096-3101.

[88] L. P. Candeias, S. Steenken, *J. Am. Chem. Soc.* **1989**, *111*, 1094-1099.

[89] W. D. Wilson, I. G. Lopp, *Biopolymers* **1979**, *18*, 3025-3041.

[90] H. Neubauer, C. Griesinger, personal communication.

[91] F. D. Lewis, R. S. Kalgutkar, Y. Wu, X. Liu, J. Liu, R. T. Hayes, S. E. Miller, M. R. Wasielewski, *J. Am. Chem. Soc.* **2000**, *122*, 12346-12351.

[92] M. Bixon, J. Jortner, *J. Am. Chem. Soc.* **2001**, *123*, 12556-12567.

[93] F. D. Lewis, J. Liu, X. Liu, X. Zuo, R. T. Hayes, M. R. Wasielewski, *Angew. Chem. Int. Ed.* **2002**, *41*, 1026-1028.

[94] M. O. Vlad, J. Ross, *J. Phys. Chem. B* **1997**, *101*, 8756-8773.

[95] E. B. Brauns, M. L. Madaras, R. S. Coleman, C. J. Murphy, M. A. Berg, *J. Am. Chem. Soc.* **1999**, *121*, 11644-11649.

[96] A. N. Lane, T. C. Jenkins, *Q. Rev. Biophys.* **2000**, *33*, 255-306.

[97] M. Nastasi, R. W. Yip, V. L. Seligy, A. G. Szabo, R. E. Williams, *Nature* **1974**, *249*, 248-250.

[98] G. Cosa, K.-S. Focsaneanu, J. R. N. McLean, J. P. McNamee, J. C. Scaiano, *Photochem. Photobiol.* **2001**, *73*, 585-599.

[99] U. Pachmann, R. Riegler, *Exptl. Cell. Res.* **1972**, *72*, 602-604.

[100] L. Yang, S. Weerasinghe, P. E. Smith, B. M. Pettitt, *Biophys. J.* **1995**, *69*, 1519-1527.

[101] D. Zinger, N. E. Geacintov, *Photochem. Photobiol.* **1988**, *47*, 181-188.

[102] C. Hélène, T. Montenay-Garestier, T. Saison, M. Takasugi, J. J. Toulmé, U. Asseline, G. Lancelot, G. C. Maurizot, F. Toulmé, N. T. Thuong, *Biochimie* **1985**, *67*, 777-783.

[103] P. L. Pearson, M. Bobrow, C. G. Vosa, *Nature* **1970**, *226*, 78-79.

[104] B. Giese, J. Amaudrut, A.-K. Köhler, M. Spormann, S. Wessely, *Nature* **2001**, *412*, 318-320.

[105] A. C. Capomacchia, S. G. Schulman, *Anal. Chim. Acta* **1975**, *77*, 79-85.

[106] Y. Ni, D. R. Kearns, *J. Phys. Chem.* **1989**, *93*, 6622-6625.

[107] J. Tomasi, M. Persico, *Chem. Rev.* **1994**, *94*, 2027-2094.

[108] M. L. Horng, J. A. Gardecki, A. Papazyan, M. Maroncelli, *J. Phys. Chem.* **1995**, *99*, 17311-17337.

[109] L. Reynolds, J. A. Gardecki, S. J. V. Frankland, M. L. Horng, M. Maroncelli, *J. Phys. Chem.* **1996**, *100*, 10337-10354.

[110] C. G. Hoogstraten, C. V. Grant, T. E. Horton, V. J. DeRose, R. D. Britt, *J. Am. Chem. Soc.* **2002**, *124*, 834-842.

[111] W. B. Davis, M. A. Ratner, M. R. Wasielewski, *J. Am. Chem. Soc.* **2001**, *123*, 7877-7886.

[112] P. Vath, M. B. Zimmt, *J. Phys. Chem. A* **2000**, *104*, 2626-2633.

[113] N. Sutin, in *Electron Transfer in Inorganic, Organic, and Biological Systems* (Eds.: J. R. Bolton, N. Mataga, G. McLendon), The American Chemical Society, Washington, **1991**, pp. 25-43.

[114] J. M. Hale, in *Reactions of Molecules at Electrodes* (Ed.: N. S. Hush), Wiley-Interscience, New York, **1971**, pp. 229-257.

[115] J. Jortner, M. Bixon, *J. Chem. Phys.* **1988**, *88*, 167-170.

[116] B. S. Brunschwig, S. Ehrenson, N. Sutin, *J. Phys. Chem.* **1986**, *90*, 3657-3668.

[117] B. S. Brunschwig, S. Ehrenson, N. Sutin, *J. Am. Chem. Soc.* **1984**, *106*, 6858-6859.

[118] E. H. Yonemoto, G. B. Saupe, R. H. Schmehl, S. M. Hubig, R. L. Riley, B. L. Iverson, T. E. Mallouk, *J. Am. Chem. Soc.* **1994**, *116*, 4786-4795.

[119] F. D. Lewis, Y. Wu, *J. Photochem. Photobiol. C* **2001**, *2*, 1-16.

[120] B. Giese, A. Biland, *submitted*.

[121] S. S. Isied, A. Vassilian, J. F. Wishart, C. Creutz, H. A. Schwarz, N. Sutin, *J. Am. Chem. Soc.* **1988**, *110*, 635-637.

[122] M. J. Powers, D. J. Salmon, R. W. Callahan, T. J. Meyer, *J. Am. Chem. Soc.* **1976**, *98*, 6731-6733.

[123] W. Saenger, *Principles of Nucleic Acid Structure*, Springer Verlag, New York, **1984**.

[124] A. Holmen, B. Norden, B. Albinsson, *J. Am. Chem. Soc.* **1997**, *119*, 3114-3121.

[125] F. Seela, T. Grein, *Nucleic Acids Res.* **1992**, *20*, 2297-2306.

[126] F. Seela, N. Ramzaeva, M. Zulauf, *Nucleos. Nucleot.* **1997**, *16*, 963-966.

[127] L. G. Karber, G. Dryhurst, *Anal. Chim. Acta* **1979**, *108*, 193-204.

[128] K. Nakatani, C. Dohno, I. Saito, *J. Am. Chem. Soc*. **2000**, *122*, 5893-5894.

[129] H. Sugiyama, I. Saito, *J. Am. Chem. Soc.* **1996**, *118*, 7063-7068.

[130] A. A. Voityuk, J. Jortner, M. Bixon, N. Rösch, *Chem. Phys. Lett.* **2000**, *324*, 430-434.

[131] W. B. Davis, I. Naydenova, R. Haselsberger, A. Ogrodnik, B. Giese, M. E. Michel-Beyerle, *Angew. Chem.* **2000**, *112*, 3795-3798.

[132] F. D. Lewis, X. Liu, J. Liu, R. T. Hayes, M. R. Wasielewski, *J. Am. Chem. Soc.* **2000**, *122*, 12037-12038.

[133] M. Bixon, J. Jortner, *J. Phys. Chem. A* **2001**, *105*, 10322-10328.

[134] I. Saito, T. Nakamura, K. Nakatani, Y. Yoshioka, K. Yamaguchi, H. Sugiyama, *J. Am. Chem. Soc.* **1998**, *120*, 12686-12687.

[135] Y. Yoshioka, Y. Kitagawa, Y. Takano, K. Yamaguchi, T. Nakamura, I. Saito, *J. Am. Chem. Soc.* **1999**, *121*, 8712-8719.

[136] N. Klonis, W. H. Sawyer, *J. Fluoresc.* **1996**, *6*, 147-157.

[137] R. Sjöback, J. Nygren, M. Kubista, *Spectrochim. Acta A* **1995**, *51*, 7-21.

[138] G. R. Fleming, A. W. E. Knight, J. M. Morris, R. J. S. Morrison, G. W. Robinson, *J. Am. Chem. Soc.* **1977**, *99*, 4306-4311.

[139] D. J. Lougnot, C. R. Goldschmidt, *J. Photochem.* **1980**, *12*, 215-224.

[140] U. Krüger, R. Memming, *Ber. Bunsenges. Phys. Chem.* **1974**, *78*, 670-678.

[141] L. K. Denzin, G. A. Gulliver, E. W. J. Voss, *Mol. Immunol.* **1993**, *30*, 1331-1345.

[142] A. Harriman, *J. Phys. Chem.* **1987**, *91*, 6102-6104.

[143] B. A. Coles, R. G. Compton, *J. Electroanal. Chem.* **1983**, *144*, 87-98.

[144] J. Pan, W. Lin, W. Wang, Z. Zhan, C. Lu, S. Yao, N. Lin, D. Zhu, *Biophys. Chem.* **2001**, *89*, 193-199.

[145] W. A. Prütz, E. J. Land, *Int. J. Radiat. Biol.* **1979**, *36*, 513-520.

[146] T. Häberle, J. Hirsch, F. Pöllinger, H. Heitele, M. E. Michel-Beyerle, C. Anders, A. Döhling, C. Krieger, A. Rückemann, H. A. Staab, *J. Phys. Chem.* **1996**, *100*, 18269-18274.

[147] A. Skerra, personal communication.

[148] E. W. J. Voss, *Comments Mol. Cell. Biophys.* **1990**, *6*, 197-221.

[149] N. Klonis, A. H. A. Clayton, E. W. J. Voss, W. H. Sawyer, *Photochem. Photobiol.* **1998**, *67*, 500-510.

[150] E. W. J. Voss, R. M. Watt, *Immunochemistry* **1977**, *14*, 237-246.

[151] E. W. J. Voss, *Fluorescein Hapten: An immunological probe*, CRC Press, Boca Raton, **1984**.

[152] E. W. J. Voss, J. C. Croney, D. M. Jamesson, *Mol. Immunol.* **2001**, *38*, 35-44.

[153] R. M. Watt, E. W. J. Voss, *Immunochemistry* **1977**, *14*, 533-541.

[154] S. Komazaki, I. Ikegami, H. Forosawa, F. Yasuda, K. Yoshihara, *J. Phys. Chem. B* **2001**, *105*, 1093-1099.

Parts of This Work Have Already Been Published

[1] S. Hess, M. Götz, W. B. Davis, M. E. Michel-Beyerle. On the Apparently Anomalous Distance Dependence of Charge Transfer Rates in 9-Amino-6-chloro-2-methoxy-acridine-modified DNA. *J. Am. Chem. Soc.* **2001**, *123*, 10046-10055.

[2] M. Götz, S. Hess, G. Beste, A. Skerra, M. E. Michel-Beyerle. Ultrafast Electron Transfer in the Complex between Fluorescein and a Cognate Engineered Lipocalin Protein, a So-Called Anticalin. *Biochemistry* **2002**, *41*, 4156-4164.

[3] W. B. Davis, S. Hess, I. Naydenova, R. Haselsberger, A. Ogrodnik, M. D. Newton, M. E. Michel-Beyerle. Distance-Dependent Activation Energies for Hole Injection from Protonated 9-Amino-6-chloro-2-methoxyacridine into Duplex DNA. *J. Am. Chem. Soc*. **2002**, *124*, 2422-2423.

[4] S. Hess, W. B. Davis, A. A. Voityuk, N. Rösch, M. E. Michel-Beyerle, N. P. Ernsting, S. A. Kovalenko, J. L. Pérez Lustres. Excited-State Photophysics of 9-Amino-6-chloro-2-methoxyacridine Selectively Intercalated in Duplex DNA. *ChemPhysChem* **2002**, in press.

Other Publications

[5] S. Hess, P. Vöhringer. Instantaneous Product Anisotropies in the fs-Photolysis of Triodide. In *Ultrafast Phenomena XI* (Eds.: T. Elsaesser, J. G. Fujimoto, D. A. Wiersma, W. Zinth), Springer Verlag, Berlin, **1998**, pp. 600-602.

[6] S. Hess, H. Bürsing, P. Vöhringer. Dynamics of Fragment Recoil in the Femtosecond Photodissociation of Triiodide Ions in Liquid Solution. *J. Chem. Phys.* **1999**, *111*, 5461-5473.

[7] S. Hess, H. Hippler, T. Kühne, P. Vöhringer. Reply to the Comment on “Transient Anisotropy and Fragment Rotational Excitation in the Femtosecond Photodissociation of Triiodide in Solution”. *J. Phys. Chem.* **1999**, *103*, 5623-5624.

[8] H. Bürsing, J. Lindner, S. Hess, P. Vöhringer. Real-Time Probing of Vectorial Properties of Ultra-Fast Photodissociations in Liquids. *Appl. Phys. B* **2000**, *71*, 411-417.

[9] H. Bürsing, S. Hess, P. Vöhringer. Coherent Femtosecond Anisotropies and Rotational Dynamics in Condensed Phase Chemical Processes. *Nonlinear Optics* **2000**, *24*, 187-190.

Danksagung

Herzlich danken möchte ich allen, die zur Entstehung dieser Arbeit beigetragen haben.

Mein besonderer Dank gilt

Frau Prof. M. E. Michel-Beyerle für die Möglichkeit, das faszinierende Gebiet des Ladungstransfers in DNA kennenzulernen, für ihr großes Interesse am Fortgang dieser Arbeit, ihre stetige Diskussionsbereitschaft sowie ihre äußerst großzügige Unterstützung.

Prof. M. D. Newton, Prof. N. Rösch und Dr. A. A. Voityuk sowie Prof. N. P. Ernsting, Dr. S. A. Kovalenko und Dr. J. L. Pérez Lustres für die erfolgreiche Kooperation und Prof. A. Skerra für die sehr interessanten FluA Proben.

Prof. Bill Davis für seinen unermüdlichen Einsatz, seine Begeisterung für das Projekt und für zahlreiche Diskussionen über Wissenschaftliches und Nichtwissenschaftliches sowie für das kritische und konstruktive Korrekturlesen dieser Arbeit.

Mirco Götz für die freundschaftliche und produktive Zusammenarbeit, die obligatorischen Pausen mit Automatenkaffee und seine imposanten Gesangseinlagen („In the Ghetto”) nachts im dunklen Labor.

Christian Kompa für die gute Zusammenarbeit sowie die tatkräftige Unterstützung bei der Bewältigung von technischen Problemen aller Art.

Dr. Izabella Naydenova und Reinhard Haselsberger für die Nanosekunden-Absorptionsmessungen, die für zentrale Erkenntnisse dieser Arbeit unerläßlich waren.

den weiteren Mitgliedern des Arbeitskreises, Tanja Schüttrigkeit, Till von Feilitzsch, Pancho Tzankov, Dr. Andreas Kummer, Dr. Alex Ogrodnik und Dr. Reiner Feick, für die gute Zusammenarbeit und stetige Hilfsbereitschaft.

Frau Reischl und Gabi Dietrich für ihre unkomplizierte und immer freundliche Handhabung aller administrativen und sonstigen Probleme.

dem Fonds der chemischen Industrie für die finanzielle Unterstützung.

vor allem meinen Eltern und meinem Bruder Christian, der mir durch sein „Voranschreiten” so manchen Weg aufgezeigt hat, für ihre einzigartige Unterstützung.

nicht zuletzt meiner Katrin für ihre außerordentliche Unterstützung, ihre unendliche Geduld, ihr Verständnis und ihren (fast) unerschütterlichen Glauben an einfachere Zeiten.